ESTI FILE COPY

ESD-TDR-64-16

ESTI PROCESSED

☐ DDC TAB ☐ PROJ OFFICER
☐ ACCESSION MASTER FILE
☐ ________

DATE ________

ESTI CONTROL NR AL-40116

CY NR 1 OF 1 CYS

ESD RECORD COPY
RETURN TO
SCIENTIFIC & TECHNICAL INFORMATION DIVISION
(ESTI), BUILDING 1211

COPY NR. ______ OF ______ COPIES

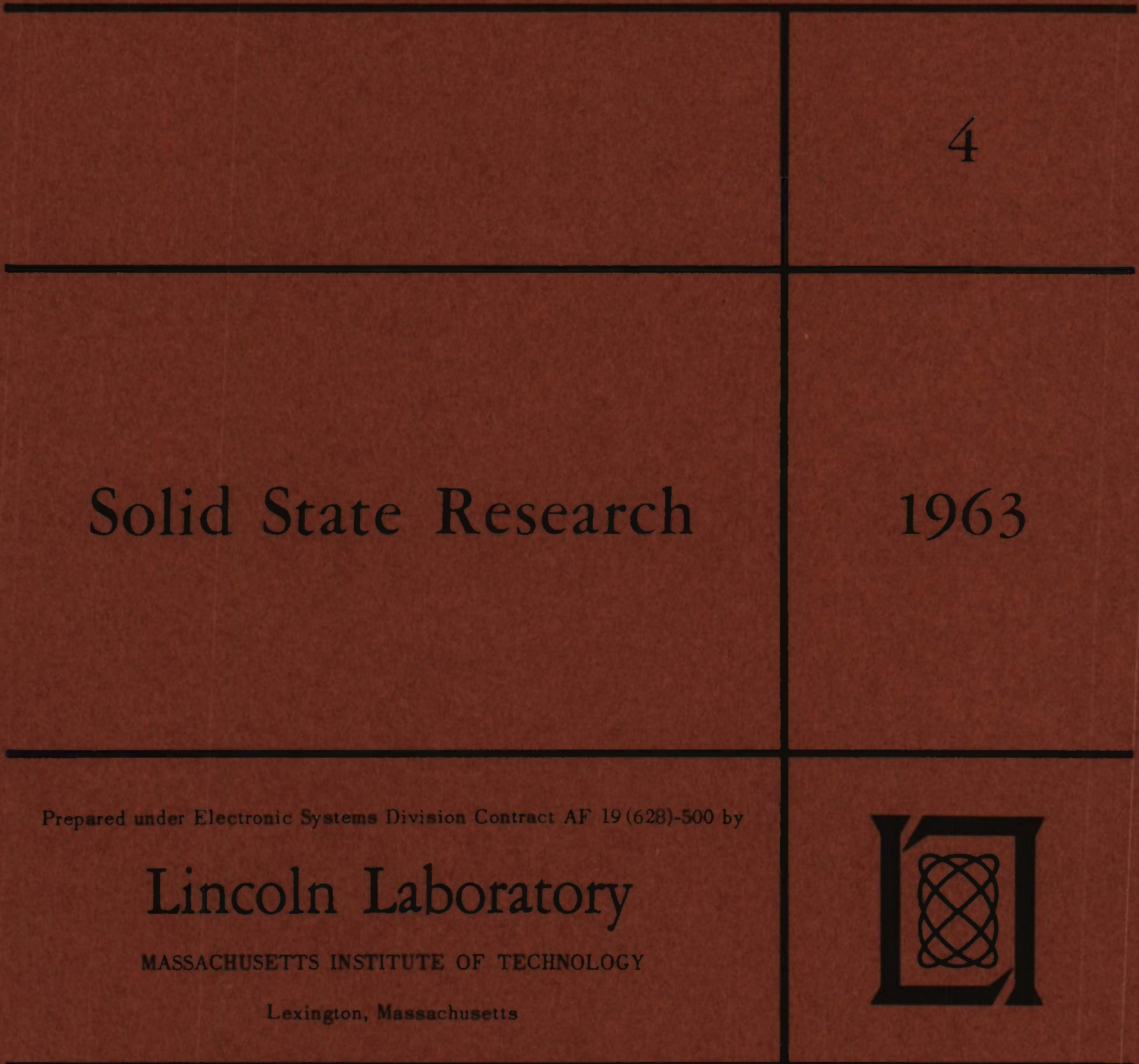

4

Solid State Research

1963

Prepared under Electronic Systems Division Contract AF 19(628)-500 by

Lincoln Laboratory

MASSACHUSETTS INSTITUTE OF TECHNOLOGY

Lexington, Massachusetts

ESD RECORD COPY
RETURN TO
SCIENTIFIC & TECHNICAL INFORMATION DIVISION
(ESTI), BUILDING 1211

COPY NR. ______ OF ______ COPIES

AD0435023

The work reported in this document was performed at Lincoln Laboratory, a center for research operated by Massachusetts Institute of Technology, with the support of the U.S. Air Force under Contract AF 19(628)-500.

Non-Lincoln Recipients

PLEASE DO NOT RETURN

Permission is given to destroy this document when it is no longer needed.

4

Solid State Research

1963

Issued 9 March 1964

Lincoln Laboratory

MASSACHUSETTS INSTITUTE OF TECHNOLOGY

Lexington, Massachusetts

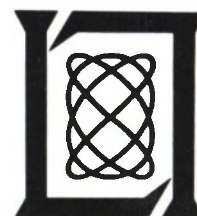

INTRODUCTION

I. SOLID STATE DEVICE RESEARCH

Forward-biased InSb diodes have been operated as CW lasers and the emission wavelength has been changed in steps of 50 Å from one cavity mode to an adjacent one by applying incremental steps of magnetic field of less than 600 gauss. The magnetic field also affects the refractive index n, as evidenced by the shift to shorter wavelength by 15 Å/kgauss of a given cavity mode. The measured 8-Å half-width of the emission line corresponds to the resolution of the grating spectrometer used. Continuous operation has been made possible at 2°K and in longitudinal magnetic fields above about 20 kgauss, by going to purer base material for the diodes. Threshold current densities for laser action at 2°K and 27 kgauss of 1400 amp cm^{-2} have been achieved.

A $CaF_2:U^{3+}$ laser has been pumped with the light input from GaAs injection lasers. Five GaAs injection lasers, electrically connected in series, were mounted along the slit of an integrating chamber in which was placed the 4-cm-long-by-3-mm-diameter laser rod of $CaF:0.1\% U^{3+}$. Laser action at 2.631 microns was observed when the current through the diodes was increased above 3.7 amp, which corresponded to 2.9 watts of 0.84-micron radiation delivered to the integrating chamber. In injection luminescent pumping, the conversion efficiency of input electrical power into useful pump radiation may be as high as 50 percent. By using mixed semiconductor crystals, one can, in principle, tailor the luminescence wavelength to match a particular laser material ideally, and thus make the conversion of the pump radiation to laser radiation also very high. In addition to the higher efficiency _per se_, injection luminescent pumping would reduce the heat dissipation in the pumped laser by a factor of at least ten over that of flash-tube pumping. This reduction in heat dissipation should significantly reduce the thermal gradient problems that plague high-energy lasers. A high-efficiency system under study is $(Ga_xIn_{1-x})As$ diodes, radiating at 0.875 micron, pumping a Nd^{3+} laser which emits at 1.06 microns. Relatively large single crystals of $(Ga_xIn_{1-x})As$ have been grown by the halogen vapor-transport mechanism in a closed system, and work is now in progress to approach the composition required to produce diodes which radiate at 0.875 micron.

The spectrum of the injection luminescence from InAs diodes at 300°K has been measured. The emission line occurs at 0.335 ev and has a half-width of 25 mev compared with the half-width of 12 mev at 2°K. The spectrum of the radiation from InAs diodes at 2°K has also been measured with a system that is more sensitive than that previously used. An additional peak is seen at 0.372 ev, 30 mev below the main emission peak, and a knee is observed at 0.34 ev.

A miniature "pill" laser package has been developed which consists of a GaAs laser and two semi-insulating GaAs spacers alloyed between two 0.080-inch-diameter metallic disks.

Lasers in this package have been supplied to other groups in the Laboratory for use in optical radar development.

The flatness of diffused junctions in GaSb is being studied to determine whether irregularities in the junction plane can explain why lasers have not been fabricated from GaSb. It has been found for diffusions at 650°C from a dilute source of zinc in gallium that the junction plane more closely follows irregularities in the surface when the diffusant concentration is reduced.

Diffused p-n junction diodes have been fabricated of PbSe and PbTe. The procedure uses an interdiffusion mechanism for introducing controlled deviation from stoichiometry; excess lead gives rise to n-type and excess selenium and tellurium to p-type PbSe and PbTe, respectively. An analysis of the p-n junction depth results in the following effective interdiffusion constants: $D_{\Delta} = 4 \times 10^{-8}\ cm^2\ sec^{-1}$ for producing a p-layer on n-type PbSe at 600°C; $D_{\Delta} = 9 \times 10^{-9}\ cm^2\ sec^{-1}$ for an n-layer on p-type PbSe at 650°C; $6 \times 10^{-7}\ cm^2\ sec^{-1}$ for an n-layer on p-type PbTe at 650°C.

An experimental and theoretical investigation has been made of growing screw-shaped plasma density waves in a semiconductor bar subjected to parallel electric and magnetic fields. It is shown that in extrinsic material the growth is spatial, corresponding to stable traveling-wave amplification, whereas for nearly equal densities of positive and negative carriers, the wave is absolutely unstable and corresponds to the oscillistor phenomenon. Experimental observations were made in germanium and the growth rates and phase characteristics of the waves were found to be in excellent agreement with theory. For nearly intrinsic material, evidence of instability was found in accordance with the theoretical prediction.

A program has been started to investigate the current instability occurring in n-type GaAs at electric fields about 2000 volts cm^{-1}. The initial experiments of J. B. Gunn on the effects of light, temperature, and magnetic field on the instability have been extended to show that: light sufficient to change the sample conductivity does not affect the instability, immersing the sample in liquid nitrogen does not affect the instability, and a 10,000-gauss magnetic field lowers the amplitude of the instability but does not change its threshold spectrum.

II. LASER RESEARCH

The angular distribution data of stimulated Raman emission from nitrobenzene have been used to calculate the dispersion characteristics of nitrobenzene. Off-axis stimulated emission experiments are in progress to further substantiate the two-step Raman scattering model.

A theoretical study has been made of the growth of Raman radiation from noise. It is found that spherical-growing Stokes waves due to noise sources interact with the incident radiation to produce anti-Stokes radiation strongly peaked at the phase-matching angle. The width of the anti-Stokes peak has been calculated.

New data on the optical absorption and electron spin resonance have been obtained for d^1 electrons in CaF_2. The results are explained by a strong dynamical Jahn-Teller distortion of the electron ground state.

Intense sources of visible pumping radiation are being developed for optically exciting GaAs. Repetitive pulsing at 13 pps and 5000 watts cm^{-2} should yield the required levels for study of possible laser action.

Short fluorescent lifetimes, such as those in GaAs, have been measured by an interferometric phase-shift technique. Samples are excited with multimode helium-neon laser radiation and the phase shift of the beat signal at 155 Mcps is used to determine the fluorescent decay time. Times in the 10^{-9}- to 10^{-10}-second region are easily measured, and typical values are reported for GaAs.

Multilayer dielectric reflectors have been produced separately and as coatings on GaAs lasers. As many as 17 layers have been deposited and 99.9-percent reflection has been obtained over bandwidths as high as 1000 Å.

Improved ruby has yielded far-field diffraction patterns that approach perfect diffraction-limited behavior.

III. MATERIALS RESEARCH

When a carrier gas is used in the vapor growth of crystals, usually the growth rate is inconveniently slow, since the carrier transports material from the source to the growing crystal by natural convection. The use of forced convection to increase the growth rate is being investigated by using this method to grow iodine crystals. Helium gas saturated with iodine vapor passes through a nozzle and strikes an air-cooled glass finger on which crystals are deposited. The rate and efficiency of crystal growth are being measured as a function of the temperature and helium flow rate.

A system has been constructed for making thermoelectric measurements at temperatures between −50° and 900°C on solids with resistances at least as high as 20 meg. Rigorous shielding of all parts of the system is necessary to prevent spurious readings due to pick-up. The system has been used for measurements between 6° and 41°C on a crystal of Cr_2O_3-3% Al_2O_3 whose resistance increases from about 3 to 20 meg in this range. The Seebeck coefficient is +900 μv deg^{-1}.

Thermoelectric measurements have been made on hot-pressed polycrystalline CrO_2 at temperatures between −50° and 240°C. The values of Seebeck coefficient (−6 to −24 μv deg^{-1}) and resistivity (1.2 to 4.3 milliohm-cm) are unusually low for an oxide. No clear evidence was found for a maximum in ρ with temperature, as previously reported in the literature.

Earlier electrical and optical measurements on n-type PbSe with carrier concentrations between 1×10^{19} and 2×10^{20} cm^{-3} have been extended to n-type samples with electron

concentrations as low as 1.5×10^{18} cm^{-3} and p-type samples with hole concentrations between 3×10^{17} and 5×10^{19} cm^{-3}. Within the scatter of the data, the Hall mobilities at 4.2°, 77°, and 300°K and the thermoelectric power at 300°K are the same for n- and p-type samples with the same carrier concentrations. For both n- and p-type samples with sufficiently high carrier concentrations, the Hall coefficient increases between 77° and 300°K. The maximum value of R_{300}/R_{77} is 1.31 for p-type samples and 1.22 for n-type samples. The effective masses obtained by analysis of reflectivity data are somewhat higher for holes than for electrons, although the data for p-type samples are limited. The effective masses obtained by analysis of the thermoelectric power data on the assumption of acoustic lattice scattering and 4-ellipsoid models for both the conduction and valence bands are somewhat smaller than the reflectivity values or published values based on Faraday rotation experiments.

The effect of NH_3 and H_2S adsorption on the spontaneous bending of thin {111} wafers of GaAs and InSb has been measured. For both these III-V compounds, adsorption of NH_3 decreases the curvature and elastic strain energy and adsorption of H_2S increases the curvature and elastic strain energy.

The system InSb-(β-Sn) has been investigated by measuring the superconducting transition temperature (T_c) as a function of composition for samples prepared by pressing mixtures of InSb and tin at 37 kbar and 450° to 480°C, quenching to room temperature or annealing at 300°C for one hour, and cooling to about −140°C before releasing the pressure. Treatment of the pure materials in this manner gives tetragonal $InSb_{II}$ (T_c = 2.1°K) or tetragonal β-Sn (T_c = 3.7°K). Alloying $InSb_{II}$ with only a few percent tin increases T_c to more than 4°K. A much smaller increase in T_c results from alloying InSb into β-Sn. The measurements indicate that the maximum solubility of β-Sn in $InSh_{II}$ is probably 2.5 to 5 atomic percent and that the maximum solubility of $InSb_{II}$ in β-Sn is probably about 35 atomic percent. In contrast, the maximum solubilities of β-Sn in normal InSb and of normal InSb in β-Sn are reported to be less than 0.5 and about 8 percent, respectively.

An analytical procedure is being developed for determining the three major constituents of HgS-HgSe alloys. After suitable sample treatment, mercury and selenium can he determined by the methods involving potentiometric titrations which were developed earlier for these elements. In initial experiments on the determination of sulfur in standard sulfate solutions, results accurate to within 1 to 2 percent have been obtained by an amperometric method based on titration with a lead solution.

IV. BAND STRUCTURE AND SPECTROSCOPY OF SOLIDS

Considerable progress continues to be made in understanding the band structures of various solid state materials. Extensive calculations of the band-edge structure of the compounds of lead with sulfur, selenium, and tellurium have been made. The results show that extrema of both the conduction and the valence bands probably lie at the (111) edge of the Brillouin zone and that there are six energy bands which influence these extrema. These

six bands interact strongly; therefore, the properties of these compounds vary considerably, and the energy extrema are highly nonparabolic. The quantitative knowledge of the energy levels and Fermi surface of graphite is being improved as further experiments are made with more versatile experimental equipment and samples of higher purity and perfection. In pyrolytic graphite, a semimetal, several low-energy transitions have been seen with a behavior comparable to the "quantum effects" observed in the millimeter cyclotron resonance experiments in semiconductors at high magnetic fields.

The matrix elements in the quantum-mechanical analysis of the Voigt effect have been modified to take into account second-order terms in the magnetic field. In germanium, 18 indirect interband transitions were observed in magnetoabsorption at 74 kgauss. Fine structure was also observed on some of these lines, and studies of this fine structure are now being carried out. Experiments on the behavior of the excited levels of deep impurities with shifts of the band edges due to an applied uniaxial stress are in progress. It is expected that these experiments will clarify the nature of the infrared absorption lines which have been observed in silicon doped with sulfur.

There is also a strong continuing interest in both the theoretical and applied aspects of transport phenomena. The theoretical basis of transport is being broadened by work on generalized master equations, and transport theory under nonhomogeneous conditions is being studied. From the standpoint of application, the properties of Nernst-Ettingshausen refrigerators are being analyzed with particular attention to the optimization of the refrigerator geometry. The properties of a device that uses single-crystal bismuth as a thermoelectric element have also been investigated.

V. MAGNETISM AND RESONANCE

Considerable progress has been made in flux techniques and electrolytic techniques for the growth of stoichiometric ferrites, chromites, and vanadites of the spinel structure and for the growth of a number of bronze crystals. A polytungstate flux has been versatile at permitting predictable results. Preliminary experiments on the systems MnAs-MsSb and MnAs-MnP appear to support our earlier suggestion that the first-order phase change at the Curie temperature of MnAs is due to a partial spin quenching that restabilizes the $B8_1$ phase.

Zero-field AFMR measurements as a function of temperature on powdered $YCrO_3$ give a Néel temperature of 129°K and a critical resonance frequency, extrapolated to 0°K, of ~ 198 kMcps. Measurements of the upper critical field of pure and impure niobium samples have been extended down to 0.4°K with the He^3 refrigerator. The temperature dependence of the attenuation of 70-kMcps longitudinal phonons in x-cut quartz has been measured from 4.2° to 25°K. A signal-to-noise ratio of 20 db has been obtained for the first echo pulse in the best quartz samples.

A theoretical investigation of the elastic magnetic scattering of neutrons at high temperatures has provided a model that permits interpretation of the anomalous "liquid" peaks

sometimes observed experimentally (e.g., near the (111) nuclear position in $MnCr_2O_4$). In order to carry the analysis to lower temperatures, it will be necessary to work out higher terms of an expansion. An investigation of the first-order spin-orbit coupling of a d^5 configuration shows that this interaction gives a highly aspherical contribution to the spin density which increases the neutron diffraction intensity at the same peaks, and on the same order of magnitude, as the spherically symmetric Dzialoshinsky canting responsible for the weak ferromagnetic moment of α-Fe_2O_3. Hence this interaction is probably important for understanding the surprising, highly aspherical ferromagnetic spin-density distribution recently observed in α-Fe_2O_3 by Pickart, Nathans, and Halperin. The influence of magnetostriction on distortions from a spiral-spin configuration have been calculated for MnP. The analysis provides a richness of detail that, if verified experimentally, will permit a strong check for the spin correlations and energy-level diagram that have been assumed for this class of material. A hierarchy of approximations to the Heisenberg ferromagnet problem has been obtained. The method has been used to calculate the Curie temperature T_c, and the susceptibility and magnetization near T_c.

This technical documentary report is approved for distribution.

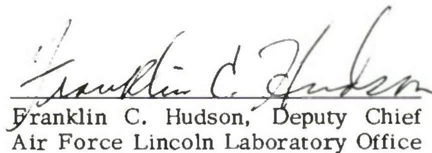

Franklin C. Hudson, Deputy Chief
Air Force Lincoln Laboratory Office

TABLE OF CONTENTS

Introduction iii
Reports by Authors Engaged in Solid State Research xi
Organization xvii

I. SOLID STATE DEVICE RESEARCH 1

A. Magnetic Tuning of CW InSb Diode Laser 1
B. Injection Luminescent Pumping of $CaF_2:U^{3+}$ Lasers 3
C. Growth of $(Ga_xIn_{1-x})As$ Single Crystals by Vapor Phase Reaction 5
D. Infrared Emission from InAs Diodes 9
E. Pill Package for GaAs Laser 10
F. Flatness of Diffused Junctions in GaSb 10
G. Diffused p-n Junction Diodes of Lead Salts 13
H. Dislocation Densities in PbSe 13
I. Growing Helical Density Waves in Semiconductor Plasmas 14
J. Current Instability in GaAs 15
K. Interface-Alloy Epitaxial Heterojunctions 16
L. Melt-Back Epitaxial Heterojunctions 17

II. LASER RESEARCH 21

A. Raman Maser 21
B. Theory of Stimulated Raman Emission 22
C. Energy Levels of d^1 Electrons in Calcium Fluoride 23
D. Intense Sources for Optically Excited GaAs Crystals 25
E. Interferometric Phase-Shift Technique for Measuring Short Fluorescent Lifetimes 27
F. Multilayer Dielectric Films 27
G. Far-Field Photographs of Improved Ruby 28

III. MATERIALS RESEARCH 33

A. Vapor Growth of Crystals by Forced Convection 33
B. Thermoelectric Measurements on High-Resistivity Solids 35
C. Thermoelectric Properties of CrO_2 37

D. Properties of n- and p-Type PbSe 38
E. Adsorption on Spontaneously Bent Wafers of III-V Compounds 41
F. Superconductivity in the High-Pressure InSb-Sn System 41
G. Chemical Analysis of HgS-HgSe Alloys 44

IV. BAND STRUCTURE AND SPECTROSCOPY OF SOLIDS 47

A. Band-Edge Structure of PbS, PbSe, and PbTe 47
B. Magnetoreflection Experiments in Pyrolytic Graphite 47
C. Quantum Theory of the Interband Faraday and Voigt Effects 47
D. Indirect Interband Transition in Germanium 48
E. Effects of Uniaxial Stress on the Infrared Absorption of Sulfur-Doped Silicon 48
F. Derivation and Properties of Generalized Master Equations 48
G. Theory of Transport Equations in Inhomogeneous Driving Fields 49
H. Transport Properties of Bismuth 50
I. Theory of the Infinite-Stage Nernst-Ettingshausen Refrigerator 50
J. Experiments on Room Temperature Nernst-Ettingshausen Refrigerators 51

V. MAGNETISM AND RESONANCE 55

A. Sample Preparation 55
1. Single-Crystal Growth from Polytungstate Fluxes 55
2. A Ceramic Double Cell for Crystal Growth by Fused Salt Electrolysis 57
3. Compounds with B31 $\leftrightarrows$ $B8_1$ Transitions 58

B. Measurements 59
1. Antiferromagnetic Resonance in $YCrO_3$ 59
2. Superconductivity 59
3. Phonon Attenuation in Quartz at 70 kMcps 61

C. Theory 61
1. Elastic Magnetic Scattering of Neutrons 61
2. Aspherical Spin-Density in S-State Cations 63
3. Proposed Spin Configuration for MnP 64
4. Higher-Order Corrections to the Molecular Field Theory of the Magnetic State 65

REPORTS BY AUTHORS ENGAGED IN SOLID STATE RESEARCH

15 October 1963 through 15 January 1964

PUBLISHED REPORTS

Journal Articles*

JA No.			
**1826	Magnetism and Crystal Structure in Nonmetals	J.B. Goodenough	Chapter 9, Magnetism: A Treatise on Modern Theory and Materials, H. Suhl and G.T. Rado, Editors (Academic Press, New York, 1963)
**2035	Cyclotron Resonance and Magneto-Optical Effects in Semiconductors	B. Lax	Proceedings of the International School of Physics Enrico Fermi (Academic Press, New York, 1963)
2041A	Propagation Constants for TE and TM Surface Waves on an Anisotropic Dielectric Cylinder	P.R. Longaker C.S. Roberts†	Trans. IEEE, PTGMTT MTT-11, 543 (1963)
2052	Criterion for Continuous Amplitude Oscillations of Optical Masers	J.I. Kaplan	J. Appl. Phys. 34, 3411 (1963)
2085A	Nernst and Seebeck Coefficients in Bismuth at High Magnetic Fields	T.C. Harman J.M. Honig	Advanced Energy Conversion 3, 525 (1963)
2089A	Galvano-Thermomagnetic Effects in Multi-Band Models	J.M. Honig T.C. Harman	Advanced Energy Conversion 3, 529 (1963)
2112	Directed Heating with Atoms, Electrons and Photons	T.B. Reed	ASM Technical Report No. NY9.1.62
2116	The Reaction of Rare Earth Oxides with a High Temperature Form of Rhodium (III) Oxide	A. Wold R.J. Arnott W. Croft†	Inorg. Chem. 2, 972 (1963)
2137	The Use of CO-CO_2 Atmospheres for the Preparation and Free Energy Determinations of Several Oxide Systems	W. Kunnmann D.B. Rogers A. Wold	J. Phys. Chem. Solids 24, 1535 (1963)

* Reprints available except where indicated by **.

† Author not at Lincoln Laboratory.

JA No.			
2138	Quantum Theory of Kinetic Equations for Electrons in Phonon Fields	P.N. Argyres	Phys. Rev. 132, 1527 (1963)
2141	Second-Order-Exchange Interactions from Spin Wave Resonance	R. Weber P.E. Tannenwald	J. Phys. Chem. Solids 24, 1357 (1963)
2143A	Optical Spectra of Several d^1-Electron Systems	J.R. O'Connor J.H. Chen*	J. Phys. Chem. Solids 24, 1382 (1963)
2153	Microwave Ultrasonics	P.E. Tannenwald	Microwave J. 6, No. 12, 61 (1963)
2155	Properties of GaAs Alloy Diodes	R.H. Rediker T.M. Quist	Solid-State Electronics 6, 657 (1963)
2197	Properties of InAs Diode Masers	I. Melngailis R.H. Rediker	Trans. IEEE, PTGED ED-10, 333 (1963)
2198	Index of Refraction of KDP	J.H. Dennis R.H. Kingston	Appl. Optics 2, 1334 (1963)
2220	High-Pressure Phases of Some Compounds of Groups II-VI	A.N. Mariano E.P. Warekois	Science 142, 672 (1963)
2232	Basic Science at the Crossroads	B. Lax	Microwave J. 7, No. 1, 16 (1964)
2243	High-Pressure Transitions in $A^{(III)} B^{(VI)}$ Compounds. I. Indium Telluride	M.D. Banus R.E. Hanneman M. Strongin† K. Gooen*	Science 142, 662 (1963)
2246	Infrared InSb Laser Diode in High Magnetic Fields	R.J. Phelan A.R. Calawa R.H. Rediker R.J. Keyes B. Lax	Appl. Phys. Letters 3, 143 (1963)
2247	Semiconductor Lasers	B. Lax	Solid State Design 4, No. 11, 26 (1963)
2258	The Laser – A Long Range Future	B. Lax	Solid State Design 4, No. 11, 8 (1963)
2264	Two-Step Raman Scattering in Nitrobenzene	H.J. Zeiger P.E. Tannenwald S. Kern R. Herendeen	Phys. Rev. Letters 11, 419 (1963)

* Author not at Lincoln Laboratory.

† Division 4.

Published Journal Articles (Continued)

JA No.			
2280	Tunable Lasers	R. H. Rediker	Electronic Design 12, No. 1, 47 (1964)
2290	Magnetic Tuning of CW InSb Diode Laser	R. J. Phelan R. H. Rediker	Proc. IEEE (Correspondence) 52, 91 (1964)

MS No.			
**752	Comments on the Lincoln Laboratory GaAs Diode Maser	R. H. Rediker	Laser and Applications, W. S. C. Chang, Editor (Ohio State University, 1963)
779B	Semiconductor Masers	B. Lax	Proceedings of the Symposium on Optical Masers (Polytechnic Institute of Brooklyn Press, 1963)
904	Recent Developments in Plasma Generation	T. B. Reed	Proc. National Electronics Conference, Northwestern University, 28-30 October 1963
910	Injection Lasers and Injection Luminescence	R. H. Rediker	NEREM Record, Boston, 4-6 November 1963
921	Nernst-Ettingshausen Energy Conversion	T. C. Harman	NEREM Record, Boston, 4-6 November 1963

* * * * *

UNPUBLISHED REPORTS

Journal Articles

JA No.			
2193	Theory of the Faraday Effect in Solids	L. M. Roth	Accepted by Phys. Rev.
2202	High Pressure Transition in InSb	R. E. Hanneman M. D. Banus H. C. Gatos	Accepted by J. Phys. Chem. Solids
2219	Preparation and Properties of Sodium and Potassium Molybdenum Bronze Crystals	A. Wold W. Kunnmann R. J. Arnott A. Ferretti	Accepted by Inorg. Chem.
2223	Helium Temperature Ultraviolet Reflectometer for Use with Modified Spectrograph	W. J. Scouler	Accepted by Appl. Optics

JA No.			
2224	Current Regulator for Ultraviolet Light Source	W.J. Scouler E.D. Mills	Accepted by Rev. Sci. Instr.
2225	Reflectivity of HgSe and HgTe from 4 eV to 12 eV at 12°K and 300°K	W.J. Scouler G.B. Wright	Accepted by Phys. Rev.
2241	A Ceramic Double Cell for Crystal Growth by Fused Salt Electrolysis	W. Kunnmann A. Ferretti	Accepted by Rev. Sci. Instr.
2253A	The Nernst-Ettingshausen Energy Conversion Figure of Merit for Bi and Bi-4%Sb Alloys	T.C. Harman J.M. Honig S. Fischler A.E. Paladino	Accepted by Solid-State Electronics
2254	Refined Treatment of the Theory Pertaining to Operating Characteristics of Anisotropic Nernst-Ettingshausen Devices	J.M. Honig B.M. Tarmy	Accepted by J. Appl. Phys.
2260	Bulk Solution of Ginzburg-Landau Equations for Type II Superconductor: Upper Critical Field Region	W.H. Kleiner L.M. Roth S.H. Autler	Accepted by Phys. Rev.
2265	Superconductivity in the High Pressure InSb-Beta Sn System	S.D. Nye M.D. Banus H.C. Gatos	Accepted by Appl. Phys. Letters
2271	Classical Ground State Spin Configurations in the Corundum Lattice	N. Menyuk K. Dwight	Accepted by J. Phys. Chem. Solids
2272	A Cluster Method for Finding Minimum Energy Spin States	D.H. Lyons* T.A. Kaplan	Accepted by J. Phys. Chem. Solids
2275	High Pressure Phase Transition in Tin Telluride	J.A. Kafalas A.N. Mariano	Accepted by Science
2276	Ultrasonic Measurements in Normal and Superconducting Niobium	R. Weber	Accepted by Phys. Rev.
2277	Theory of Spin Resonance and Relaxation	P.N. Argyres P.L. Kelley	Accepted by Phys. Rev.
2282	Cascade Capture of Electrons by Ionized Impurities	D.R. Hamann A.L. McWhorter	Accepted by Phys. Rev.
2293	Growing Helical Density Waves in Semiconductor Plasmas	C.E. Hurwitz A.L. McWhorter	Accepted by Phys. Rev.

* Author not at Lincoln Laboratory.

Unpublished Journal Articles (Continued)

JA No.			
2294	Recombination Radiation from Semiconductors	T.M. Quist	Accepted by Intl. Science and Technology
2302	Injection Luminescent Pumping of $CaF_2:U^{3+}$ Lasers	R.J. Keyes T.M. Quist	Accepted by Appl. Phys. Letters
2303	2000-Ampere Pulse Generator	N.A. Sullivan	Accepted by Rev. Sci. Instr.
2306	Interferometric Phase Shift Techniques for Measuring Short Fluorescent Lifetimes	R.J. Carbone* P.R. Longaker	Accepted by Appl. Phys. Letters
MS No.			
940	Narrow Band vs Localized d Electrons	J.B. Goodenough	Accepted Proc. Buhl Conf. on Materials, Pittsburgh, 31 October – 1 November 1963
941	Spin Correlations Among Narrow Band Electrons	J.B. Goodenough	Accepted by J. Appl. Phys. (Magnetism and Magnetic Materials Conference, Atlantic City, 12-15 November 1963)
943	Electrical Conductivity in the Spinel System $Co_{1-x}Li_xV_2O_4$	D.B. Rogers J.B. Goodenough A. Wold	Accepted by J. Appl. Phys. (Magnetism and Magnetic Materials Conference, Atlantic City, 12-15 November 1963)

Meeting Speeches†

MS No.			
924A	Semiconductor Injection Lasers	R.H. Rediker	New England Section, Optical Society of America, Waltham, 17 October 1963
934	Pressure Measurement and Efficiency in a Tetrahedral Anvil Press as Related to Anvil and Pyrophyllite Size	M.D. Banus S.D. Nye J.A. Kafalas	ASME Annual Meeting, Philadelphia, 17-22 November 1963
936	The $CaWO_4/Nd^{3+}(Na^+)$ Optical Maser: Wavelength and Polarization Dependence on Resonator Geometry	D.F. Edwards	American Physical Society, Chicago, 18-19 October 1963
938	Applications of Spark Source Mass Spectroscopy	E.B. Owens	Eastern Analytical Symposium, New York, 15 November 1963
957	Applications of Semiconductor Lasers	A.L. McWhorter B. Lax	First National Conference on Laser Technology, San Diego, 12-14 November 1963

* Division 4.

† Titles of Meeting Speeches are listed for information only. No copies are available for distribution.

Unpublished Meeting Speeches (Continued)

MS No.			
959	A Cluster Calculation of Magnetic Properties	G. F. Dresselhaus	Solid State Physics Seminar, Yale University, 18 October 1963
963A	Injection Lasers	R. H. Rediker	M.I.T., 25 October 1963
965	InSb CW Diode Laser	R. J. Phelan R. H. Rediker	American Physical Society, Pasadena, 19-21 December 1963
983	Stoichiometry of Electronic Materials	A. J. Strauss	Industrial Liaison Symposium, M.I.T., 18 December 1963
987	Crystal Growth at Lincoln Laboratory	T. B. Reed	Industrial Liaison Symposium, M.I.T., 18 December 1963
984	Masers and Magneto-Optics	B. Lax	Optical Society of America, Chicago, 23-25 October 1963
1008	Injection Lasers	R. H. Rediker	Princeton University, 11 December 1963
1024	Stimulated Raman Emission	H. J. Zeiger	Physics Colloquium, Brandeis University, 19 January 1964

For convenience in ordering copies of Lincoln Laboratory reports, DDC (formerly ASTIA) and H numbers are listed. Reports assigned H numbers are unclassified (released) and are obtainable at cost as microfilm or photoprint copies from the Microreproduction Laboratory, Hayden Memorial Library, M.I.T., Cambridge, Massachusetts 02139.

ORGANIZATION

DIVISION OFFICE

Benjamin Lax, *Division Head*
A. L. McWhorter, *Associate Head*
P. E. Tannenwald, *Assistant Head*
M. J. Hudson, *Assistant*
D. T. Stevenson*

GROUP 81

J. M. Honig, *Leader*
T. C. Harman, *Assistant Leader*

Argyres, P. N.
Brebrick, R. F.
Chapin, D. S.
Dresselhaus, G. F.
Duston, D. K.†
Gottschalk, M.
Hilsenrath, S.
Houghton, B. H.*
Kelley, P. L.
Kleiner, W. H.
Litvak, M. M.
Mason, V. J.
Paladino, A. E.
Rawson, N. B.
Sillers, S. J.
Wilner, M. H.
Work, C. C.

GROUP 82

J. B. Goodenough, *Leader*
H. J. Zeiger, *Associate Leader*

Arnott, R. J.
Delaney, E. J.
Dwight, K., Jr.
Feldman, B.
Ferretti, A.
Germann, R. W.
Kaplan, T. A.
Kern, S.
Kernan, W. C.
Kunnmann, W.
Larson, E. G.*
Menyuk, N.
Newman, W. A.
Perry, F. H.
Ridgley, D. H.
Rogers, D. B.
Rosenblum, E. S.
Stickler, J. J.
Thaxter, J. B.
Weber, R.

GROUP 83

E. P. Warekois, *Leader*
A. J. Strauss, *Assistant Leader*

Andrews, H. I.†
Bachner, F. J.†
Banus, M. D.
Button, M. J.
Carter, F. B.
Cornwell, J. C.
Ehlers, H. H.
Fahey, R. E.
Farrell, L. B.
Finn, M. C.
Fischler, S.
Gardels, M. C.
Giardino, N. A.
Kafalas, J. A.
LaFleur, W. J.
Lavine, M. C.*
Nye, S. D.†
Owens, E. B.
Plonko, M. C.
Reed, T. B.
Roddy, J. T.
Siuta, V. P.†

GROUP 84

J. G. Mavroides, *Leader*
G. B. Wright, *Assistant Leader*

Brown, J. P.
Curran, E. A.
Dickey, D. H.
Dimmock, J. O.
Dresselhaus, M. S.
Edwards, D. F.
Fulton, M. J.
Halpern, J.‡
Kolesar, D. F.
Krag, W. E.
Mason, W. C.
Scouler, W. J.

GROUP 85

R. H. Rediker, *Leader*
R. J. Keyes, *Assistant Leader*

Bates, D. H.
Butler, J. F.
Calawa, A. R.
Caswell, F. H.
Clough, T. F.
Donaldson, P. L.
Foyt, A. G.‡
Grant, C. R.
Hinkley, E. D., Jr.
Hurwitz, C. E.
May, W. G.†
Melngailis, I.
Palermo, J. S.
Phelan, R. J.
Quist, T. M.
Sirrine, R. C.
Stopek, S.
Sullivan, F. M.
Sullivan, N.
Ward, J. H. R., III
Youtz, P.

GROUP 86

R. H. Kingston, *Leader*
F. L. McNamara, *Associate Leader*

Billups, R. R.
Chatterton, E. J., Jr.
Dennis, J. H.
Longaker, P. R.
O'Connor, J. R.
Pitts, R. F.
Rotstein, J.
Schlickman, J. J.
Tank, C. C. M.
Underwood, D. I.
Wong, G. W.
Ziegler, H. L.
Zieman, H. E.
Zimmerman, M. D.

---

* Part Time
† Research Assistant
‡ Staff Associate

I. SOLID STATE DEVICE RESEARCH

A. MAGNETIC TUNING OF CW InSb DIODE LASER

Diode lasers of InSb have been reported[1] which have operated on a pulse basis in the presence of a longitudinal magnetic field. By varying the intensity of this magnetic field, a relatively large shift in the wavelength of the stimulated emission was also observed. We have now operated forward-biased InSb diodes as CW lasers, and have been able to change the emission wavelength in steps of 50 Å from one cavity mode to an adjacent one by applying incremental steps of magnetic field of less than 600 gauss.

The diodes were similar to those reported previously, except that the net carrier concentration at 77°K of the single-crystal n-type InSb from which the diodes were made was reduced by a factor of about twenty to 4.8×10^{14} cm^{-3}. The corresponding Hall mobility at 77°K, for the diodes to be reported here, was 4.3×10^{5} cm^{-1} $volt^{-1}$ sec^{-1}. As reported previously,[1] in order to obtain laser action at available diode forward currents, a magnetic field parallel to the direction of the junction current of the order of 20 kgauss was required. By going to the purer material, however, the threshold current density at a given magnetic field has been reduced (at 27 kgauss and 2°K, J_T = 1400 amp cm^{-2} vs 3500 amp cm^{-2} for the more heavily doped material[1]). Because of this reduced threshold, it has been possible to operate the lasers CW.

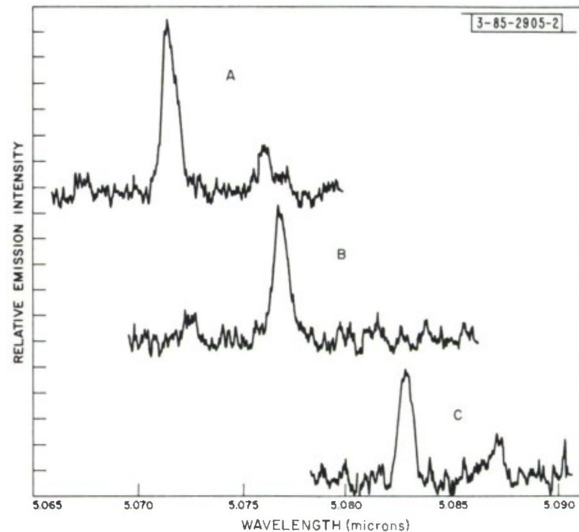

Fig. I-1. Spectra of CW emission from InSb diode laser at 2°K and 1-amp DC forward current. The applied longitudinal magnetic field for spectrum A was 52 kgauss and was reduced in steps of 530 gauss to obtain spectra B and C.

Figure I-1 shows the CW emission spectra for a diode operating at 2°K with a current of 1-amp DC. The applied longitudinal magnetic field for the spectrum A at the top of the figure was 52 kgauss. Spectrum B was obtained by reducing the magnetic field by 530 gauss, and spectrum C was obtained by a further reduction of 530 gauss. Both the absolute value and the incremental values of the magnetic field have been determined to within 3 percent. As is evident from the figure, the emission wavelength has been tuned from one cavity mode to an adjacent one by

varying the magnetic field by less than 600 gauss. Although this tuning has been shown in Fig. I-1 for magnetic fields near 50 kgauss, other magnetic fields above the minimum required for laser action could have been used for the illustrative purposes.

There is also an effect of the magnetic field on the refractive index n as evidenced by the shift to shorter wavelength of a given cavity mode as the magnetic field is increased (Fig. I-1, A and B). This shift for InSb is 15 Å $kgauss^{-1}$ as compared with a similar shift which has been previously reported[2] for InAs lasers of 3 Å $kgauss^{-1}$. The decrease in the index of refraction at a given wavelength as the magnetic field is increased is expected because this wavelength becomes more removed from that corresponding to the bandgap, and the index of refraction is a decreasing function of the wavelength at the bandgap. The increase in the bandgap energy with magnetic field also produced the change in the spectrum of the spontaneous emission which causes the modes to switch to shorter wavelengths as illustrated in Fig. I-1.

The measured half-width of 8 Å of the main emission lines in Fig. I-1 corresponds to the resolution of the grating spectrometer used. While essentially single-mode operation of the CW InSb laser is shown in Fig. I-1, multimode operation at a given magnetic field can be obtained by increasing the diode current. At a given magnetic field, the spacing between adjacent cavity modes is about 45 Å. The length between the cleaved surfaces which define the cavity for the diode of Fig. I-1 was 0.051 cm. From the mode spacing $\Delta\lambda$ and the cavity length L, one can determine

$$[n_o - \lambda_o \frac{dn}{d\lambda}] = \frac{\lambda_o^2}{2L\Delta\lambda} = 5.9 \quad . \qquad (1)$$

Moss[3] has determined both the refractive index n and $(dn/d\lambda)$ near the bandgap energy for InSb at 300°K for <u>zero</u> magnetic field. Using his value for n_o of 4.0 and for $(dn/d\lambda)$ of 0.1 $micron^{-1}$, one obtains, for the left-hand side of Eq. (1), a value of 4.5. The quantity $(dn/d\lambda)$ increases very rapidly near the bandgap, and an increase in this number by a factor of about four can explain the experimentally determined mode spacing. Both n and $(dn/d\lambda)$ should differ from the data of Moss because of the effects of the low temperatures and magnetic fields used in our experiments.

R. J. Phelan
R. H. Rediker

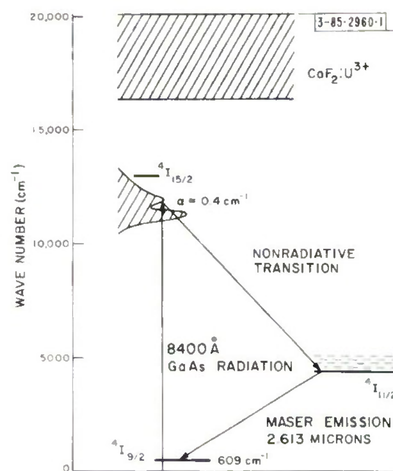

Fig. I-2. Energy-level diagram of U^{3+} in CaF_2 showing the laser transition and absorption in the vicinity of the GaAs radiation.

B. INJECTION LUMINESCENT PUMPING OF $CaF_2:U^{3+}$ LASERS

The usual methods of the optical pumping of solid state lasers by means of gas discharge tubes or tungsten filaments are inefficient in the conversion of pump power to laser radiation. For low-energy output lasers, this low efficiency is not serious, but for high-power devices it may well be a limiting factor. We shall describe a new method of optical pumping, using injection luminescence from a semiconductor diode, which should lead to more efficient pumping. In particular, we shall describe the pumping of a $CaF_2:U^{3+}$ laser with the light output from GaAs diode lasers.

The pertinent energy levels associated with the U^{3+} ion in CaF_2 are shown in Fig. I-2. Absorption of the GaAs diode radiation at 0.84 micron excites an electron from the ground state to the $^4I_{15/2}$ levels. Rapid nonradiative recombination to the $^4I_{11/2}$ levels is followed by radiative recombination to either the $^4I_{9/2}$ level or the ground state. Laser action initially occurs at 2.61 microns between the lowest $^4I_{11/2}$ level and the splitoff $^4I_{9/2}$ state. The absorption spectrum of the $^4I_{15/2}$ levels is indicated in the drawing. It should be noted that the absorption coefficient in the region of the GaAs excitation radiation is only $0.4\ cm^{-1}$. For this reason, it was necessary to insert the 3-mm diameter $CaF_2:U^{3+}$ rod into an integrating chamber in order to absorb the 0.84-micron radiation effectively. Figure I-3 is an artist's sketch of the diode pump. Basically, the pump consists of five GaAs laser diodes electrically connected in series and mounted along the slit of an integrating chamber. At injection currents of 6 amp, the bank delivered 4.5 watts of monochromatic radiation (0.84 micron) to the integrating chamber.

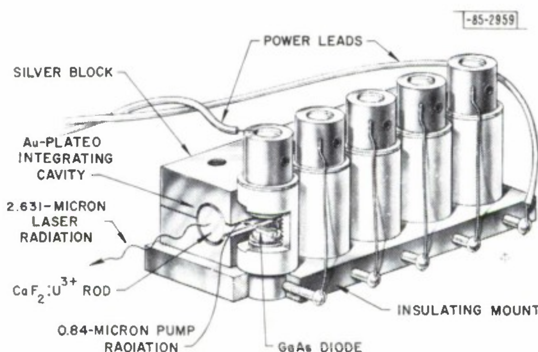

Fig. I-3. Artist's representation of GaAs pump and laser crystal.

The integrating chamber was formed by milling a 3.3-mm hole in a 3-cm-long silver block. The 4-cm-long-by-3-mm-diameter laser* rod of CaF_2:0.1% U^{3+} had confocal ends with silver coatings of zero and 1 percent transmission. The entire assembly, suspended from a quartz light pipe, was inserted in a liquid-helium dewar. The $CaF_2:U^{3+}$ radiation emerging from the quartz pipe was measured using a photovoltaic InSb detector. A germanium filter at room temperature prevented any of the GaAs radiation from reaching the detector. The signal from the InSb detector and the current through the pump diodes were simultaneously monitored on separate beams of a dual-beam oscilloscope. A previous calibration of the radiation from the diodes as a function of injection current permitted the translation of diode current to input radiation.

* Supplied by Walter Hargraves of Opto-Vac Company.

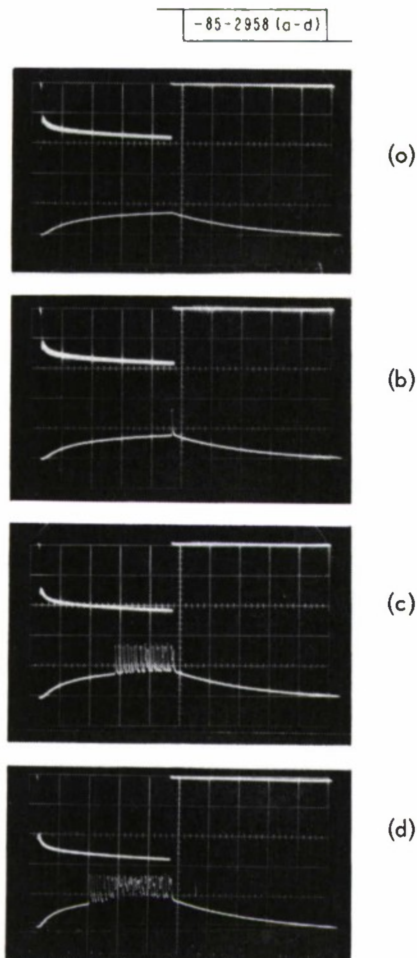

Fig. I-4. Oscilloscope troces showing U^{3+} emission for vorious pump intensities ot 4.2°K. The top troce in eoch photogroph represents the diode current (2 omp div^{-1}) ond the lower troce represents the loser emission. The time scole is 100 µsec div^{-1}.

Figure I-4(a-d) shows a sequence of the photographs taken from the oscilloscope. In each picture, the diode current on the upper trace appears as a negative deflection, and the detector signal on the lower trace appears as a positive deflection. Each division of vertical deflection of the diode current represents approximately 1.5 watts of 8400-Å radiation into the laser rod. The time base is 100 µsec per division. Just below threshold [Fig. I-4(a)], one observes the normal 2.631-micron fluorescence of the U^{3+} with its characteristic 130-µsec decay time. At very slightly higher input power [Fig. I-4(b)], laser action is observed as a single spike that appears at the end of the pulse and, as the current is increased further above threshold [Figs. I-4(c) and (d)], the spiking begins earlier in the pulse and persists to its termination. In these photographs, the amplitude of the laser spikes relative to the fluorescence is not truly represented, because of detector saturation. When the output radiation is sufficiently attenuated before it reaches the detector, the fluorescence is imperceptibly small compared with the laser spikes. No attempt was made to measure the absolute intensity of the laser output radiation.

With longer current pulses, up to 3 msec at a repetition rate of 10 pps, it was found that the laser showed spiking over the entire pulse length. This is somewhat in disagreement with the observations of laser action in this material reported by Sorokin and Stevenson,[4] in which spiking was found to cease after a few milliseconds.

By using fast fall-time current pulses into the diodes, one could, in principle, determine the relaxation time from the $^4I_{15/2}$ levels to the $^4I_{11/2}$ laser level. We were not able to determine this lifetime with our present equipment but have established that it was less than the 3-μsec RC time constant of the detector circuit.

It has been shown that the radiation emitted by GaAs laser diodes can be effectively used as an optical pump source for other laser materials. The reproducibility and the precise control of the intensity and speed of this source make it an ideal tool for studying the relaxation parameters of other fluorescent materials. Intrinsically, this new source is capable of modulation up to 500 Mcps, and hence can simultaneously serve both as a pump and as a method of superimposing information on the laser beam.

Perhaps the most useful aspect of injection luminescent pumping lies in its efficiency of conversion of input electrical power into useful pump radiation. For presently available GaAs diodes, this efficiency approaches 50 percent. By using mixed semiconductor crystals, we can, in principle, tailor the luminescence wavelength to ideally match a particular laser material, and thus make the conversion of the pump radiation to laser radiation also very high. For example, high efficiency should be obtainable by using $(Ga_xIn_{1-x})As$ diodes radiating at 8750 Å in conjunction with Nd^{3+} lasers. Theoretically, this system should be 80 percent efficient in the conversion of pump output power to 1.06-micron laser beam power. In addition to being much more efficient than the standard flash-tube pumps (<6 percent), the injection luminescent pumping would reduce the heat dissipation in the pumped laser by a factor of at least ten over that of flash-tube pumping. This reduction in heat dissipation should significantly reduce the thermal gradient problems that plague high-energy lasers.

R. J. Keyes
T. M. Quist

C. GROWTH OF $(Ga_xIn_{1-x})As$ SINGLE CRYSTALS BY VAPOR PHASE REACTION

The epitaxial growth of single-crystal III-V compounds by the halogen disproportionation mechanism in both open and closed systems has been reported by a number of people.[5-8] The nonseeded growth of polycrystals has been discussed by Holonyak and coworkers.[9] This note deals with the nonseeded growth of single mixed crystals $(Ga_xIn_{1-x})As$ grown by the halogen vapor-transport mechanism in a closed system.

There is considerable advantage to growing mixed single crystals in the closed-tube process. The material can be homogenized by transporting several times before the final crystal is grown. The crystal grows with large, atomically flat faces, which are suitable for injection laser fabrication without polishing.

Polycrystals grown by this method usually contain large crystallites; therefore, the problem in growing single crystals is to control the initial nucleation. The geometry of the reaction vessel, the method of removing the heat of crystallization, and the temperature profile of the furnace have been found to influence this initial nucleation. The reaction vessel used is shown in Fig. I-5(a). The desired amounts of GaAs and InAs are placed in the tube along with a few milligrams of arsenic and a dopant, usually selenium. The vessel is pumped down to approximately 10^{-6} torr, back-filled with Cl_2 and sealed off. The vessel is placed in a furnace with a profile as shown in Fig. I-5(b). In growing the final crystal, the tube is positioned as shown. In order to grow single

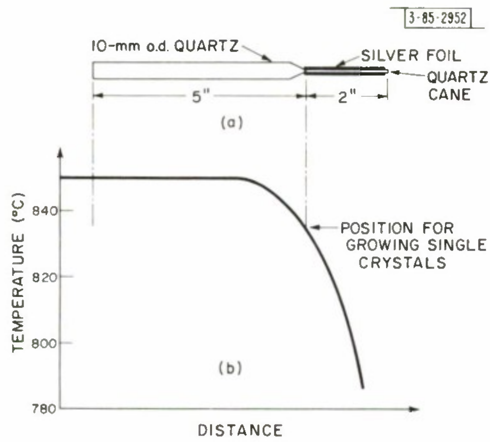

Fig. I-5. Reaction vessel positioned for growing single crystals: (a) reaction vessel; (b) temperature profile of furnace.

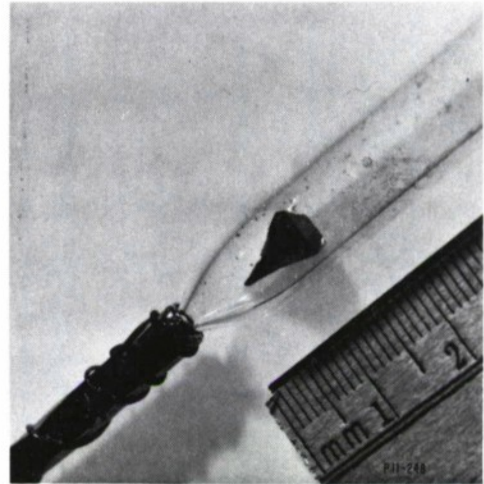

Fig. I-6. Single crystal of $(Ga_{0.95}In_{0.05})As$ inside reaction vessel.

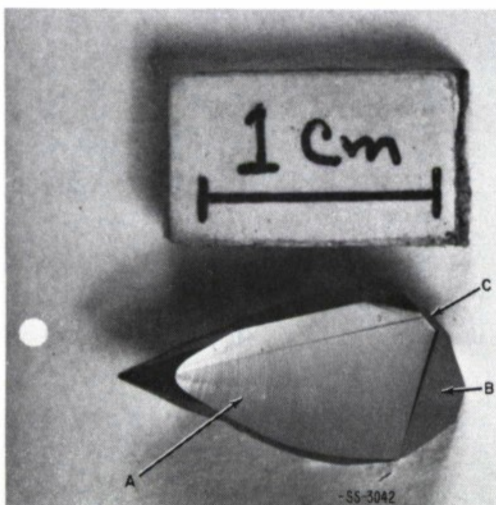

Fig. I-7. Crystal of $(Ga_{0.97}In_{0.03})As$.

crystals, the transport rate must be very slow. The slow growth rate is accomplished by having a small temperature difference between the source and the tip. The heat sink drops the temperature at the tip about 10°C, insuring that nucleation starts at the tip. After the crystal is nucleated, the heat conductivity of the metal, plus the preferential reaction on the metal rather than on on the quartz, causes the crystal to grow out toward the quartz wall.

Figure I-6 shows a $(Ga_{0.95}In_{0.05})As$ crystal grown according to the above discussion. The crystal, which was loosely bonded to the quartz, has been moved back from the tip by gentle tapping. The crystal was photographed while still in the quartz vessel, and the spots seen on the top face are actually on the quartz. Figure I-7 shows another crystal $[(Ga_{0.97}In_{0.03})As]$ in its "as grown" shape. The top face (labeled A) is a (111) plane. The other side of the crystal contains a face parallel to the A face shown. The face labeled B in the figure is a (111) face and the face labeled C is a (211) face. The line on face A also appears on the opposite side of the crystal and indicates that the crystal is twinned. However, x-ray patterns shot on either side and straddling the line are identical. Figure I-8 is an interference pattern of the line and indicates a shallow furrow. The ring structure seen on the top surface cannot be detected on the interference microscope.

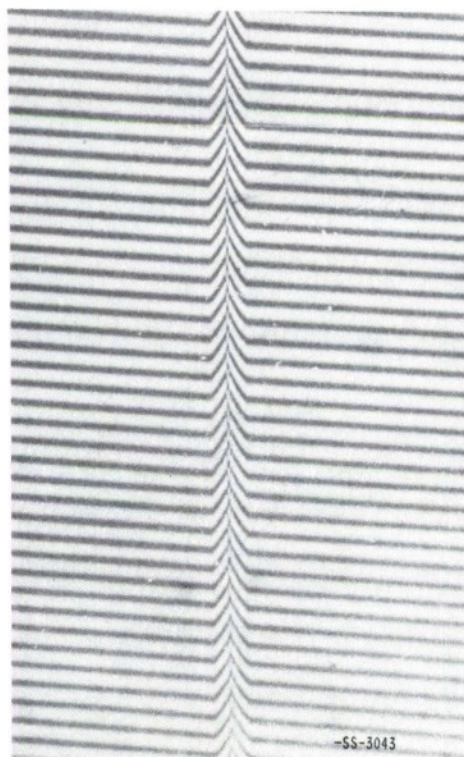

Fig. I-8. Interference pattern showing furrow at twin line in face A.

The compositions involving several percent of indium were chosen in the search for injection lasers at 8800 Å, a wavelength needed to pump a Nd^{3+} in CaF_2 laser. Single crystals have also been grown of $(Ga_{0.20}In_{0.80})As$, which in this case produced coherent light at 2.4 microns. Growing single crystals on the indium-rich side requires a larger temperature difference between source and tip than gallium-rich compositions.

R. C. Sirrine

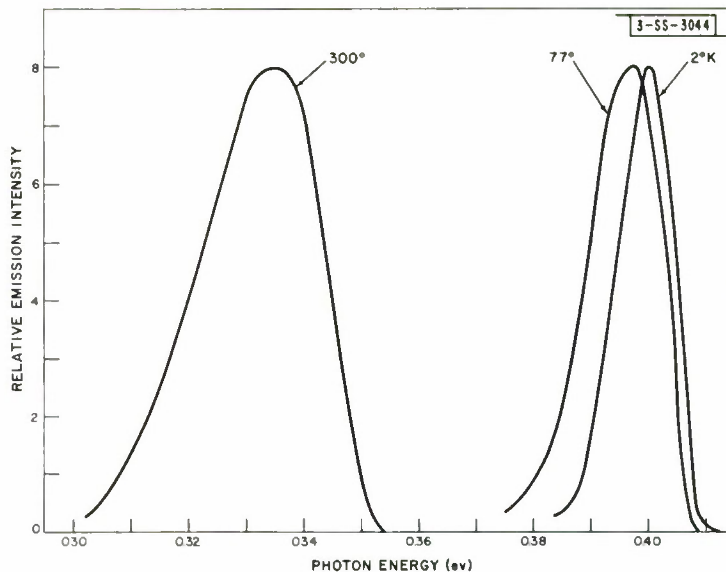

Fig. I-9. Emission spectra at 300°, 77°, and 2°K for a Zn-diffused InAs diode with net donor concentration in base region of 2×10^{16} cm^{-3}. The spectra are not plotted to the same intensity scale.

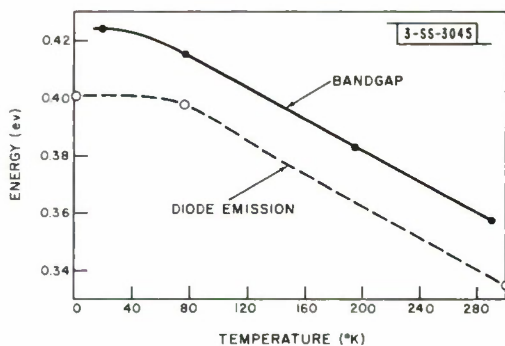

Fig. I-10. Comparison of the temperature variation of the InAs bandgap (after Dixon and Ellis[11]) with the temperature variation of the diode emission energy.

D. INFRARED EMISSION FROM InAs DIODES

We have previously reported infrared radiation near 3 microns in forward-biased InAs diodes at 77° and 4.2°K.[10] With a more sensitive detection system, it is now also possible to measure the room temperature (300°K) spectrum of these diodes and to observe at 2°K additional low-intensity structure in the diode spectrum at energies lower than the energy of the main peak.

To achieve greater sensitivity, the diode current was chopped electronically at 1.8 kcps; the signal was detected with an InSb photovoltaic detector, and was amplified by a narrow-band amplifier. Figure I-9 shows the spectrum at 300° and spectra at 77° and 2°K for a diode fabricated by diffusing Zn into an n-type base with a donor concentration of 2×10^{16} cm^{-3}. The intensity scale is different for each temperature. Actually the energy of the radiation integrated over the spectrum is about one order of magnitude lower at 300°K than at 77°K. The emission line at 300°K occurs at 0.335 ev or 3.7 microns and has a half-width of 25 mev, compared with 12 mev at 2°K. Figure I-10 compares the temperature variation of the photon energy at the diode emission peak with the temperature variation of the optical bandgap published by Dixon and Ellis[11] for n-type InAs of comparable purity. On the basis of two points, the diode emission line follows closely the bandgap variation between 298° and 77°K, at an energy about 20 mev below the gap energy. At lower temperatures, the shift of the diode emission seems to be less than the change in the gap.

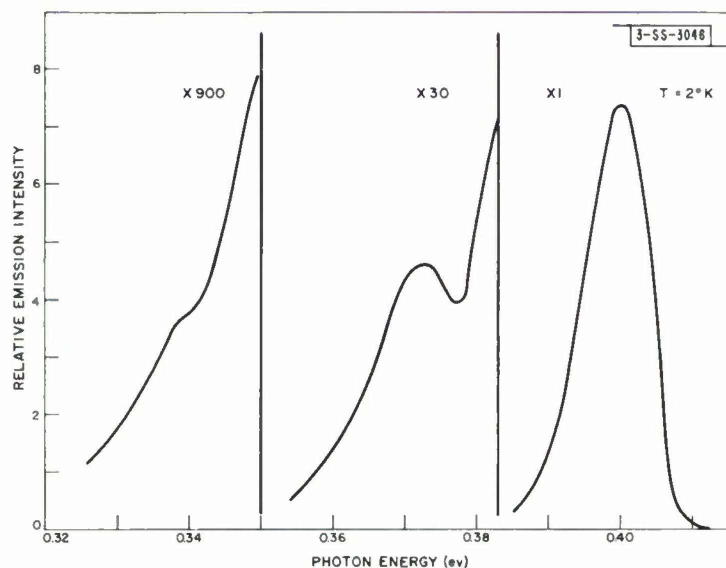

Fig. I-11. Emission spectrum of an InAs diode at 2°K. The intensity scale is expanded twice as the photon energy decreases.

Figure I-11 shows the spectrum of the same diode at 2°K with details of the low-energy tail on successively expanded scales. An additional peak occurs at 0.372 ev, 30 mev below the main emission peak, and a knee is observed at 0.34 ev.

I. Melngailis

E. PILL PACKAGE FOR GaAs LASER

A miniature "pill" package has been developed for GaAs injection lasers which will be used in high-power pulse applications. This package has the advantage of low inductance, and consequently will allow more efficient high-frequency modulation of the diode. It should also be easier to cool than the larger package described in the last Solid State Research report and, of course, its smaller size is an advantage *per se*, when volume and weight must be minimized.

The package consists of a GaAs laser and two semi-insulating GaAs spacers alloyed between two 0.080-inch-diameter metallic disks. The unit is less than 0.025-inch thick. An artist's conception of the package is shown in Fig. I-12.

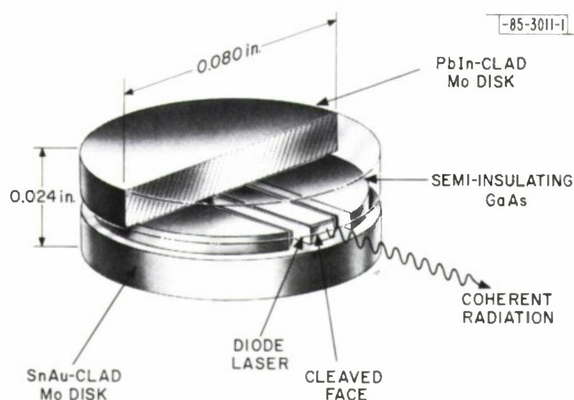

Fig. I-12. Artist's representation of miniature "pill" laser package.

In the fabrication of this unit, the p-surface of the 0.043 × 0.009 × 0.004-inch-thick GaAs laser and the two semi-insulating GaAs spacers of identical thickness, are simultaneously alloyed onto a PbIn-clad molybdenum disk. The alloying is done in a controlled atmosphere chamber at about 300°C. Finally a tin-clad molybdenum disk is alloyed onto the n-surface of the laser, so that it also wets to the GaAs spacers. In this case, the alloying is done at a temperature of about 200°C. The quality of the alloyed joints is of concern, since they serve as heat conduction paths and electrical connections.

Lasers in the "pill" package have been supplied to other groups in the Laboratory for use in optical radar development.

J. S. Palermo

F. FLATNESS OF DIFFUSED JUNCTIONS IN GaSb

In GaAs, it has been observed[12,13] that a lack of flatness in the indiffused junction usually results in higher threshold currents for laser action. In some cases, no lasing action is observed at any current.

In GaSb, laser action has not yet been achieved. Diffused junctions in GaSb have been investigated to determine the degree of flatness achieved under different diffusion conditions with the end goal of producing laser structures which have flat junctions. If the lack of flatness in the GaSb junctions has been the cause for the inability to fabricate injection lasers of GaSb, the program will hopefully lead to the realization of the GaSb laser.

Results are presented for zinc diffusion in GaSb doped with tellurium to a net donor concentration of 1×10^{18} cm^{-3}. Similar results were obtained with selenium-doped samples. The surfaces into which the zinc was to be diffused were either mechanically and chemically polished optically flat, ground to a fine matted finish with 4-micron garnet, or cleaved. GaSb cleaves along the (110) planes. The polished or ground surfaces were either (111), (100), or (110). No orientation effects were observed. The source material consisted of an alloy of gallium and zinc with the zinc concentration varying from 2.0 to 10.0 percent by weight. The sample and source were placed in a sealed, evacuated quartz tube.

Figure I-13 is a cross-sectional photograph of a junction formed by diffusing into a polished GaSb surface for 16 hours at 650°C from a source alloy of 10-percent zinc. The photograph is of a cleaved surface etched with a solution of $67H_2O{:}13HF{:}20HNO_3$ heated to 55°C.[14] If one assumes that the width of the inversion layer is of the order of a micron, the 2- to 3-micron junction irregularities shown here could be a source of trouble.

Figure I-14 shows a p-n junction formed by diffusing into two ground surfaces and one cleaved surface of a piece of GaSb for 16 hours at 650°C. The source alloy was 10-percent zinc. The ground surfaces were finished with 4-micron garnet. Note that the junction depth is about three times larger from the ground surface than it is from the cleaved surface. The rounding of the junction along the edges of the cleaved surface suggests that this is due to the higher effective surface concentration of zinc along the ground surface. Also, the junction along the ground surfaces is as flat or flatter than that along the cleaved surface. The large abrupt voids in the junction line are believed due to poor junction delineation. In a subsequent diffusion, the surface concentration was decreased by diluting the source alloy to 2.0-percent zinc. The diffusion was then performed for 90 hours at 650°C. This junction is illustrated in Fig. I-15. The reduced penetration is a result of the lower zinc concentration. The junction has larger irregularities and it is noticeable that the surface defects were essentially reproduced in the junction plane. The large defects on the surface are believed due to thermal etching. Thus it seems that the junction plane becomes more surface dependent when low diffusant concentrations are used. Figure I-16 illustrates the results when the diffusant concentration is increased to 4 percent. In this 60-hour diffusion at 650°C, the surface effects are less pronounced than those shown in Fig. I-15. These preliminary studies indicate that junction flatness becomes less dependent on surface defects as the surface concentration of zinc is increased.

The junction flatness variation along cleaved surfaces, such as illustrated in Fig. I-14, is believed to be due to poor cleaving rather than to defects in the bulk crystal. A 90-hour diffusion at 650°C into a well-cleaved surface, using a 2.0-percent zinc concentration in the source alloy, did produce a junction which is flat to within one micron over the entire surface. This, however, was an exception and has occurred only once. There is as yet no evidence that the bulk properties of the crystal are responsible for any of the junction variations. Another difficulty encountered in the diffusion of zinc into GaSb is that stresses are introduced into the crystal with short, high-temperature diffusions and rapid quenching, as illustrated in Fig. I-17. The photograph is of a cleaved surface which has had no delineation treatment at all. The p-n junction which was checked by thermal probing is clearly defined. The striations extending perpendicularly from the surface to the junction are irregularities in the cleaved surface, and are believed to be due

-SS-3047

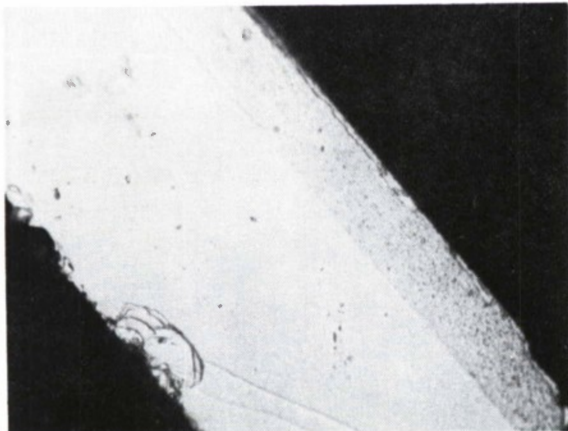

Fig. I-13. Cross section (magnified 500X) of junction formed by diffusing into polished surface for 16 hours at 650°C from 10-percent Zn in Zn-Ga source. The junction has been delineated by etching with a solution $67H_2O:13HF:20HNO_3$ at 55°C.

-SS-3048

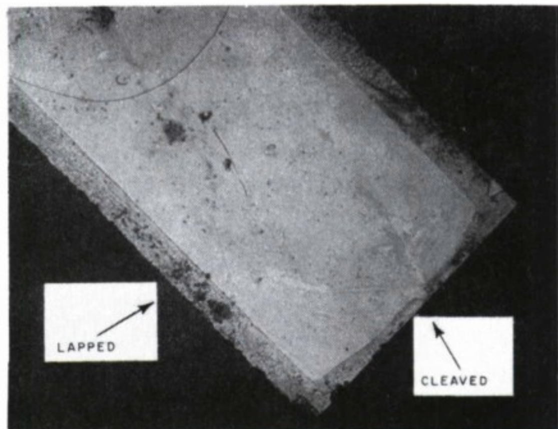

Fig. I-14. Cross section (magnified 200X) of junction formed by diffusing into two ground and one cleaved surfaces for 16 hours at 650°C with 10-percent Zn in Zn-Ga source. The junction has been delineated by etching with a solution $67H_2O:13HF:20HNO_3$ at 55°C.

-SS-3049

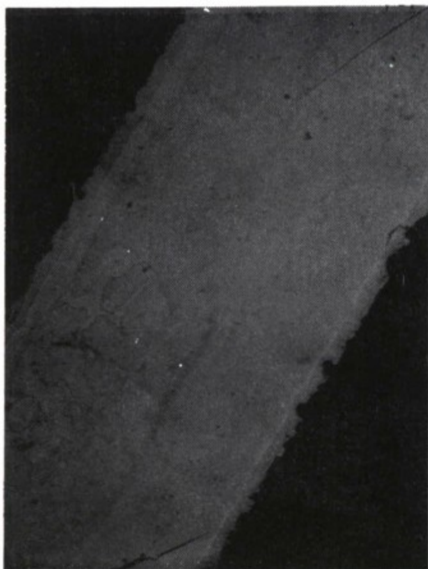

Fig. I-15. Cross section (magnified 200X) of junction formed by diffusing into ground surface for 90 hours at 650°C with 2-percent Zn in Zn-Ga source. The junction has been delineated by etching with a solution $67H_2O:13HF:20HNO_3$ at 55°C.

-SS-3050

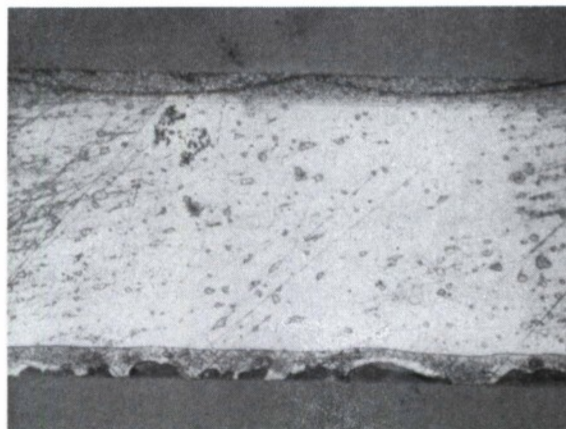

Fig. I-16. Cross section (magnified 200X) of junction formed by diffusing into ground surface for 60 hours at 650°C from 4-percent Zn in Zn-Ga source. The junction has been delineated by etching with a solution $67H_2O:13HF:20HNO_3$ at 55°C.

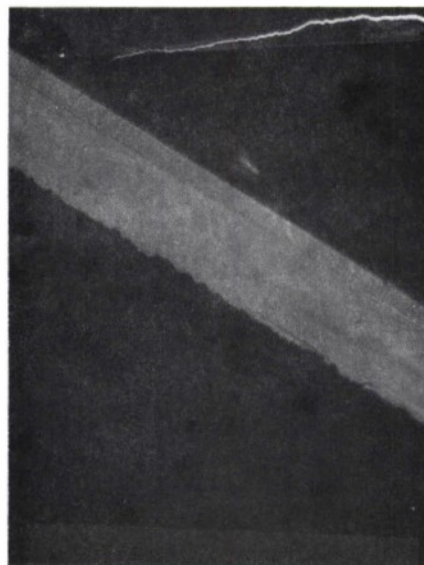

Fig. I-17. Cross section (magnified 200X) of junction formed by diffusing at 660°C for 3 hours from Zn-Ga source with 10-percent Zn concentration. Diffusion was followed by rapid water quench. The photograph is of a cleaved surface which has not been etched.

to strains in the crystal caused by the zinc diffusion. The diffusion was performed at 660°C for 3.5 hours from a source with a 10-percent zinc concentration and was followed by a rapid quench in cold water.

Further diffusion studies are being performed. The flattest junctions are being used to fabricate diodes with a laser structure.[15]

A. R. Calawa

G. DIFFUSED p-n JUNCTION DIODES OF LEAD SALTS

Diffused p-n junction diodes have been fabricated with PbTe and PbSe. The procedure, as outlined previously[16] for PbSe, utilizes an interdiffusion mechanism to introduce controlled deviations from stoichiometry and is a modification of a method developed by Brebrick and Gubner,[17] and Brebrick and Allgaier[18] to study composition stability limits. As is well known, excess lead gives rise to n-type, and excess selenium and tellurium to p-type PbSe and PbTe, respectively. An analysis of experiments based on Fick's law diffusion results in the following effective interdiffusion constants: $D_{\Delta} = 4 \times 10^{-8}\ cm^2\ sec^{-1}$ for producing a p-layer on n-type PbSe at 600°C; $D_{\Delta} = 9 \times 10^{-9}\ cm^2\ sec^{-1}$ for an n-layer on p-type PbSe at 650°C; $D_{\Delta} = 6 \times 10^{-7}\ cm^2\ sec^{-1}$ for an n-layer on p-type PbTe at 650°C. In the first case, the diffusion has been studied as a function of diffusion time, and the results show that the assumption of simple Fick's law diffusion is valid. Diode electrical characteristics have been studied and can be explained as resulting from a combination of diffusion and tunneling current components.

An article describing this work has been submitted to the Journal of the Electrochemical Society.

J. F. Butler

H. DISLOCATION DENSITIES IN PbSe

Dislocation densities in PbSe crystals have been determined by producing etch pits on freshly cleaved surfaces and assuming a one-to-one correspondence between etch pits and dislocations.

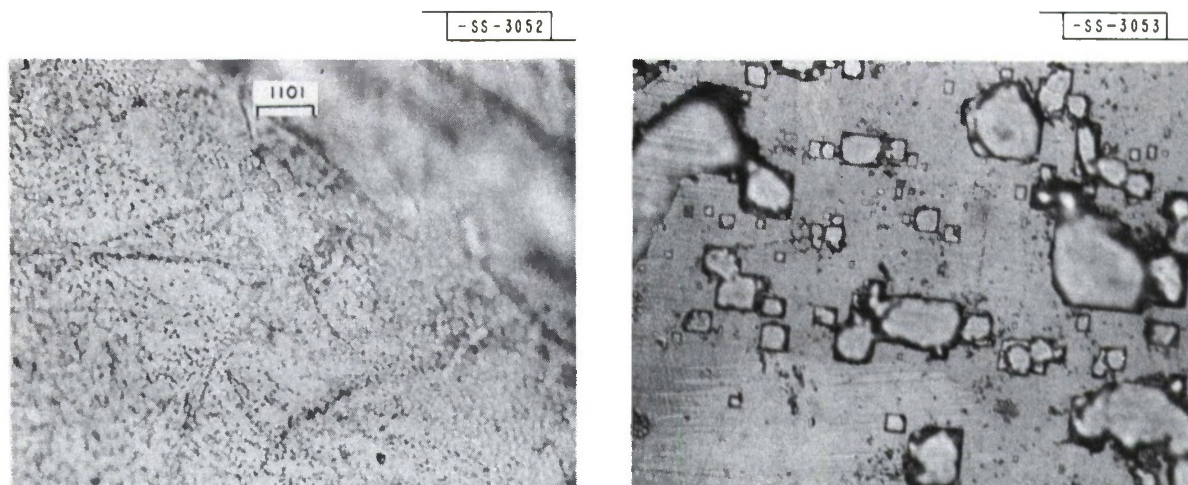

Fig. I-18. Etch pits in PbSe: (a) 1000X, before annealing, etching time 2 minutes; (b) 500X, after annealing, etching time 4 minutes.

The etching solution was a mixture of thiourea and HCl originally developed for use on PbS (Ref. 19) and was applied to PbSe without modification. PbSe of both conductivity types, taken from various sources, had 77°K carrier concentrations ranging from 10^{18} to 5×10^{17} cm^{-3}, and 77°K Hall mobilities between 33,000 and 12,000 cm^2 volt^{-1} sec^{-1}. In all cases, the dislocation densities were found to be on the order of 10^7 cm^{-2}. Figure I-18(a-b) shows photomicrographs of a sample ($n = 2 \times 10^{18}$ cm^{-3}) taken before and after it had been annealed by heating in a closed system at 700°C for 4 hours and cooling to room temperature at a rate of 20°C hr^{-1}. The annealing process apparently decreased the dislocation density by a factor of about ten.

Scanlon[19] observed that minority carrier lifetime in PbS was approximately inversely proportional to dislocation density over the range studied (10^5 to 10^8 cm^{-2}). One would expect a similar dependence in PbSe. If the recombination associated with dislocations is nonradiative, it can be conjectured that the previously reported[20] low efficiency of injection luminescence of PbSe diodes is related to the high dislocation density.

J. F. Butler

I. GROWING HELICAL DENSITY WAVES IN SEMICONDUCTOR PLASMAS

An article with the above title has been submitted to the Physical Review. A summary of the paper follows.

> A theoretical and experimental study is made of growing screw-shaped waves of electron-hole density in a semiconductor bar subjected to sufficiently large parallel electric and magnetic fields. The formulation of a physical model for the growth mechanism and motion of this helical wave leads to several interesting results. It is shown that the wave may exhibit growth in two distinctly different forms. For unequal densities of positive and negative carriers, the growth is spatial, corresponding to unidirectional traveling-wave amplification. For equal or nearly equal carrier densities, the growth may be temporal, leading to instability. The latter case corresponds to the helical instability proposed

by others as an explanation of the anomalous diffusion in a gas discharge with a longitudinal magnetic field, and of the oscillistor effect in semiconductors. It is shown further that growing helical waves may be obtained in a particularly simple physical configuration. All that is required is a uniform semiconductor bar with a low recombination surface, ohmic contacts, and moderate applied electric and magnetic fields.

A detailed and quantitative mathematical description of the growth and propagation characteristics of the waves is presented. Expressions for the threshold fields and frequencies, growth constant, and phase constant for the case of stable spatial growth are derived. These results are further improved in accuracy and extended by numerical computation. The analysis and discussion of the unstable situation is carried out within the framework of a quite general technique for the determination of instability in wavelike systems, and a quantitative stability criterion is developed.

Experimentally, the growing helical waves were excited and observed in bars of 30-ohm-cm germanium at and above room temperature. The growth and phase characteristics of the waves were found to be in excellent agreement with the theoretical predictions. Frequencies of operation ranged from 20 to 400 kcps, with electric and magnetic fields from 25 to 60 volts cm^{-1} and 0 to 11 kgauss, respectively. Stable traveling-wave gain in excess of 35 db cm^{-1} was attained. Above this value, nonlinear effects, including saturation and oscillations in the terminal sample current, similar to the oscillistor effect were observed. At temperatures of 67°C and above, evidence of unstable oscillations appeared, in qualitative agreement with the theoretical predictions. This result, coupled with the observation of current oscillations due to large-signal nonlinearity, further confirm the correctness of previous explanations of the oscillistor effect in terms of a helical instability.

C. E. Hurwitz
A. L. McWhorter

J. CURRENT INSTABILITY IN GaAs

An investigation of an instability in the current through samples of n-type GaAs, first observed by J. B. Gunn,[21] has been started during the past quarter. This instability is observed when the electric field is increased above 2000 volts cm^{-1} and occurs at room temperature with no external magnetic field. The sample, typically a 10^{-2} cm cube of one-ohm-cm n-type GaAs with ohmic contacts on both ends, has a resistance of about ten ohms. The spectrum of the instability has a center frequency of

$$f = v_d/L$$

where v_d is the drift velocity of the electrons in the sample, and L is the length of the sample. The quantity v_d is typically 10^7 cm sec^{-1}, so f is in the 1000-Mcps range. Gunn has reported seeing both sinusoidal and random current variations.

The circuit used in this experiment is shown in Fig. I-19. The current sampling resistor R is usually one-tenth the sample resistance, C is used to provide an electrically short path around the sample, and a pulsed voltage source is used to avoid heating the sample.

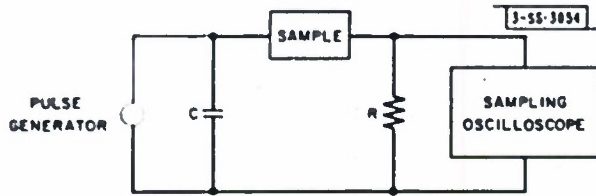

Fig. I-19. Circuit used to observe instability in GaAs.

Both the frequency relation $f = v_d/L$ and the threshold condition $E_{min} \sim 2000$ volts cm^{-1} have been confirmed. Gunn's experiments on the effects of light, temperature, and magnetic field have also been extended to show that light sufficient to change the conductivity of the sample does not affect the instability, that immersing the sample in liquid nitrogen (77°K) does not affect the instability, and that a 10,000-gauss DC magnetic field lowers the amplitude of the instability, but does not change the threshold or the spectrum.

A. G. Foyt

K. INTERFACE-ALLOY EPITAXIAL HETEROJUNCTIONS

An article with the above title has been submitted for publication. The abstract of the paper follows.

Abrupt epitaxial heterojunctions have been produced by melting the lower-melting-point semiconductor at the interface between two different semiconductors. When the temperature is reduced, the melted semiconductor recrystallizes, having alloyed into the higher-melting-point semiconductor. Heterojunctions between GaAs and germanium and between GaAs and GaSb have been produced. Kossel line techniques have been used to prove conclusively that the GaAs-Ge heterojunction is single crystal. Similar but less definitive results for the GaAs-GaSb couple indicate that this heterojunction is also single crystal. In the interface alloying, the wafers rotate and/or tilt with respect to each other as required for single-crystal regrowth, which appears to be the lowest energy method for regrowing. Electron-beam microprobing shows that for the GaAs-Ge couple the transition from GaAs to germanium in the alloyed region is not monotonic, whereas for the GaAs-GaSb couple the transition from arsenic to antimony is abrupt and without structure. As expected from the known electrical activity of germanium in GaAs and gallium and arsenic in germanium, the electrical characteristics of the GaAs-Ge heterojunction cannot be explained by simple heterojunction theory. A possible explanation in terms of tunneling through the barrier at the crystal interface is offered for the forward current of the GaAs-GaSb heterojunctions which varies as $I_0 \exp(AV)$.

R. H. Rediker
S. Stopek
J. H. R. Ward

L. MELT-BACK EPITAXIAL HETEROJUNCTIONS

Heterojunctions between GaAs and GaSb have been produced by completely melting the lower-melting-point semiconductor (GaSb), and cooling it in a temperature gradient such that the interface recrystallizes first. This fabrication technique should be contrasted to that described in the preceding section where only the interface is melted. Although the crystalline nature of a "completely-melted" heterojunction has not, as yet, been investigated, the electrical properties have been studied and are described below.

The GaAs and GaSb samples were square in shape and 0.5 mm thick. The edges were 2 and 1 mm for GaAs and GaSb, respectively, and the resulting junctions were about 1 mm in diameter. The materials were prepared by rough polishing, followed by a 15-second etch in a solution consisting of 10-percent bromine in methyl alcohol. The alloying was performed in a hydrogen atmosphere with heater strips both above and below the GaAs-GaSb couple, as illustrated in Fig. I-20. After the GaSb had been completely melted and observed to "wet" the GaAs, the temperature of the upper strip was slowly reduced to allow the GaSb to regrow from the GaAs surface. The GaSb appeared to regrow smoothly, unless the cooling was done too rapidly. It should be mentioned here that there was evidence of some slight decomposition of the GaAs during the formation of the junction. Units were mounted on tabs with the GaAs side down. Kovar tabs clad with tin were used to make ohmic contacts to n-type GaAs. Ohmic contacts to p-type GaAs were made with tabs clad with 97-percent gold, 3-percent zinc. Alloy contacts using 0.010-inch-diameter 99% Sn-1% Te dots were used to make ohmic contact to n-type GaSb and 0.010-inch-diameter 99% In-1% Zn dots were used for making contact to p-type GaSb.

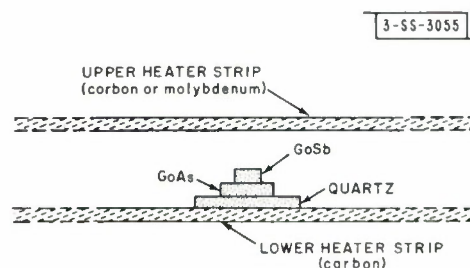

Fig. I-20. Experimental arrangement for alloying.

Units of all combinations of doping GaAs and GaSb were made and studied. The log current density vs voltage data are shown in Fig. I-21 for units at 77°K and in Fig. I-22 for units at 300°K. The reverse bias data depended on surface preparation and are not shown. Units of p-type GaSb on n-type GaAs showed soft reverse breakdowns at about 5 volts. Other units generally had lower breakdown voltages. Forward conduction occurred when p-type GaAs was biased positively or when n-type GaAs was biased negatively. At values of forward current below which series resistance becomes important, the current is a simple exponential function of voltage for all units except p-GaSb on n-GaAs at 77°K, in which case, as shown in Fig. I-21, there is a kink in the forward characteristics. In order to check for contact effects, two contacts were alloyed to each type of material. The characteristics between these contacts were found to be linear; therefore, the results presented above cannot be explained in terms of contact rectification.

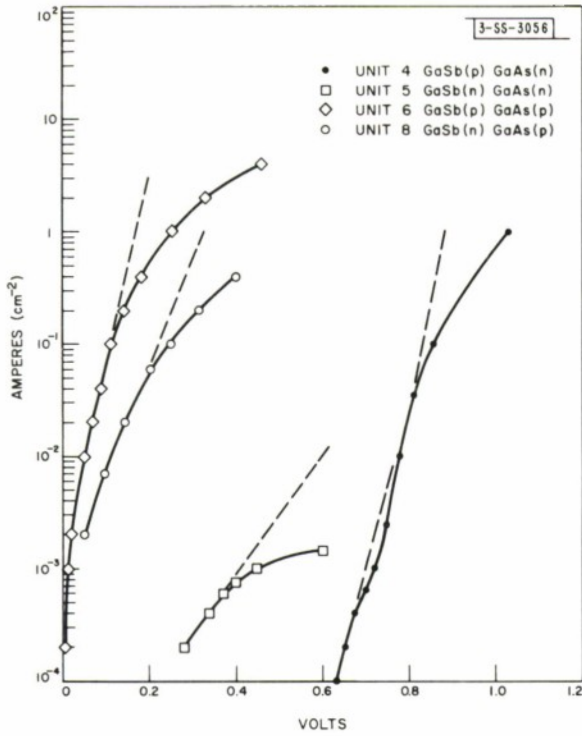

Fig. I-21. Forward current-valtoge choracteristics at 77°K of all four types of GaAs-GaSb hetero-junctions.

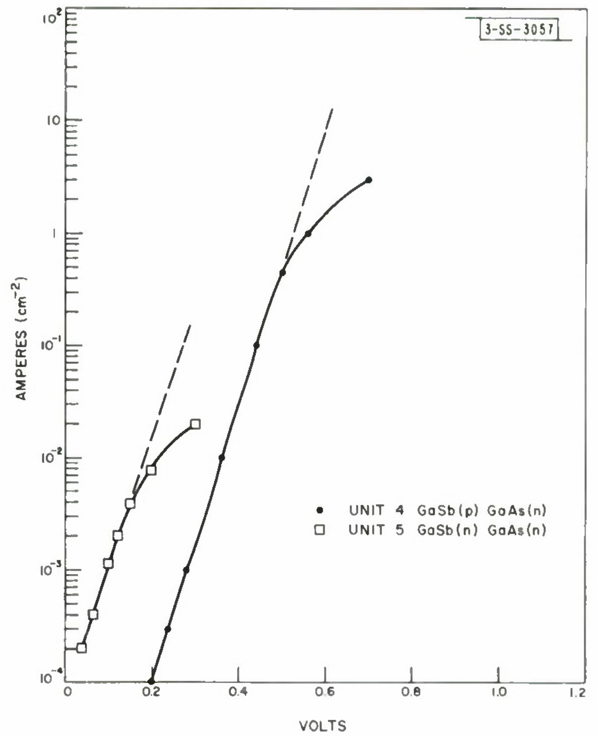

Fig. I-22. Farward current-valtoge characteristics at 300°K of GaAs-GaSb n-p and n-n heterojunctians.

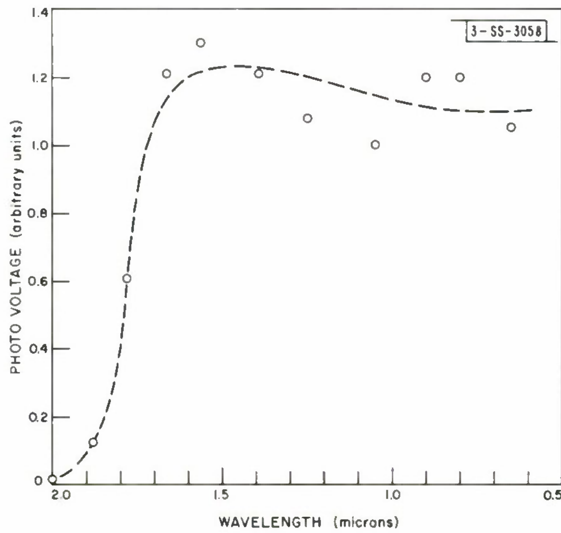

Fig. I-23. Spectral respanse of GaSb-InAs n-p heterojunctian illuminated through GaSb.

All the units showed some sensitivity to light. Some exhibited as much as 0.3 volt open circuit voltage under microscope lamp illumination at 77°K.

Attempts have also been made to form junctions between GaSb and InAs. The structure shown in Fig. I-20 was used with InAs replacing GaAs. The junctions have shown rectification only when made between p-type InAs and lightly doped n-type GaSb. There is visual evidence of decomposition of the InAs and results vary a great deal between units made from similar material.

Efforts have been made to reduce the decomposition by placing the GaSb in direct thermal contact with the upper heater strip and making the process as fast as possible. With data from Boomgaard and Schol,[22] attempts have also been made to establish the appropriate vapor pressure of arsenic to prevent decomposition of the InAs. Arsenic was heated to 400°C on a separate heater strip. When this was done, it was also necessary to heat antimony to 700°C to prevent it from coming out of the melted GaSb, and possibly being replaced by arsenic. When operated under forward bias, diodes made without attempting to reduce the decomposition of InAs emitted infrared radiation at about 1.8 microns, similar to that emitted from GaSb homojunctions. These diodes did not show InAs radiation. At 77°K, most diodes exhibited open-circuit photovoltages as large as 0.6 volt, and short-circuit currents of about 0.5 amp cm^{-2} when illuminated with a microscope lamp at 77°K. The spectral response of one of these diodes, with the junction illuminated from the GaSb side, is shown in Fig. I-23. There was no response for longer wavelength illumination. These results are consistent with those that might be expected if a junction was formed in the GaSb rather than at the GaSb-InAs interface.

When diodes made with the GaSb in direct thermal contact with the upper heater strip, and under vapor pressures of arsenic and antimony, were forward biased, they emitted – in addition to the 1.8-micron radiation, – radiation near 3 microns, very close to that emitted by InAs homodiodes. In general, these units exhibited photovoltages of less than 0.05 volt. It is possible that, using methods to prevent decomposition of the InAs, junctions between other types of InAs and GaSb will show rectification characteristics.

W. Lindley (Summer Staff 1963)

REFERENCES

1. R.J. Phelan, A.R. Calawa, R.H. Rediker, R.J. Keyes, and B. Lax, Appl. Phys. Letters 3, 143 (1963).
2. I. Melngailis and R.H. Rediker, Appl. Phys. Letters 2, 202 (1963).
3. T.S. Moss, S.D. Smith, and T.D.F. Hawkins, Proc. Phys. Soc. (London) B70, 776 (1957).
4. P.P. Sorokin and M.J. Stevenson, Advances in Quantum Electronics, J.R. Singer, Ed. (Columbia University Press, New York, 1961), pp. 65-76.
5. V.J. Silvestri and V.J. Lyons, J. Electrochem. Soc. 109, 963 (1962).
6. R.R. Moest and B.R. Shupp, J. Electrochem. Soc. 109, 1061 (1962).
7. San-Mei Ku, J. Electrochem. Soc. 110, 991 (1963).
8. F.A. Pizzarello, J. Electrochem. Soc. 110, 1059 (1963).
9. N. Holonyak, Jr., D.C. Jillson, and S.F. Bevacqua, Metallurgy of Semiconductor Materials, J.B. Schroeder, Ed. (Interscience, New York, 1961).
10. Solid State Research Report, Lincoln Laboratory, M.I.T. (1963:1), p. 1, DDC 405517.
11. J.R. Dixon and J.M. Ellis, Phys. Rev. 123, 1560 (1961).
12. J.C. Marinace, J. Electrochem. Soc. 110, 1153 (1963).
13. T.M. Quist, private communication.
14. S.J. Silverman, J. Electrochem. Soc. 109, 166 (1962).
15. Solid State Research Report, Lincoln Laboratory, M.I.T. (1963:3), pp. 1-3, DDC 427340.
16. Solid State Research Report, Lincoln Laboratory, M.I.T. (1963:2), p. 5, DDC 417686.
17. R.F. Brebrick and E. Gubner, J. Chem. Phys. 36, 170 (1962); ibid., 1283.
18. R.F. Brebrick and R.S. Allgaier, J. Chem. Phys. 32, 1826 (1960).
19. W.W. Scanlon, Phys. Rev. 106, 718 (1957).
20. Ref. 16.
21. J.B. Gunn, Solid State Communications 1, 88 (1963).
22. J. van den Boomgaard and K. Schol, Philips Research Report 12, 127 (1957).

II. LASER RESEARCH

A. RAMAN MASER

The angular distribution data of stimulated Raman emission from nitrobenzene[1] have been used to calculate the dispersion characteristics of nitrobenzene. Using known values of index of refraction[2] at the laser frequency L and anti-Stokes line AS_1, and the measured peak angles of AS_1, S_2, and S_3, values for the index of refraction at S_1, S_2, and S_3 have been calculated (Fig. II-1). This curve is the same as a previous one,[3] except that the point S_3 has been moved to correct a numerical error.

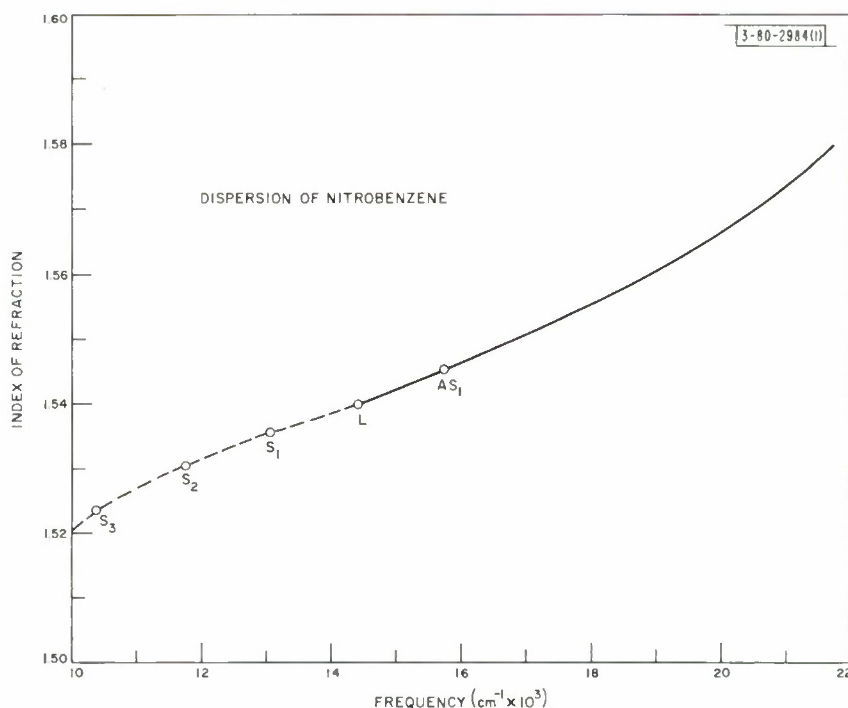

Fig. II-1. Dispersion characteristic of nitrobenzene. Solid portion of curve is measured index of refraction; dashed portion is drawn through points calculated from angular peaks of AS_1, S_2, and S_3.

In order to further substantiate the two-step Raman scattering model, experiments are now in progress to obtain stimulated S_1 emission in an optical cavity structure at an angle with the forward direction. An even more crucial test is the feeding in of S_1 radiation at the phase-matching angle and observation of an enhancement of the associated AS_1 radiation.

S. Kern P. E. Tannenwald
F. H. Perry H. J. Zeiger

B. THEORY OF STIMULATED RAMAN EMISSION

The stimulated Raman process has been studied theoretically. Equations coupling the radiation field and molecular oscillations at frequency ω_v are derived from the density operator equations of motion for the material system. These molecular displacements introduce nonlinear terms into Maxwell's equation. The cubic term is found to be responsible for the stimulated Raman effect. The resulting Maxwell equation is of a similar form to that obtained by Armstrong, et al.,[4] and specialized to the Raman case by Garmire, et al.,[5] Terhune,[6] and Hellwarth.[7] In the dominant Raman process, two of the amplitude factors in the cubic term pertain to the incident radiation. If we assume that the incident intensity at frequency ω_o is constant, the cubic term reduces to an effective linear term which couples the Stokes radiation at frequency $\omega_o - \omega_v$, with the anti-Stokes radiation at frequency $\omega_o + \omega_v$. In the case of plane waves, such as treated by Garmire, et al.,[5] the coupling between the two waves is significant if the following matching condition is fulfilled[5,8]

$$\vec{k}_{\omega_o+\omega_v} + \vec{k}_{\omega_o-\omega_v} = 2\vec{k}_{\omega_o} \quad . \tag{1}$$

If the above phase-matching condition is obeyed, the growth of the Stokes radiation is severely modified from that which would be obtained in the absence of interaction. In particular, for the plane wave model, the two waves should obtain nearly the same intensities in the phase-matched directions.

Methods of solution of the coupled equations in three dimensions have been investigated in some detail. These methods are based on the probable nature of the sources of the Stokes and anti-Stokes radiation. The noise sources responsible for the generation of Stokes and anti-Stokes waves are the zero point or thermal vibrations of the material oscillators interacting with the incident radiation, or Stokes radiation scattered from the forward direction. We restrict the present calculation to the first case.

The Stokes noise radiation is by far the stronger one since, at the molecular vibration, the zero-point fluctuations predominate. Because the Raman oscillators are, to a high degree of approximation, independent, one can assume that the noise sources form an incoherent superposition of point sources that produce the Stokes radiation. If one disregards, at first, the interaction of the Stokes and anti-Stokes radiations, each point noise source at the Stokes frequency acts as a radiating dipole, thus producing a growing spherical wave. The coupling between the Stokes and anti-Stokes radiations causes the spherically-growing Stokes wave to introduce a source term in the anti-Stokes equation. The anti-Stokes radiation produced by this source term is found to be strongly peaked in the direction given by solving Eq. (1) for the angle between the anti-Stokes and the incident radiations. It is then found that this anti-Stokes radiation does not markedly affect the Stokes wave because, for spherical waves, the phase-matching condition (1) is fulfilled only in a narrow angular region. This is in contrast to the plane wave case where the plane waves may interact over the entire (Raman) active region. The angular width of the anti-Stokes peak is obtained in terms of the growth and coupling constants for Stokes and anti-Stokes radiations.

Since the above model treats the anti-Stokes generation as a small perturbation on the Stokes radiation, the intensity of the Stokes radiation is therefore solely a function of its path length in

the active region. The average path length has been calculated as a function of the angle with respect to the direction of the incident radiation. The results are in qualitative agreement with the experimental evidence,[8] provided the beams of incident radiation are very narrow compared with the distance traveled through the active medium.

P. L. Kelley
H. J. Zeiger
H. Haus (Department of
Electrical Engineering, M.I.T.)

C. ENERGY LEVELS OF d^1 ELECTRONS IN CALCIUM FLUORIDE

Previous papers[9] have shown that transition ions such as scandium, yttrium, and lanthanum behave as deep electron traps in CaF_2. This section reports new data on optical absorption and electron spin resonance (EPR) of Sc^{+2} ($3d^1$), Y^{+2} ($4d^1$), and La^{+2} ($5d^1$) in CaF_2. The data can be explained only by a strong, dynamical, Jahn-Teller (J-T) distortion[10] of the ground state of these d^1 electron ions.

Several single crystals of CaF_2 doped with either ScF_3, YF_3, or LaF_3 were grown and then exposed to 5×10^6 rad of 2.5-Mev electrons from a Van de Graff generator.[11] The trapping of d^1 electrons occurs as follows. Trivalent transition ions substitute for Ca^{+2} at cation sites. The excess positive charge is compensated for by an interstitial F^{-1} ion. Because of the rapid diffusion of anions in CaF_2, the transition ion and its compensator will be highly associated. When this material is exposed to ionizing radiation, the transition ion traps an electron in a d-state; a hole is, in general, trapped in a p-level of the F^0 compensator. For highly associated pairs, there is sufficient wave function overlap for recombination to occur. In particular, the thermoluminescent spectra of CaF_2: Sc, Y, La can be explained[12] on the basis of radiative recombination from electron-hole pairs situated on the first five nearest-neighbor sites. Separated pairs are metastable and represent ~5 percent of the initial concentration. Subsequent reduction in this concentration is due to hole hopping from the F^0 site toward the divalent transition ion.

The pertinent EPR data of Sc^{+2}, Y^{+2}, and La^{+2} are shown in Table II-1(a). These results were obtained by using a 23.4-kMcps spectrometer at temperatures of 4.2° and 20°K. At temperatures above 20°K, the resonance of these ions is isotropic and can be fitted to a spin Hamiltonian with an isotropic g-factor (g_{iso}). At 4.2°K, however, these ions show an axial spectrum which corresponds to a tetragonal distortion along one of the cube edges. The axial spin Hamiltonian can be fitted by $g_{||} = 2.0$ and $g_{\perp} = 2 - \lambda/\Delta$, where λ is the spin-orbit interaction parameter.

Following Van Vleck,[13] Öpik and Pryce,[14] and Hayes and Twidell,[15] we assume that there are two normal modes of vibration, $Q_2 = \rho \sin\Theta$ and $Q_3 = \rho \cos\Theta$, of a cube which will couple with the e_g doublet. The doublet will be split and the energy of the lowest orbital singlet is given by

$$E = -A\rho + \frac{1}{2} M\omega^2\rho^2 \pm A_3\rho^3 \cos 3\Theta$$

where the first term represents the J-T electronic energy, the second term is the elastic energy in the absence of a J-T effect and the last term gives the angular dependence of the energy. Both

TABLE II-1

OPTICAL AND PARAMAGNETIC PROPERTIES OF Sc, Y, AND La IN CaF_2 SINGLE CRYSTALS

(a) Paramagnetic Properties				(b) Optical Transitions (mμ)		
Ion	g_{iso}	$g_{\parallel}$	$g_{\perp}$	$e_g \rightarrow t_{2g}$	$\Delta(cm^{-1})$	$d_{z^2} \rightarrow d_{x^2-y^2}$
Sc (III)	1.991	1.99	1.985	311 374 418	27,600	538 (18,590 cm^{-1})
Y (III)	1.971	1.99	1.958	230 336 402	32,700	582 (17,180 cm^{-1})
La (III)	1.936	2.00	1.905	271 351 421	29,700	678 (14,750 cm^{-1})

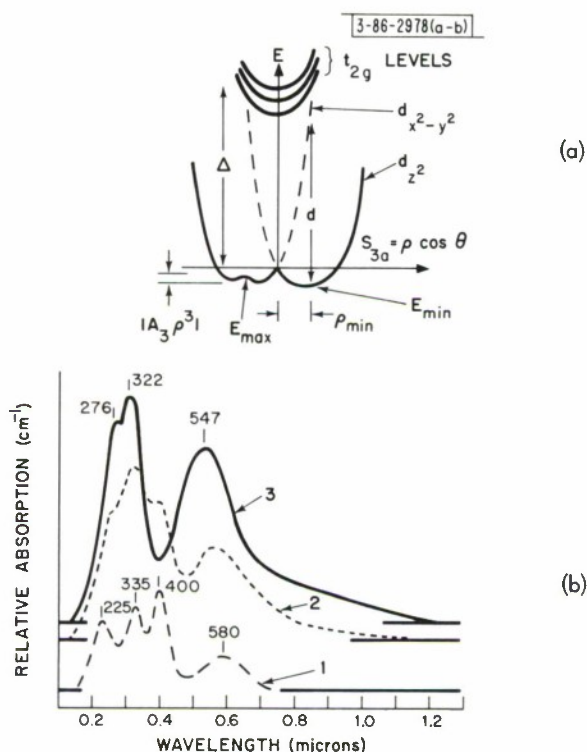

Fig. II-2. (a) Energy level diagram for a d^1 electron in CaF_2. (b) Relative optical absorption (cm^{-1}) of $CaF_2(Y^{+2})$ as a function of wavelength. Curve 1 – room temperature electron irradiation and measurements, curve 2 – irradiated at 77°K and measured at 260°K, curve 3 – irradiated and measured at 77°K.

E and the g-factor will depend on the sign of A_3 as well as on the expectation value of Θ.

The EPR spectra allow us to construct the energy level diagram shown in Fig. II-2(a). The e_g doublet splits, leaving a d_{z^2} ground state. The ground state has energy minima, $E_{min} \approx -A^2/2M\omega^2$, at $\Theta = \pi$, $5\pi/3$, and $\pi/3$. Three potential barriers, located between the minima, are given by $E_{max} \approx -E_{min} + A_3\rho^3$. Both E_{min} and E_{max} are located on a circle radius $\rho_{min} = A/M\omega^2$. The cubic field will raise the t_{2g} levels an energy of $\Delta = 30{,}000\ cm^{-1}$. In addition, these levels will be split by the static J-T tetragonal field as well as a J-T effect in the excited states. Figure II-2(a) shows that the $d_{z^2} \rightarrow d_{(x^2-y^2)}$ vertical, optical transition, represented by d, will occur close to the t_{2g} levels. We therefore expect four broad optical absorptions at an energy of $\sim 30{,}000\ cm^{-1}$.

Curve 1 of Fig. II-2(b) plots the optical absorption at 20°C due to Y^{+2}. Spectra for Sc^{+2} and La^{+2} are similar and are given in Table II-1(b). The spectra of Y^{+2} change with temperature as follows. At 77°K, the t_{2g} levels shift to higher energies by $125\ cm^{-1}$ and at ~10°K move an additional $175\ cm^{-1}$. The d-transition, however, shifts toward lower energy as the temperature is decreased. At 77°K, the shift is $350\ cm^{-1}$ and at ~10°K the total shift is $725\ cm^{-1}$. To examine this situation, crystals of CaF_2:Y were irradiated with electrons at 77°K and maintained at this temperature for absorption measurements. The spectrum at 77°K is shown by curve 3 and curve 2 shows how the absorptions change as the sample temperature is raised to ~260°K. These spectra are interpreted as follows. At 77°K, a weak band is observed at 828 mμ which disappears into a broad tail of the d-transition at ~100°K. The origin of the band appears to be structural and is probably a hole or other point defect trapped near the Y^{+2} ion so that the d-transition occurs at a low energy. Most of the d-transition at 77°K is at 547 mμ. Note also at 77°K that the splitting of the t_{2g} levels has been reduced.

J. R. O'Connor
J. H. Chen (Boston College)

D. INTENSE SOURCES FOR OPTICALLY EXCITED GaAs CRYSTALS

Previously, the external quantum efficiency of optically excited GaAs crystals was reported to be within an order of magnitude of values obtained from diode masers operated below threshold.[16] Further investigation and recent reports[17-20] have shown that p-type crystals with approximately $1 \times 10^{19}\ cm^{-3}$ zinc or cadmium impurity concentrations and n-type material with approximately $3 \times 10^{17}\ cm^{-3}$ tellurium or silicon impurities exhibit spontaneous emission characteristics similar to diode maser subthreshold spectra. As a result, an effort has been made to observe stimulated emission from such crystals by the use of high-intensity optical pumps. Several systems of this nature have been designed and constructed with the ultimate source parameters defined by thermal, detector, and inversion considerations. A continuously variable pump with a maximum power density of $5000\ watts\ cm^{-2}$, a pulse length of $\leqslant 10\ \mu sec$, a spectral distribution such that $3000 \leqslant \lambda \leqslant 8000\ \text{Å}$, a 13-pps repetition rate, and 30-percent efficient optical coupling were taken as the initial design parameters.

The first source to show promise of fulfilling the given requirements was the Edgerton, Germeshausen & Grier FX-51 xenon flashlamp which has an arc length of 8 cm and an inside bore diameter of 0.7 cm. Successful operation of this lamp up to its maximum voltage rating

of 3000 volts DC was characterized by a maximum power density of 250 watts cm^{-2} (through a Corning CS4-97 filter), lasting 100 μsec at a repetition rate of 1.6 pps. The optical coupling consisted of a fast lens and mirror system which effectively collected 7 percent of the total lamp power. This system without the filter pumped a $CaWO_4:Nd^{3+}$ maser at 1.6 pps, 2000 volts DC, and 100 μfd.

The output spectrum determined by the CS4-97 filter was studied with a Jarrell-Ash f/6.3 spectrometer and showed a predominantly blue radiance having a 2700-Å bandwidth. The same type of tube with mercury added was approximately 10 percent less efficient than the standard lamp.

An experimental XFX-51 source with a 5000-volt DC maximum rating has recently been purchased and preliminary studies have yielded operation at 1.6 pps, 4000 volts DC, and 1 μfd, with a 25-μsec output pulse duration. Also, the filtered bandwidth has been doubled by the use of a KG-3 Schott heat-glass filter, and the optical coupling increased 25 percent by utilizing an American Optical image conduit. This system should yield 750 watts cm^{-2}. In addition, a 1-μsec, 13-pps, 5000-watts cm^{-2} pump is anticipated when a 10,000-volt DC PEK-XE-10 xenon lamp system is completed.

The second source, a ruby laser, was chosen for its immediate availability, high intensity, and short duration pulse. Such a device has been previously used to excite semiconductor crystals having a band edge greater than 7000 Å.[21] By using a directly exposed 7102, S-1 response photomultiplier, it was possible to calibrate a 5-mm square rod in a normal-mode external-mirror configuration such that a repeatable power density as high as 6×10^4 watts cm^{-2} and individual spike durations of approximately 0.5 μsec could be obtained.

Although both sources have produced useful data, the results regarding stimulated emission have been inconclusive, and a rigorous experimental program for obtaining more definitive information has been undertaken.

J. J. Schlickman

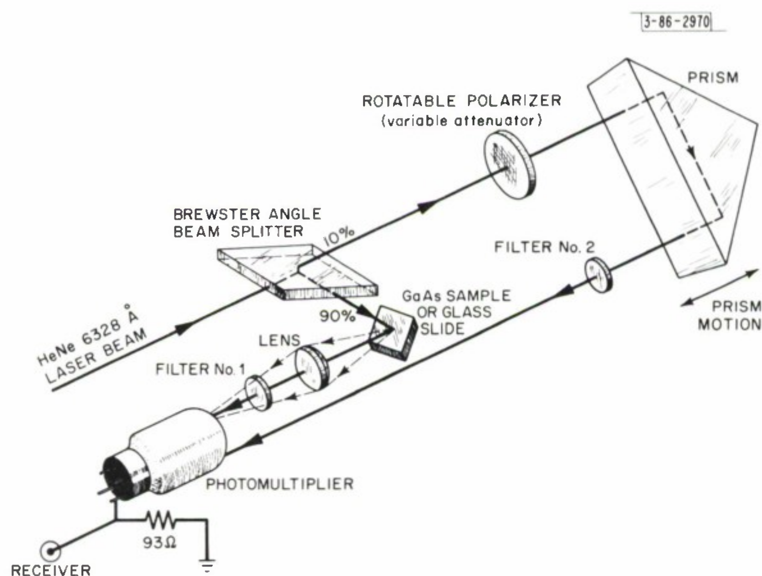

Fig. II-3. Phase shift interferometer.

E. INTERFEROMETRIC PHASE-SHIFT TECHNIQUE FOR MEASURING SHORT FLUORESCENT LIFETIMES

As is well known, the beam from a gaseous laser, when projected on the cathode of a photomultiplier, will produce a signal at the difference frequency between axial modes of the laser cavity.[22,23] Excitation of a fluorescent material by the same gaseous laser beam produces a fluorescence which is also amplitude-modulated at just this difference frequency. Using a gaseous laser as a source for a 2-beam interferometer, and a photomultiplier as a detector, one can obtain a null in the difference signal when a beam travels an additional distance equal to just half a wavelength of the difference frequency. Hence, one can measure by a sensitive null technique, a phase shift in the modal difference frequency produced in a fluorescent material by virtue of the fact that it emits with some characteristic time τ.

The experimental apparatus consists of a 2-beam interferometer, gaseous laser source, and photomultiplier detector schematically shown in Fig. II-3. The helium-neon laser is operated at 6328 Å with a mirror spacing which gives stable optical modes 155 Mcps apart. The receiver is tuned to accept the 155-Mcps signal which is detected by the audio beat between it and a beat-frequency oscillator. The audio signal is nulled first with a glass slide reflector in place of the sample, by moving the prism along an optical bench. The filters are such that both 6328-Å beams reach the detector but with suitable attenuation. The polarizer is a convenient means of attenuating one beam so the amplitudes of both beams are identical; otherwise, the null will not be complete. The glass slide is then replaced by a fluorescent sample with the appropriate filter to block the 6328-Å radiation and allow the fluorescent radiation to reach the detector. The null position of the prism will now have been altered by the phase delay associated with the fluorescent lifetime.

By means of this technique, we have measured the lifetime at room temperature for single-crystal Merck GaAs, n-doped with tellurium, and find that $\tau = 3.0 \times 10^{-9}$ sec. This may be compared with an experimental value[24] of 6×10^{-9} sec determined from minority carrier storage measurements in diodes and a theoretical calculation[25] that indicates a lower limit of $\tau = 2.5 \times 10^{-10}$ sec. Fluorescent spectra of this sample excited by the 6328-Å laser show that the fluorescent radiation is contained totally in a single band 240 Å wide, peaked at 8690 Å.

Further measurements on a p-n junction doped with zinc and tellurium, respectively, give $\tau = 6.6 \times 10^{-10}$ sec for the p-doped face and $\tau = 9.4 \times 10^{-10}$ sec for the n-doped face. On cooling to liquid nitrogen temperature, the lifetimes are shortened by about 1×10^{-10} sec. We have been unable to note any difference in lifetime between a sample with a carefully lapped surface and the same sample with an etched surface.

Further work is planned with a monochromator in the fluorescent beam. It should be noted that this technique is adaptable to the measurement of the relative delay across the face of a photomultiplier detector.

P. R. Longaker
R. J. Carbone

F. MULTILAYER DIELECTRIC FILMS

The vacuum evaporation unit for producing multilayer dielectric films has been used for mirror preparation and reflective coatings on such devices as GaAs lasers. Multilayers having

their spectral reflecting bands centered around 6000, 7000, 8500 Å, and 1.4 microns have been produced successfully. Figure II-4 shows a typical spectral transmittance curve, in this case, for a mirror prepared to reflect at both 5700 and 6300 Å.

M. D. Zimmerman

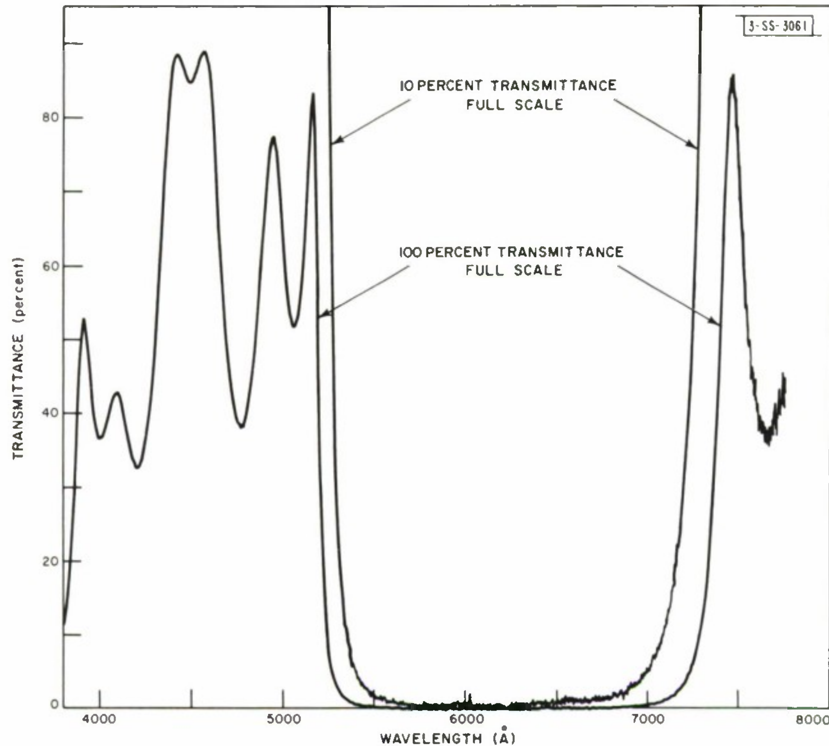

Fig. II-4. Transmittance of ZnS-MgF_2 multilayer dielectric mirror.

G. FAR-FIELD PHOTOGRAPHS OF IMPROVED RUBY

Successful operation of such systems as the parametric oscillator require high mode purity in the ruby beam. Far-field patterns of a 1-inch-long ruby[26] of excellent quality were taken with a lens of 2-meter focal length. The photographs, taken with progressively decreasing exposures, are shown in Fig. II-5(a-d). For comparison, the far-field pattern of a ruby of ordinary quality is shown in Fig. II-6.

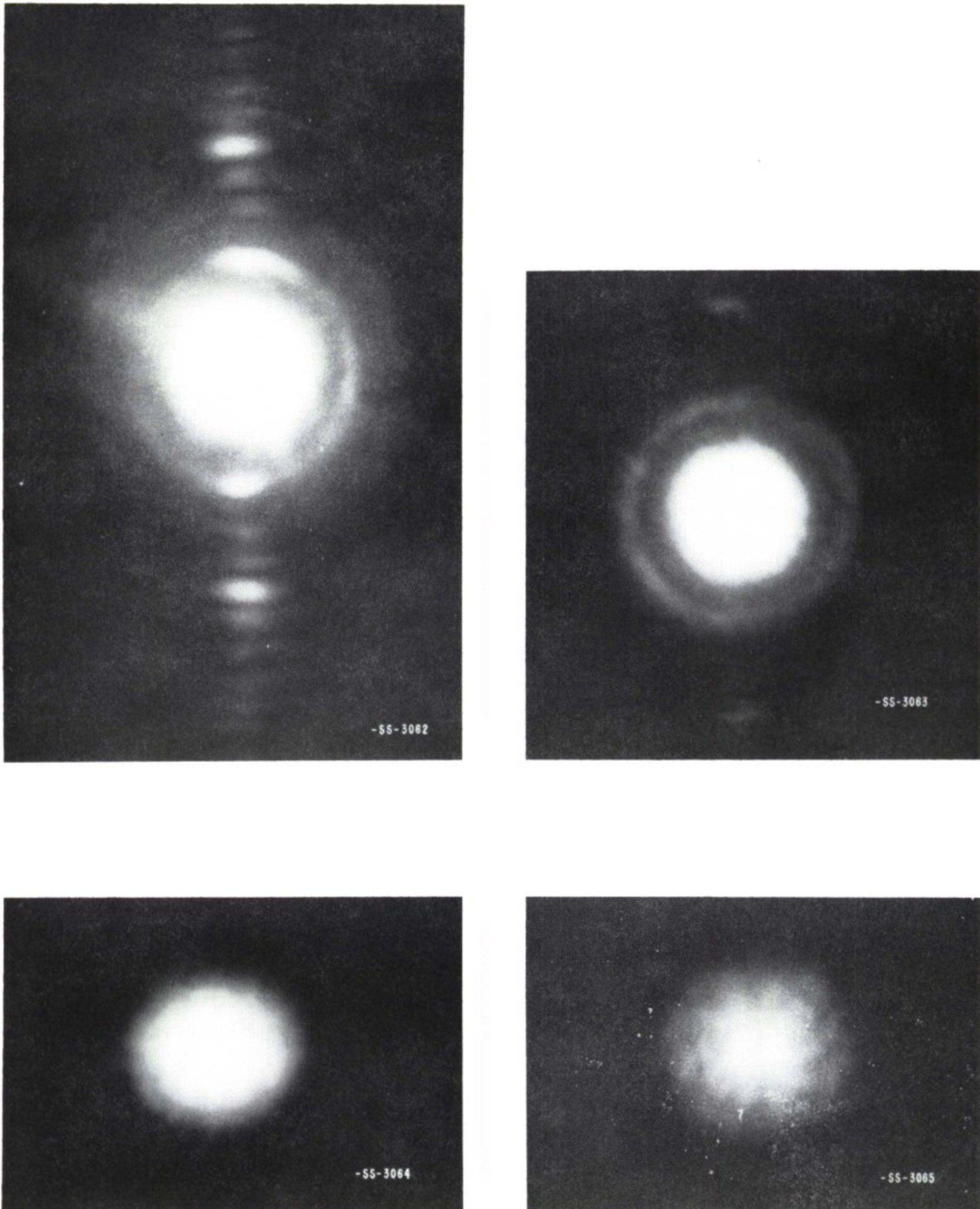

Fig. II-5. Far-field pattern of an improved ruby, exposures decrease from (a) to (d).

Fig. II-6. Far-field pattern of an ordinary ruby.

In the photograph of the good ruby, the off-axis modes are quite distinguishable from the on-axis modes of the Fabry-Perot etalon resonator of the laser. In Fig. II-5(a), several off-axis rings are seen in addition to the overexposed on-axis modes in the center. In (b) only one off-axis mode, the first one, which lies at $\Theta = \sqrt{\lambda}/d$ is seen. In (c), only the on-axis modes appear, and in (d) the central diffraction spot of the on-axis modes is evident. The angular width of this spot is $\Theta = \lambda/d$, the diffraction limit. In the photograph of the ordinary ruby (Fig. II-6), the on- and off-axis modes are smeared together and indistinguishable.

Jane H. Dennis

REFERENCES

1. Solid State Research Report, Lincoln Laboratory, M.I.T. (1963:3), pp. 13-15, DDC 427340.
2. K. Feussner, Z. Physik 45, 689 (1927).
3. H.J. Zeiger, P.E. Tannenwald, S. Kern, and R. Herendeen, Phys. Rev. Letters 11, 419 (1963).
4. J.A. Armstrong, N. Bloembergen, J. Ducuing, and P.S. Pershan, Phys. Rev. 127, 1918 (1962).
5. E. Garmire, F. Pandarese, and C.H. Townes, Phys. Rev. Letters 11, 15 (1963).
6. R.W. Terhune, Solid State Design 4, 38 (1963).
7. R.W. Hellwarth, Current Science, India (to be published).
8. H.J. Zeiger, P.E. Tannenwald, S. Kern, and R. Herendeen, Phys. Rev. Letters 11, 419 (1963).
9. J.R. O'Connor and J.H. Chen, Bull. Am. Phys. Soc. II, 8, 231 (1963); Phys. Rev. 130, 1790 (1963); J. Phys. Chem. Solids 24 11, 1382 (1963); J.H. Chen and J.R. O'Connor, Bull. Am. Phys. Soc. II, 8, 231 (1963).
10. H.A. Jahn and E. Teller, Proc. Roy. Soc. (London) A161, 220 (1937).
11. The authors gratefully acknowledge the help of Dr. K.A. Wright at M.I.T.
12. J.R. O'Connor (to be published).
13. J.H. Van Vleck, J. Chem. Phys. 7, 72 (1939).
14. V. Öpik and M.H.L. Pryce, Proc. Roy. Soc. (London) A238, 425 (1957).
15. W. Hayes and J.W. Twidell, Proc. Phys. Soc. (London) 82, 330 (1963).
16. Solid State Research Report, Lincoln Laboratory, M.I.T. (1963:2), p. 49, DDC 417686.
17. M.I. Nathan and G. Burns, Phys. Rev. 129, 125 (1963).
18. M.I. Nathan and G. Burns, Appl. Phys. Letters 1, 89 (1962).
19. D.K. Wilson, Appl. Phys. Letters 3, 127 (1963).
20. D.E. Hill, Phys. Rev. Letters (to be published).
21. N.G. Basov, L.M. Lisitsyn, and B.D. Osipov, Doklady 8, 290 (1963) [English translation].
22. D.R. Herriott, "Optical Properties of the Cavity and Output Beam of a Continuous Gas Maser," Advances in Quantum Electronics (Columbia University Press, New York, 1961), pp. 44-49.
23. A.T. Forrester, R.A. Gudmundsen, and P.O. Johnson, Phys. Rev. 99, 1691 (1955).
24. J. Halpern and R.H. Rediker, Proc. IRE 48, No. 10 (1960).
25. H.J. Zeiger, J. Appl. Phys. (to be published).
26. Obtained from the Linde Company by D.F. Edwards.

III. MATERIALS RESEARCH

A. VAPOR GROWTH OF CRYSTALS BY FORCED CONVECTION

A number of different methods have been used for vapor growth of crystals. Most theoretical attention has been focused on growth from a one-component vapor, since this process can be analyzed in terms of two independent variables: the temperature of the growing crystal and the degree of supersaturation. The practical importance of this method is limited, however, since only materials which have relatively high vapor pressures below their melting points can be grown in single-crystal form at satisfactory rates.

Crystals of materials with low vapor pressures can be grown from the vapor, if suitable carrier gases are available. One method of this kind, in which the carrier gas transports material from the source to the growing crystal by natural convection, is shown schematically in Fig. III-1(a). Since the concentration of the transported species available for deposition from the gas phase is less by a factor of 10^4 to 10^6 than the concentration of the crystal, the volume of carrier gas which must be moved is 10^4 to 10^6 cm^3 per cubic centimeter of grown crystal. Under the usual experimental conditions, the velocity produced by natural convection is of the order of 10 cm sec^{-1}. Therefore, the linear growth rates achieved by this method are inconveniently low, typically in the range 10^{-3} to 10^{-1} cm hr^{-1}.

The rate of crystal growth can be greatly increased by forced convection of the carrier gas, since gas velocities up to 10^5 cm sec^{-1} can easily be attained in this manner. The use of forced convection is also advantageous because the degree of supersaturation can be better controlled and because the formation of massive crystals rather than dendrites is favored, since crystal growth is significantly influenced by aerodynamic as well as by crystallographic forces.

An apparatus for studying forced convection is shown schematically in Fig. III-1(b). A stream of carrier gas saturated with vapor at temperature T_2 is directed by a nozzle to a cooled seed,

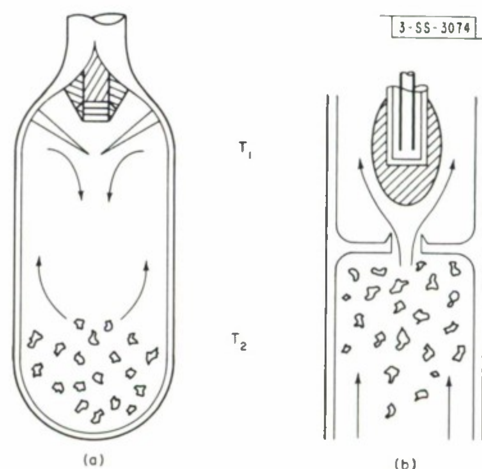

Fig. III-1. Vapor growth of crystals by: (a) natural convection and (b) forced convection. The directions of gas flow are indicated by arrows.

where crystal growth occurs at temperature T_1. The rate G_o in grams per hour at which vapor leaves the nozzle is given by

$$G_o = \frac{p_2}{1 - p_2} \frac{Q_e M}{24.02}$$

where p_2 is the vapor pressure in atmospheres of the feed stock at T_2, Q_c is the flow rate of carrier gas in liters (NTP) per hour, and M is the molecular weight of the vapor. Only a portion of the vapor leaving the nozzle is available for deposition at T_1, since the carrier gas must remain saturated with vapor at that temperature. The maximum possible rate of deposition G_{max} is given by

$$G_{max} = G_o \left[1 - \frac{p_1(1 - p_2)}{p_2(1 - p_1)}\right]$$

where p_1 is the vapor pressure in atmospheres of the crystal at T_1. Two different growth efficiencies are of interest. The projected efficiency is defined as the ratio of the observed growth rate in the projected area of the nozzle to the maximum possible rate ($E_p = G_p/G_{max}$), and the total efficiency is the ratio of the total growth rate to the maximum possible rate ($E_t = G_t/G_{max}$).

In order to study the forced convection method experimentally, growth of iodine crystals by this method is being investigated. Iodine was chosen because rapid crystal growth can take place at convenient temperatures and because growth from pure iodine vapor has already been extensively studied. The apparatus is shown in Fig. III-2. It is immersed in a water thermostat

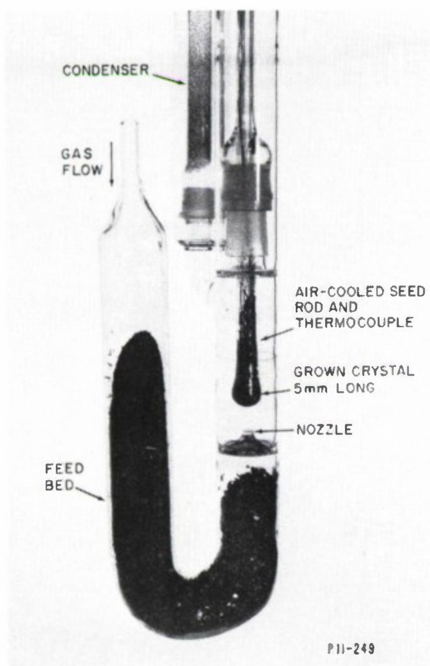

Fig. III-2. Apparatus for forced convection growth of iodine crystals.

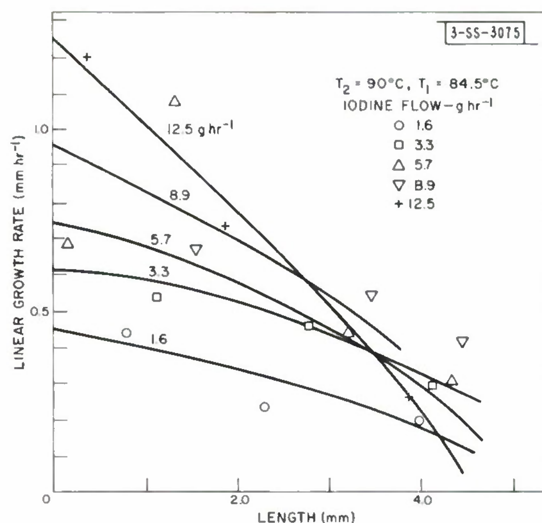

Fig. III-3. Linear growth rate vs length for iodine crystals grown at various flow rates.

typically maintained at 90°C. Helium gas passes through a preheater coil (not shown), a feed bed of granular iodine 8 inches long, and a glass nozzle. The saturated gas then strikes an air-cooled glass finger containing a thermocouple and finally passes through a condenser, where the iodine not deposited on the cold finger is condensed. Figure III-2 shows a boule, consisting of several large grains, which was grown on the cold finger during one of the runs. It can be seen that the shape of the boule was determined primarily by the gas-flow pattern.

Quantitative results obtained in one preliminary run are shown in Fig. III-3. The linear growth rate on the portion of the cold finger opposite the nozzle, measured with a cathetometer, is plotted against the total length of grown crystal for various values of G_o. There is considerable scatter in the data due to fluctuations in the cold finger temperature which resulted from using an unsatisfactory air regulator. Nevertheless, it is clear that the growth velocity decreased as the length of the crystal increased, probably because the temperature at the growth interface increased, even though the temperature measured by the thermocouple inside the cold finger was kept approximately constant. The difference between the interface and thermocouple temperatures should have been greatest at the highest gas flow rates. This probably accounts for the fact that for the longest crystals the growth velocity decreased with increasing G_o, while for sufficiently short crystals the velocity increased with G_o as expected. The growth rates are an order of magnitude greater than those usually observed for vapor growth of massive crystals, although gas velocities of only 10 to 100 cm sec^{-1} were used.

During the run of Fig. III-3, 65.6 grams of iodine were vaporized from the feed bed at T_2 = 90°C (p_2 = 27.5 mm Hg). Of this amount, 15.5 grams were available for deposition at T_1 = 84.5°C (p_1 = 21 mm Hg). The mass condensed on the seed was 5.9 grams, giving a value of 0.38 for the average total efficiency for all the flow rates listed in Fig. III-3. This is actually a minimum value for E_t, since the average temperature at the interface was probably greater than 84.5°C. For a flow rate of 1.6 g hr^{-1} of iodine, the initial growth rate was 0.45 mm hr^{-1}, corresponding to a projected efficiency E_p of 0.09.

It is interesting to compare the measured mass transfer efficiencies with the heat transfer efficiencies measured in forced convection heat transfer from flames. For slow flames such as those produced by a bunsen burner, as much as 10 percent of the available heat can be transferred to a probe in the projected area of the flame, while essentially 100 percent of the available heat can be transferred to a sufficiently large probe.

T. B. Reed
W. J. LaFleur

B. THERMOELECTRIC MEASUREMENTS ON HIGH-RESISTIVITY SOLIDS

A system has been constructed for making thermoelectric measurements at temperatures between −50° and 900°C on solids with resistances at least as high as 20 megohms. Rigorous shielding of all parts of the system, including even the dewar containing the thermocouple reference junctions, was found to be necessary to prevent spurious readings due to pickup. Figure III-4 is an exploded view of the sample holder assembly. The silver blocks shown are used to stabilize the temperatures at the ends of the sample and to minimize temperature gradients along the thermocouples, which are insulated by quartz spaghetti and brought out through holes in the blocks. The sample assembly is clamped together by means of spring-loaded stainless

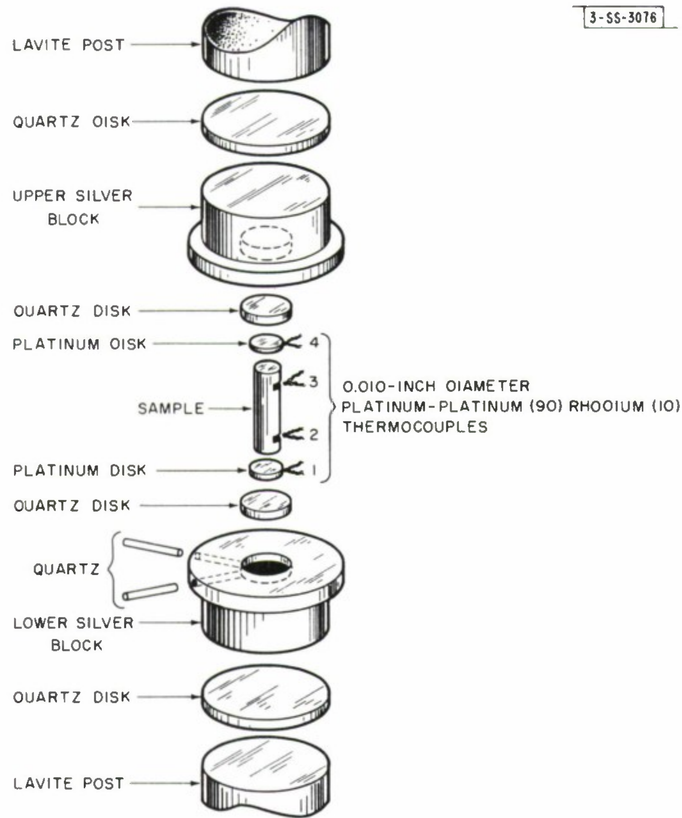

Fig. III-4. Exploded view of sample assembly used for thermoelectric measurements on high-resistivity solids.

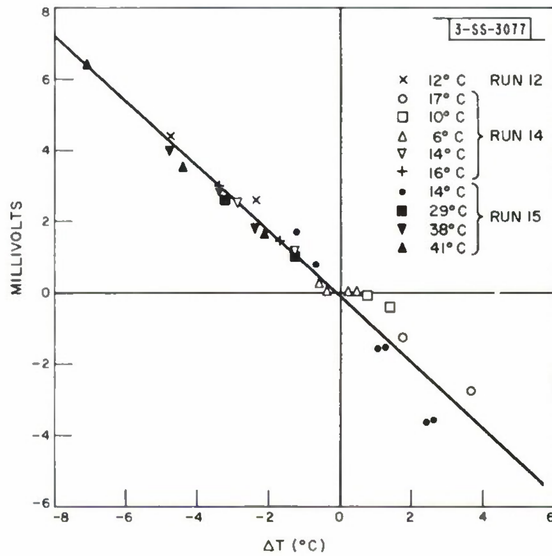

Fig. III-5. Potential difference vs temperature difference for Cr_2O_3-3% Al_2O_3.

steel rods and placed inside a stainless steel shield on which are wound two trimming resistance heaters used to maintain the desired temperature gradient across the sample. For measurements above and below room temperature, the apparatus is either heated with a clam-shell resistance furnace or cooled by a dry-ice bath surrounding the outer tube. The thermocouple voltages are measured with a K-3 potentiometer, and the voltages across the sample are measured with a Fluke Model 821A high-impedance differential voltmeter, which is completely enclosed by shielding.

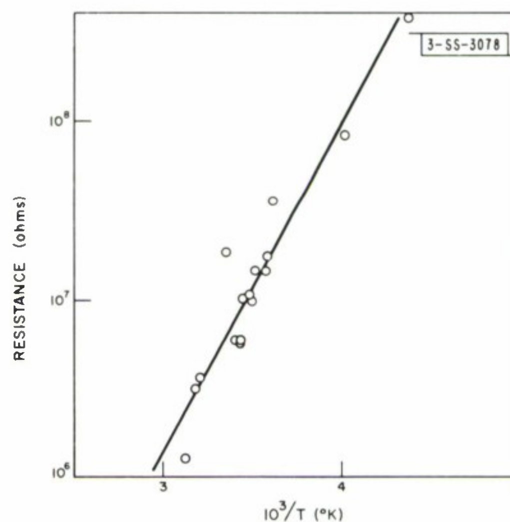

Fig. III-6. Resistonce vs recipracal temperature for Cr_2O_3-3% Al_2O_3.

The system has been used to make Seebeck measurements at average temperatures between 6° and 41°C on a crystal of Cr_2O_3-3% Al_2O_3 obtained from the Linde Company. The results are shown in Fig. III-5, where the potential difference between the platinum leads attached to the sample is plotted against the temperature difference. Since the experimental points fit a straight line, over the temperature range investigated the Seebeck coefficient has a constant value of +900 μv deg^{-1} obtained from the slope of the line. The fact that the line passes through the origin indicates that the shielding of the system was sufficient to reduce pickup voltages to a satisfactory level. The resistance of the sample was measured with the same system and the results are shown in Fig. III-6, where log R is plotted against $10^3/T$ °K. The data fit a straight line whose slope corresponds to an activation energy of 0.4 ev. Over the temperature range of the Seebeck measurements, the sample resistance varies between about 3×10^6 and 2×10^7 ohms.

D. S. Chapin
J. M. Honig

C. THERMOELECTRIC PROPERTIES OF CrO_2

The Seebeck coefficient (α) and resistivity (ρ) have been measured as a function of temperature on hot-pressed polycrystalline CrO_2 obtained by the high-pressure reaction between CrO_3 and Cr_2O_3.[1] The material is n-type and exhibits values of α and ρ which are unusually low for an oxide. In the Seebeck measurements, the plots of potential difference vs temperature difference give straight lines which pass very close to the origin. The measured values of α, corrected for the Seebeck coefficient of platinum, are plotted against $10^3/T$ °K in Fig. III-7. The data can be

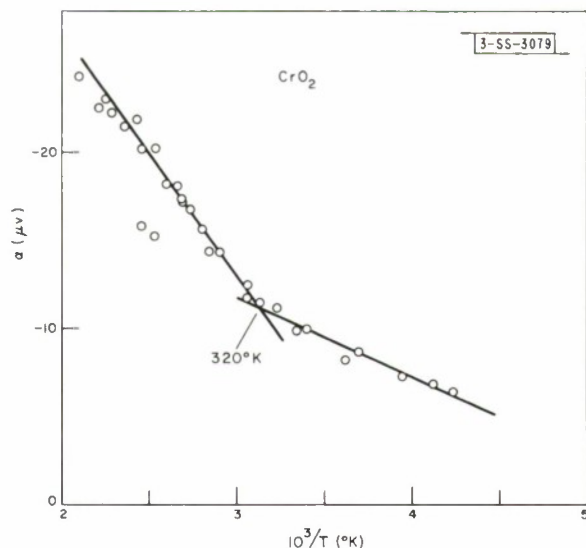

Fig. III-7. Seebeck coefficient (α) vs reciprocal temperature for hot-pressed polycrystalline CrO_2.

fitted by two straight lines intersecting at about 320°K. The values of ρ are in the range 1.2 to 4.3 milliohm-cm and generally increase with temperature between −50° and 240°C. No clear evidence was found for a maximum in ρ previously reported in the literature.[2]

D. S. Chapin
J. M. Honig

D. PROPERTIES OF n- AND p-TYPE PbSe

Electrical and optical measurements on n-type samples of Bi-doped PbSe with apparent carrier concentrations at 77°K ($n_{77}^* = 1/eR_{77}$) between 1×10^{19} and 2×10^{20} cm^{-3} were reported previously.[3] Additional measurements have been made on undoped n-type samples with n_{77}^* as low as 1.5×10^{18} cm^{-3} and on p-type samples with apparent hole concentrations at 77°K between 3×10^{17} and 5×10^{19} cm^{-3}. All samples were cut from single crystals grown in evacuated quartz ampules by the Bridgman method. The highest hole concentrations were obtained by doping with silver, while the lowest hole concentrations were obtained by annealing undoped samples under controlled selenium pressures.

Within the scatter of the data, the Hall mobilities at 4.2°, 77° and 300°K (Fig. III-8) and the thermoelectric power at 300°K (Fig. III-9) are the same for n- and p-type samples with the same carrier concentrations. (Although n-type samples with n_{77}^* between about 7×10^{18} and 4×10^{19} cm^{-3} generally have lower mobilities at 4.2°K than the corresponding p-type samples, the reduction in mobility can be attributed to compensation of the bismuth donors by acceptor lattice defects associated with stoichiometric deviations.) The highest mobilities observed at 77° and 300°K are probably about the same as the lattice mobilities at those temperatures, but the highest values observed at 4.2°K are probably considerably lower than the lattice mobility. At all three temperatures, the mobility decreases with increasing n_{77}^* over the concentration range in which impurity scattering is significant.

For the n-type samples investigated previously, it was reported that the Hall coefficient is 13 to 22 percent higher at 300° than at 77°K.[3] As shown in Fig. III-10, where R_{300}/R_{77} is plotted

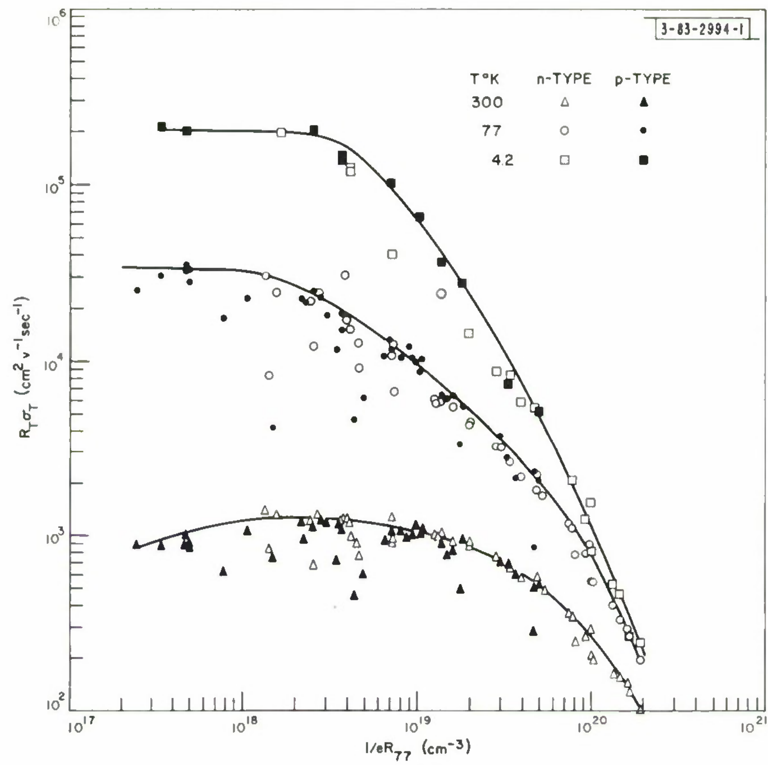

Fig. III-8. Voriotion of Holl mobility (R) with $n^*_{77} = 1/eR_{77}$ for PbSe.

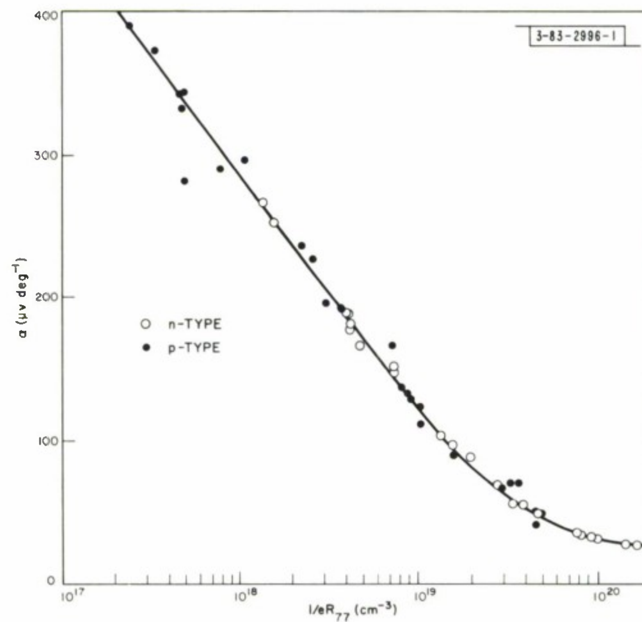

Fig. III-9. Voriotion of thermoelectric power (a) at 300°K with n^*_{77} for PbSe.

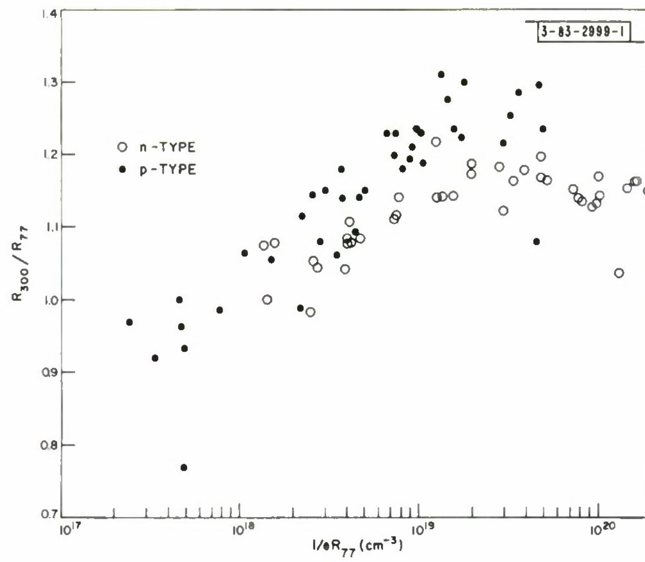

Fig. III-10. Variation of R_{300}/R_{77} with n^*_{77} for PbSe.

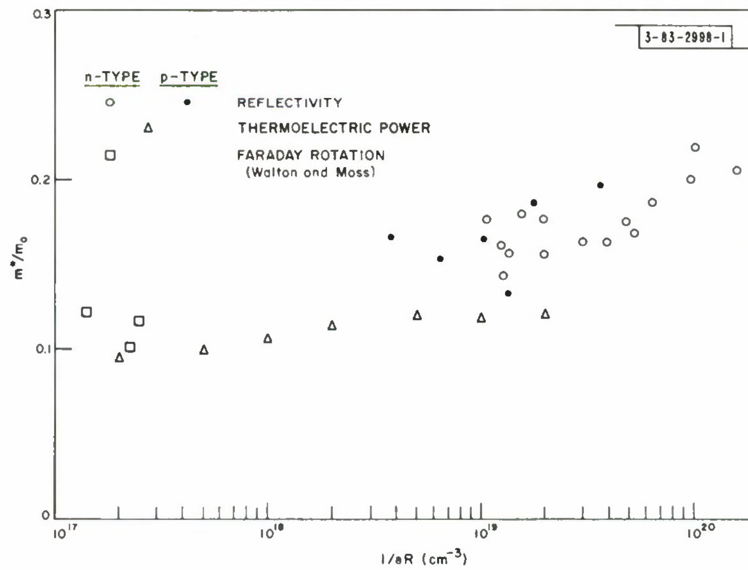

Fig. III-11. Variation of effective mass (m^*/m_o) with n^*_{77} far PbSe.

against n^*_{77}, even larger increases are exhibited by p-type samples with corresponding concentrations. For several samples, the ratio of R_{300} to R_{77} is between 1.25 and 1.30. Such values are probably too large to be attributed to a change in statistics with temperature, particularly for carrier concentrations exceeding 10^{19} cm^{-3}. Therefore, it is believed that the increases in Hall coefficient result from the thermal transfer of holes (or electrons) from the lowest valence (or conduction) band to a higher-lying band, as in the case of p-type PbTe.[4] The decrease in R_{300}/R_{77} with decreasing n^*_{77}, which is also observed for p-type PbTe, is consistent with this explanation. For sufficiently low values of n^*_{77}, R_{300}/R_{77} becomes less than unity, probably because the intrinsic carrier concentration is not negligible at 300°K.

Measurements of infrared reflectivity as a function of wavelength have been made at room temperature on a number of p-type samples which had been polished and etched. Because of the free carrier contribution to the electric susceptibility, the reflectivity exhibits a rather deep minimum previously observed for n-type samples.[3] Values of the susceptibility effective mass of holes and electrons, calculated from the reflectivity data for both p- and n-type samples by the method of Dixon and Riedl,[5] are plotted against n^*_{77} in Fig. III-11. The effective mass is apparently somewhat higher for holes than for electrons, although there is considerable scatter in the data. Effective mass values calculated from the thermoelectric power data of Fig. III-9 on the assumption of acoustic lattice scattering and a 4-ellipsoid model for both the conduction and valence bands[6] are also plotted in Fig. III-11. These values, although somewhat too low, are in reasonable agreement with those calculated from the reflectivity data and also with those obtained by Walton and Moss[7] from Faraday rotation experiments.

A. J. Strauss

E. ADSORPTION ON SPONTANEOUSLY BENT WAFERS OF III-V COMPOUNDS

Because of the elastic strain energy (ESE) associated with the distortion of the sp^3 bonds of surface atoms in the A{111} planes, {111} wafers of III-V compounds with thicknesses of the order of 10 microns are spontaneously bent. Radii of curvature and the corresponding values of ESE were reported previously for wafers of GaAs, InAs, GaSb, and InSb in air.[8] The effect of preferential adsorption on the bending of GaAs and InSb has been studied by comparing the initial curvature of wafers in air with the curvature after they have been placed in an evacuated desiccator, exposed to either NH_3 or H_2S, and removed for measurement. The results are given in Table III-1, where the thickness (t), radius of curvature (R), ESE, and relative change in ESE are tabulated. For both GaAs and InSb, the ESE is decreased by adsorption of NH_3 and increased by adsorption of H_2S.

Mary C. Finn

F. SUPERCONDUCTIVITY IN THE HIGH-PRESSURE InSb-Sn SYSTEM

It was found by alloying b. c. t. β-Sn with b. c. t. $InSb_{II}$ (Ref. 9) that the superconducting transition temperature (T_c) of $InSb_{II}$ is markedly increased [from 2.1 (Ref. 10) to 4.4°K], as shown in Fig. III-12. The increase in T_c of pure Sn when alloyed with $InSb_{II}$ is not as marked, amounting to several tenths of a degree. The T_c's of alloys of intermediate nominal concentrations are also shown in Fig. III-12. Some samples quenched directly from the melt exhibited somewhat higher T_c than those heat-treated just below the melting point before quenching. This effect is the same as the "quench effect" reported by Merriam and Von Herzen.[11]

TABLE III-1 EFFECT OF ADSORPTION ON BENDING OF {111} WAFERS					
Compound	t (microns)	Ambient	R (cm)	ESE (ergs)	$\frac{\Delta(ESE)}{(ESE)_o}$
GaAs	11.2	Air	6.0	0.42	−0.19
		NH_3	6.7	0.34	
InSb	9.8	Air	50	2.4×10^{-3}	−1.0
		NH_3	∞	0	
GaAs	13.5	Air	10.7	0.23	+1.22
		H_2S	7.2	0.51	
InSb	11.0	Air	114	6.3×10^{-4}	+0.89
		H_2S	39	5.4×10^{-3}	

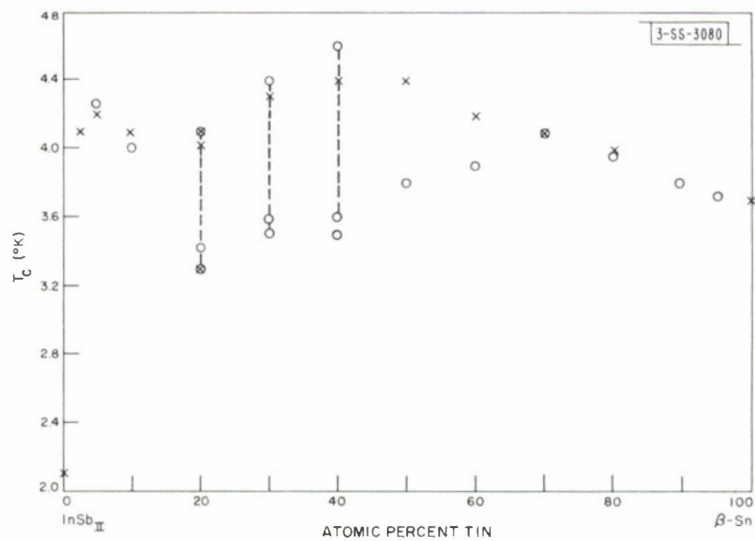

Fig. III-12. Superconducting transition temperature (T_c) vs nominal composition for $InSb_{II}$-(β-Sn) samples prepared at 37 kbar. x: samples quenched directly from the melt to room temperature. o: samples annealed at 300°C for one hour, after melting and before quenching. Dotted lines connect values of T_c for two transitions in a single sample.

The samples were prepared by pressing mixtures of high-purity InSb and tin at 37 kbar in a "belt" high-pressure unit and holding them at this pressure and at 450° to 480°C (well above their melting point) for 2 hours. Then the samples were either quenched to room temperature or annealed for one hour at 300°C, below the melting points of the constituents at this pressure. While still under pressure, the samples were cooled with liquid nitrogen to about −140°C, where $InSb_{II}$ can be retained indefinitely; the pressure was then released.

The T_c's of pure $InSb_{II}$ and pure β-Sn shown in Fig. III-12 were obtained with samples prepared by the high-pressure procedure described. In all cases, T_c was determined by self-inductance techniques, using cylindrical samples about 0.2 inch in diameter by 0.2 inch long.[12] Typical data for T_c determinations are shown in Fig. III-13.

The increase in T_c at the terminal compositions is consistent with the empirical formula proposed by Seraphim, Chiou, and Quinn[13] to describe such variations in solid solutions based on tin, aluminum, and indium with solute concentrations up to about 10 percent. Recent calculations by Markowitz and Kadanoff[14] have shown that the T_c should vary linearly with solute concentrations in the "valence" region, i.e., beyond the very dilute regions where the mean free path is greater than the coherence length.

Considering the superconducting behavior of other alloy systems, it is probable that the $InSb_{II}$-(β-Sn) system exhibits terminal solubilities, with a 2-phase region in the middle portion

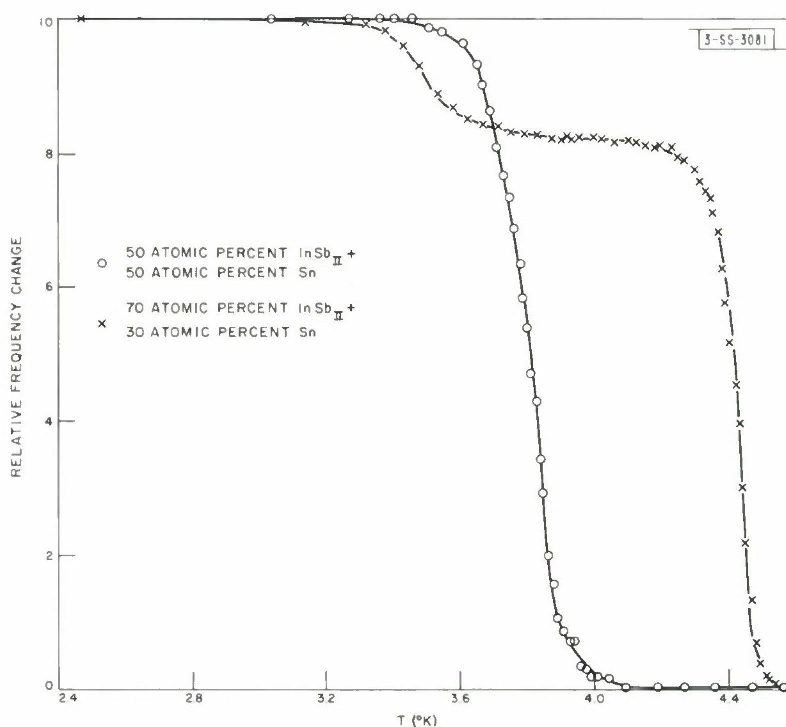

Fig. III-13. Typical curves of relative change in frequency vs temperature for $InSb_{II}$-(β-Sn) samples. Initial frequency in normal state was 1005 to 1105 cps; total frequency change was 20 to 55 cps. Frequency change for a single sharp transition was about twice the total change for two transitions in a single sample.

of the composition range. Some samples, both quenched and annealed, containing 20, 30, and 40 nominal atomic percent β-Sn exhibited two distinct superconducting transitions, as indicated in Fig. III-13. The nature of the phases responsible for the two transitions is not clear. Similar double transitions were reported in the In-Sn system,[11] where the "quench effect" was also observed and has been explained on the basis of internal strains. Consistent with this explanation, the "quench effect" in the systems reported previously has been found to be the most pronounced in the alloys falling in a 2-phase region and not at all pronounced in the pure elements. In the present case also, the "quench effect" is not observed near the terminal compositions. It thus seems likely that here, too, the "quench effect" has the same origin as in the In-Sn system.

It appears that the solubility of β-Sn in $InSb_{II}$ is 2.5 to 5 percent and that the solubility of $InSb_{II}$ in β-Sn is about 35 percent. It is of interest to point out that the solubility of β-Sn in normal InSb (zinc-blende structure) is less than 0.5 percent, and that of normal InSb in tin is about 8 percent.[15] Although there seems to be an appreciable increase in solubilities by transforming InSb into its high-pressure phase, it is still surprising that $InSb_{II}$ and β-Sn are not completely soluble; not only do they have the same structure, but their lattice constants are also very similar [$InSb_{II}$: $a = 5.79$, $c = 3.15$ Å (Ref. 16); Sn: $a = 5.819$, $c = 3.175$ Å]. The application of x-ray diffraction for the conclusive determination of the $InSb_{II}$-(β-Sn) phase diagram is extremely difficult in view of the structural similarities of the two constituents and the inherent strain of $InSb_{II}$ retained at low temperatures.[16]

M. D. Banus
Susan D. Nye

G. CHEMICAL ANALYSIS OF HgS-HgSe ALLOYS

An analytical procedure is being developed to determine the three major constituents of HgS-HgSe alloys. The EDTA titration described previously[17] can be used to determine mercury, if the sample is dissolved under reflux to prevent loss of mercury. Selenium is determined by a potentiometric titration[18] after the chloride ion is removed by volatilization.

Methods of sulfur determination are currently under investigation. A method described by Sporek,[19] in which $PbSO_4$ is precipitated, dissolved in excess EDTA, and back-titrated with standard zinc solution, was found to be unsatisfactory. The gravimetric $BaSO_4$ procedure gives results accurate to about 2 percent in the presence of selenium. Analyses accurate to within 1 to 2 percent have been obtained with an amperometric method[20] based on the titration of the sulfate with a lead solution. Preliminary experiments indicate the feasibility of removing mercury and selenium by controlled potential electrolysis prior to the sulfur determination. In any event, since sulfur is the minor constituent in the alloys to be analyzed, it is not necessary for the sulfur analysis to be so accurate as the analyses for mercury and selenium.

M. C. Gardels
J. C. Cornwell

REFERENCES

1. Solid State Research Report, Lincoln Laboratory, M.I.T. (1963:3), p.21, DDC 427340.
2. B. Kubota and E. Hirota, J. Phys. Soc. Japan 16, 345 (1961).
3. Solid State Research Report, Lincoln Laboratory, M.I.T. (1963:2), p.13, DDC 417686.
4. R.S. Allgaier, J. Appl. Phys. Supp. 32, 2185 (1961). R.S. Allgaier and B.B. Houston, Proceedings of the International Conference on Physics of Semiconductors, Exeter (1962), p.172.
5. J.R. Dixon and H.R. Riedl, Proceedings of the International Conference on Physics of Semiconductors, Exeter (1962), p.179.
6. M.R. Ellett and K.F. Cuff, Bull. Am. Phys. Soc. 8, 601 (1963).
7. A.K. Walton and T.S. Moss, Proc. Phys. Soc. 81, 509 (1963).
8. Ref.1, p.22.
9. M.D. Banus, R.E. Hanneman, A.N. Mariano, E.P. Warekois, H.C. Gatos, and J.A. Kafalas, Appl. Phys. Letters 2, 35 (1963).
10. S. Geller, D.B. McWhan, and G.W. Hull, Jr., Science 140, 62 (1963).
11. M.F. Merriam and M. Von Herzen, Phys. Rev. 131, 637 (1963).
12. T.B. Reed, H.C. Gatos, W.J. LaFleur, and J.T. Roddy, Metallurgy of Advanced Electronic Materials, G.E. Brock, Ed. (Interscience, New York, 1963), p.71.
13. D.P. Seraphim, C. Chiou, and D.J. Quinn, Acta Met. 9, 861 (1961).
14. D. Markowitz and L.P. Kadanoff, Phys. Rev. 131, 563 (1963).
15. J.C. Woolley and D.G. Lees, J. Less Common Metals 1, 192 (1959).
16. R.E. Hanneman, M.D. Banus, H.C. Gatos, J. Phys. Chem. Solids (in press).
17. Ref.1, pp.27-29.
18. Ref.3, p.17.
19. K.F. Sporek, Anal. Chem. 30, 1032 (1958).
20. I.M. Kolthoff and Y. Pan, J. Am. Chem. Soc. 62, 3332 (1940).

IV. BAND STRUCTURE AND SPECTROSCOPY OF SOLIDS

A. BAND-EDGE STRUCTURE OF PbS, PbSe, AND PbTe

A pseudopotential calculation has shown that both the conduction and valence band extrema for PbS, PbSe, and PbTe are likely to occur at the L-point (111 edge) of the Brillouin zone. Three valence bands and three conduction bands have been predicted to lie near the forbidden gap. These bands interact strongly with one another and are well isolated in energy from other bands at L. The forms of the dispersion relations $E(\vec{k})$ for these bands, as determined by symmetry and by $\vec{k} \cdot \vec{P}$ perturbation theory, depend strongly on their order and spacing. The conduction and valence band extrema may be either anisotropic, with small, highly concentration-dependent transverse masses, as found in PbTe, or more nearly isotropic, as found in PbS and PbSe. The theoretical variation with carrier concentration of the cyclotron effective masses and extremal cross-sectional areas of the Fermi surface have been derived from $\vec{k} \cdot \vec{P}$ perturbation theory, for models of the band structures in these compounds. Good agreement with experiment can be obtained by varying, from compound to compound, the order and spacing of the six bands at L. The phenomenological momentum matrix elements obtained by comparison with experiment are in reasonable agreement with those calculated from the eigenfunctions of the pseudopotential. Formulas for the g-tensors for models of the band structure at L in PbS, PbSe, and PbTe have also been obtained and compared with available experimental data. The possibility of conduction and valence band extrema located at other points in the Brillouin zone is considered. This work is being prepared for publication.

J. O. Dimmock
G. B. Wright

B. MAGNETOREFLECTION EXPERIMENTS IN PYROLYTIC GRAPHITE*

The previously reported magnetoreflection measurements on pyrolytic graphite have been extended to magnetic fields up to 110 kgauss. By using higher magnetic fields on a sample of higher crystalline perfection, we have been able to extend the observation of interband transitions up to photon energies of ~0.5 ev. In the photon energy range $\hbar\omega \lesssim 0.2$ ev, interband transitions have been observed for the first time at room temperature. For very low photon energies, the higher magnetic fields have made possible the observation of several new transitions with behavior comparable to the so-called "quantum effects" observed in the millimeter cyclotron resonance experiments in semiconductors.[1]

Mildred S. Dresselhaus
J. G. Mavroides

C. QUANTUM THEORY OF THE INTERBAND FARADAY AND VOIGT EFFECTS

The quantum-mechanical analysis of the Voigt effect previously reported[2] has been modified to take account of second-order terms in the magnetic field in the P^+ and P^- matrix elements,

---

*Measurements carried out at the National Magnet Laboratory, M.I.T.

which are not canceled out by the P^z terms. The ansatz that the oscillator strength for the "z" transitions is equal to an oscillator strength, suitably averaged, for the "±" transitions leads, in a natural way, to a relation between the matrix elements consistent with the theoretical work of Burstein, *et al.*[3] and also gives a result in the long-wavelength region that is identical in form to that of the semiclassical analysis of Kolodziejczak, Lax, and Nishina.[4] The choice of relation between matrix elements affects only the long-wavelength limit. The terms in question do not give rise to singularities, and hence the line shapes in the vicinity of a Landau level remain the same as for the original analysis.

J. Halpern
B. Lax

D. INDIRECT INTERBAND TRANSITION IN GERMANIUM*

A study is being made at 1.5°K of the interband magneto-optical absorption of the indirect transition in germanium. The data were taken in the Faraday configuration (magnetic field parallel to the direction of propagation), using samples with impurity concentrations on the order of 10^{13} cm^{-3}. At 74 kgauss, as many as 18 distinct transitions between Landau levels were observed, some of which had structure which will be further investigated. At approximately 50 kgauss, the transition energy began to rise quadratically with the magnetic field. Preliminary data have also been taken on the indirect exciton, in order to study its fine structure more closely.

J. Halpern
B. Lax

E. EFFECTS OF UNIAXIAL STRESS ON THE INFRARED ABSORPTION OF SULFUR-DOPED SILICON

The absorption spectrum of sulfur impurities in silicon has been previously reported.[5] The effects of uniaxial stress on these absorption lines are now being studied. Shifts in the energies, splittings, and polarization effects due to the applied stress have been observed in the absorption lines attributed to states which, in the effective mass approximation, are excited 1s-like states of the impurities. Shifts in the energies of the transitions to the p-like states have also been observed. It is expected that these stress measurements will help to clarify the nature of many of the transitions which have been observed. Observations of these transitions are continuing but, because in many cases the character of the shift at low strain is important, it will be necessary to install a more sensitive detector in our spectrometer.

W. E. Krag
H. J. Zeiger
W. H. Kleiner

F. DERIVATION AND PROPERTIES OF GENERALIZED MASTER EQUATIONS

We have derived generalized master equations for an arbitrary system with a Hamiltonian $H = H_o + V$ for both the diagonal and off-diagonal elements of the density operator ρ in the unperturbed representation $|\alpha\rangle$. For the diagonal elements $\langle\alpha|\rho|\alpha\rangle \equiv f_\alpha$, these have the form (for $t > 0$)

---

*Measurements carried out at the National Magnet Laboratory, M.I.T.

$$\frac{d}{dt} f_{\alpha}(t) = \int_{0}^{t} d\tau \sum_{\alpha'} \{w_{\alpha\alpha'}(t-\tau) f_{\alpha'}(\tau) - w_{\alpha\alpha'}(t-\tau) f_{\alpha}(\tau)\} + F_{\alpha}(t) \quad (1)$$

where

$$w_{\alpha\alpha'}(t) = -\mathrm{Tr}\{|\alpha\rangle \langle\alpha| \mathcal{V} e^{-i\mathcal{P}'\mathcal{H}t} \mathcal{V} |\alpha'\rangle \langle\alpha'|\}$$

$$F_{\alpha}(t) = -i \langle\alpha| \mathcal{V} e^{-i\mathcal{P}'\mathcal{H}t} \mathcal{P}'\rho(0)|\alpha\rangle \quad .$$

$\mathcal{H}$ and $\mathcal{V}$ stand for the Liouville operators corresponding to H and V, defined by $\mathcal{H}\rho \equiv [H,\rho]$. $\mathcal{P}'$ is a projection operator defined by: $\langle\alpha|\mathcal{P}'\rho|\alpha'\rangle = (1-\delta_{\alpha\alpha'})\,\rho_{\alpha\alpha'}$. The off-diagonal elements $\rho_{\alpha\alpha'}(\alpha' \neq \alpha)$ satisfy an analogous equation.

The derivation of Eq. (1), which will be published elsewhere, is simple and makes essential use of the algebra of Liouville operators.

The compact form of $w_{\alpha\alpha'}(t)$ has allowed us to establish its physical significance, by relating it to the transition probability rate

$$S_{\alpha\alpha'}(t) = \frac{d}{dt} |\langle\alpha|t\rangle|^2 \quad \text{when} \quad |t=0\rangle = |\alpha'\rangle \quad .$$

Explicitly, for the Fourier transforms of the matrices $w_{\alpha\alpha'}(t)$, $S_{\alpha\alpha'}(t)$, where

$$w(z) = \int_{0}^{\infty} dt\, e^{izt} w(t) \quad (\mathrm{Im}\, z \geq \epsilon > 0)$$

and similarly for S(z), we have found the interesting relation:

$$\frac{w(z)}{-iz} = S(z)\,[1 + S(z)]^{-1} \quad .$$

This allows us to use all the results of scattering theory in the theory of the master equations.

The method of derivation of these results is easily applicable to more general situations.

P. N. Argyres

G. THEORY OF TRANSPORT EQUATIONS IN INHOMOGENEOUS DRIVING FIELDS

A direct and rigorous method has been devised for deriving transport equations for electrons in semiconductors and metals in the presence of inhomogeneous and time-varying fields of force. Scattering by static impurities has been considered in detail for free, Landau, and Block electrons. Formal transport equations valid for arbitrary strength of the electron-impurity interaction and for arbitrary space-time variation of the driving field have been derived. These are non-Markoffian equations which allow for memory effects and describe, without any assumptions, the interference effects between the driving field and the scattering. A systematic expansion of the formal scattering operator, which is valid for arbitrary strength of the electron-impurity interaction, has been carried out for small interaction. The conditions under which such an expansion is valid have been deduced. This expansion makes essential use of the resolvent operator. The physical meaning of the various terms of the collision operator has been uncovered

in a general and simple way. The usual Boltzmann equation is discussed and its limitations pointed out.

P. N. Argyres

H. TRANSPORT PROPERTIES OF BISMUTH

The transport theory previously developed[6] for anisotropic materials has been applied to the Jones-Shoenberg model for bismuth. According to this model, the conduction band exhibits three or six half-ellipsoids lying along the threefold binary axes, and tilted out of the trigonal plane. The conduction band contains one or two half-ellipsoids lying along the trigonal axis.

The first step in the procedure consists in correcting for the tilt of the conduction band ellipsoids by carrying out a similarity transformation on the various galvano-thermomagnetic (GTM) tensors. The second step consists in expressing all GTM properties associated with a given ellipsoid in terms of the common-crystal-symmetry coordinate system. Again, this is done by carrying out appropriate similarity transformations on the various GTM tensors. The results were found to be extremely unwieldy, and it was advisable to specialize by considering when the magnetic field lies along one of the crystal-symmetry axes, and by going to the low- and high-field limiting cases. Advantage was also taken of the fact that in bismuth the mobility of electrons along the bisectrix direction is negligible compared with those along the binary axis, whereas the two mobilities are equal for holes in the valence band. On carrying through the necessary mathematical manipulations, one arrives at a set of GTM tensors. These are listed in a preprint.

The theoretical predictions are in excellent agreement with experimental data. In the limit of weak fields (excluding terms of order H^2 or higher), the theory specifies two independent (zero-field) resistivities, two Seebeck (zero field), two Hall, and three Nernst coefficients. In the limit of strong magnetic fields aligned with the symmetry axes, the theory predicts three longitudinal, four transverse, and two off-diagonal resistivities; three Hall and one planar Hall coefficients; three longitudinal, five transverse, and three off-diagonal Seebeck coefficients; four Nernst and two planar Nernst coefficients.

T. C. Harman
J. M. Honig
Bette M. Tarmy

I. THEORY OF THE INFINITE-STAGE NERNST-ETTINGSHAUSEN REFRIGERATOR

In connection with the experiments currently in progress (Sec. IV-J), the theory for an infinite-stage Nernst-Ettingshausen refrigerator was developed. Such a device can be constructed by proper shaping of the device arm. By adapting the previous theory concerning the

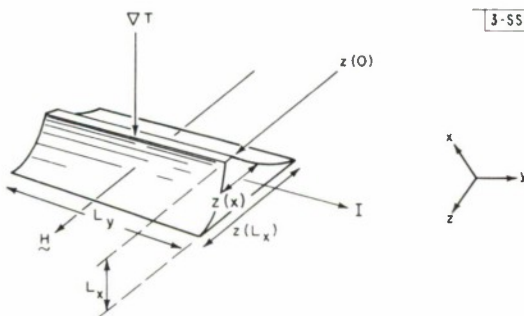

Fig. IV-1. Shaped sample, equivalent to infinite stage cascade, for use as Nernst-Ettingshausen refrigerator. Direction of current flow I, magnetic field H, and temperature gradient ∇T are indicated.

operating characteristics of parallelepiped-shaped samples[7] to the present case, and utilizing the theory first developed by Rittner,[8] it can be shown that the sample depicted in Fig. IV-1 must be shaped according to the requirement

$$z(x)/z(0) = [z(L_x)/z(0)]^{x/L_x} \quad .$$

The temperatures at the cold and hot junctions T_L and T_o obey the relation

$$z(L_x)/z(0) = (T_L/T_o)^{(1+\delta)/(1-\delta)}$$

where $\delta = \sqrt{1 - Z\overline{T}}$, $\overline{T} = (T_L + T_o)/2$, and Z is the figure of merit appropriate to Nernst-Ettingshausen energy conversion devices.[7] It follows from the theory that, if $z(L_x)/z(0) \gg 1$, for any particular hot-junction temperature T_L, the cold junction would be cooled to very near absolute zero for any nonzero value of Z, providing that the sample shape follows the form prescribed above.

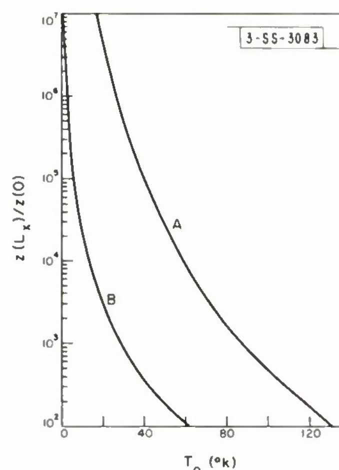

Fig. IV-2. Geometry ratio $z(L_x)/z(0)$ vs T_o for $Z\overline{T} = 0.5$ (curve A) ond $Z\overline{T} = 0.7$ (curve B), ossuming hot-junction temperoture T_L of 290°K.

The cold-junction temperatures predicted for given ratios of $z(L_x)/z(0)$ and for $Z\overline{T}$ values of 0.5 and 0.7 are depicted in Fig. IV-2. A $z(L_x)/z(0)$ ratio of 10^2 is considered practical, whereas the value of 10^7 is considered impractical. With a hot-junction temperature of 290°K, cold-junction temperatures between 60° and 100°K should ultimately be reached.

Experiments testing the theory are currently in progress.

T. C. Harman

J. EXPERIMENTS ON ROOM TEMPERATURE NERNST-ETTINGSHAUSEN REFRIGERATORS*

Unusually large crystals of bismuth were prepared as described elsewhere[9] and cut into the desired shapes by use of a spark-erosion cutter.[10] The sample was mounted in a specially designed holder through which water was circulated to keep one face of the bismuth crystal at nearly constant temperature throughout the experiments. The assembly was placed in an electromagnet,

*Measurements carried out at the National Magnet Laboratory, M.I.T.

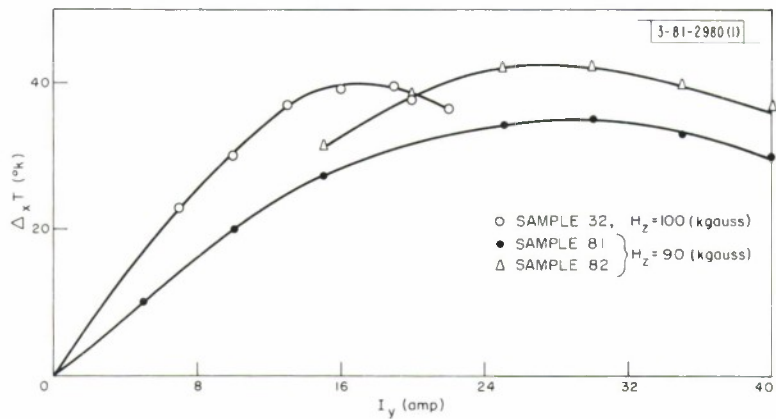

Fig. IV-3. Plots of number of degrees of cooling obtained with $\Delta_x T$ vs electrical current flow I_Y through device at $H_z \simeq 90$ kgauss for parallelepiped-shaped elements.

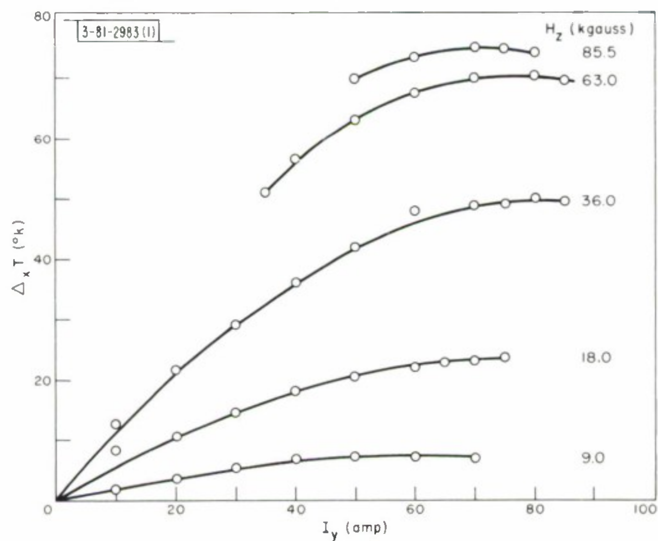

Fig. IV-4. Experimental curves of $\Delta_x T$ vs I_Y for various magnetic field strengths for shape ratio of 12 and hot-junction temperature of 277.4°K.

so that the magnetic field pointed along the bisectrix axis; current was then passed through the sample along its trigonal crystal axis, and the resulting temperature difference across the sample along the binary axis was monitored by means of thermocouples.

Curves depicting the cooling achieved with different parallelepiped-shaped samples for various electric currents are shown in Fig. IV-3. The optimal temperature difference and associated electric currents are in reasonably satisfactory agreement with theoretical predictions; discrepancies are principally due to the voltage short-circuiting effects in the vicinity of the electrical junctions.

Temperature differences obtained with an exponentially shaped sample (Fig. IV-1), which is equivalent to an infinite stage, are shown in Fig. IV-4. The largest observed temperature difference was 76° at a current of approximately 70 amp in a magnetic field of approximately 86 kgauss; the predicted value was 67° for a shape ratio (Sec. IV-I) $z(L_x)/z(0) \approx 12$. The greater cooling, compared with that predicted theoretically, is attributed to the fact that the temperature dependence of the transport properties have not been taken into account in the theory. It is noteworthy that the steady-state temperature at each value of the magnetic field was reached within a few seconds after turning on the current. Furthermore, on imposing a heat load on the hot junction by operating in air rather than in vacuum, the temperature difference between the hot and cold junctions was reduced by only a few degrees.

Further experiments are in progress.

T. C. Harman
J. M. Honig
S. Fischler
A. E. Paladino
M. Jane Button

REFERENCES

1. J. J. Stickler, H. J. Zeiger, and G. S. Heller, Phys. Rev. 127, 1077 (1962).
2. Solid State Research Report, Lincoln Laboratory, M. I. T. (1963:2), p. 21, DDC 417686.
3. E. Burstein, G. S. Picus, R. F. Wallis, and F. Blatt, Phys. Rev. 113, 15 (1959).
4. J. Kolodziejczak, B. Lax, and Y. Nishina, Phys. Rev. 128, 2655 (1962).
5. W. E. Krag and H. J. Zeiger, Phys. Rev. Letters 8, 145 (1962).
6. Ref. 2, p. 24; op. cit. (1963:3), pp. 32-33.
7. T. C. Harman, J. M. Honig, and B. M. Tarmy, J. Appl. Phys. 34, 2225 (1963).
8. E. S. Rittner, J. Appl. Phys. 30, 702 (1959).
9. S. Fischler, Electronic Materials Conference, AIME, Boston, 23-26 August 1963 (to be published).
10. H. H. Ehlers and D. F. Kolesar, "Specimen Preparation by Spark-Erosion Cutting," Technical Report 303, Lincoln Laboratory, M. I. T. (14 March 1963), DDC 402938.

V. MAGNETISM AND RESONANCE

A. SAMPLE PREPARATION

1. Single-Crystal Growth from Polytungstate Fluxes

Recent advances in the theoretical understanding and experimental interest of pure ferrite, chromite, and vanadite powdered samples has created a need for single crystals of these materials. Each of the series of compounds mentioned has a unique set of problems related to crystal growth, which differ widely from one series to another. Growth of stoichiometric ferrite crystals is difficult, because the melting points of these compounds are higher than the dissociation temperature of ferric oxide in oxygen at atmospheric pressure. The chromite series of compounds, although usually quite stable, has extremely high melting points (approximately 2000°C and greater), thus creating the problem of finding a container that is both inert and capable of withstanding such temperatures. The vanadite series requires that the vanadium be in a lower-than-normal valence state, necessitating an atmosphere such as CO/CO_2 to maintain stoichiometry. In addition, there is considerable doubt as to the stability of vanadites at the elevated temperatures that would be required in a direct (fused melt) synthesis of single crystals.[1]

Ferrites have been successfully grown from molten borax,[2] lead oxide,[3] sodium carbonate,[4] sodium ferrite,[5] and ferrite melts under high oxygen pressure.[6] Little or no work has been performed on the single-crystal synthesis of chromites or vanadites. We have found that manganese chromite ($MnCr_2O_4$) can be melted at 2000°C in an iridium crucible with RF heating; the stoichiometry is maintained by use of an argon-hydrogen-water-vapor atmosphere. The oxygen partial pressure of this system relies on the equilibrium between the decomposition of water vapor in the presence of excess hydrogen. A direct synthesis of $MnCr_2O_4$ single crystals via this technique is in progress. It is doubtful that any members other than $MnCr_2O_4$ and the alkaline-earth chromites can be produced by a direct fusion of the compound.

To circumvent all the difficulties previously described, an extremely versatile flux system has been developed which yields predictable results. Usually, an adequate flux system for the growth of a particular species of crystals is found by trial and error, and the conditions for crystal growth are unique for each system. The inability to utilize the flux for other systems can generally be traced to ignorance concerning the solution process. The flux system described below differs from the usual in that the solution process is known, and predictable results, based on thermodynamic calculations, can be made with good accuracy.

Fundamentally, the flux system can be described in terms of the Lewis acid-base theory in that the basic oxides (transition metal oxides) are dissolved by a strong Lewis acid (WO_3) and then reprecipitated by a strong Lewis base (Na_2WO_4). This process of solution and precipitation is carried out by the equilibrium reaction

$$Na_2W_2O_7 \rightleftarrows Na_2WO_4 + WO_3 \quad . \qquad (1)$$

Sodium pyrotungstate ($Na_2W_2O_7$) is a relatively stable compound at lower temperatures, dissociating only slightly into the acid-base components. As the temperature increases, the

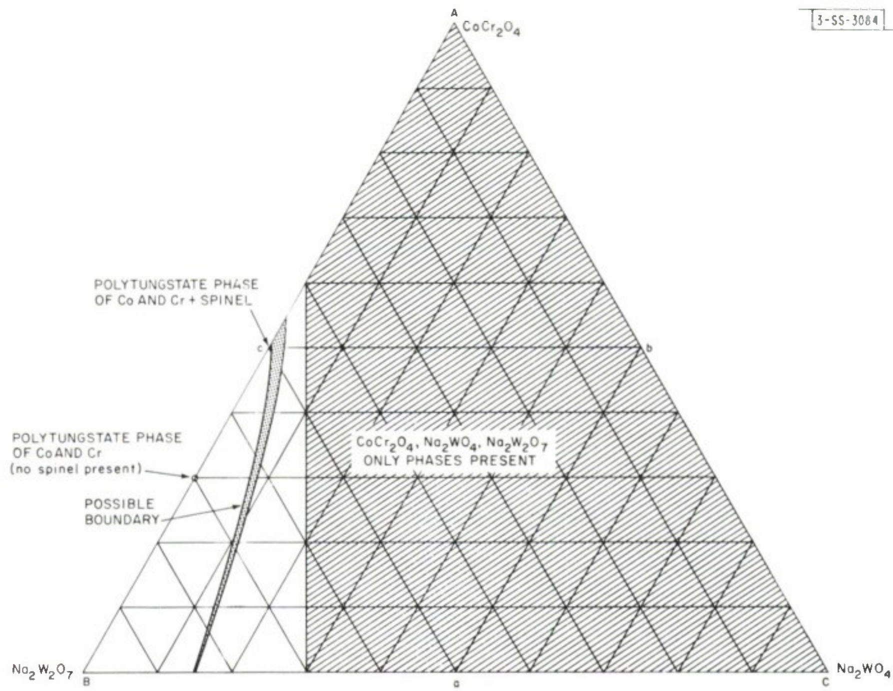

Fig. V-1. Partial phase diagram far system $CaCr_2O_4$-$Na_2W_2O_7$.

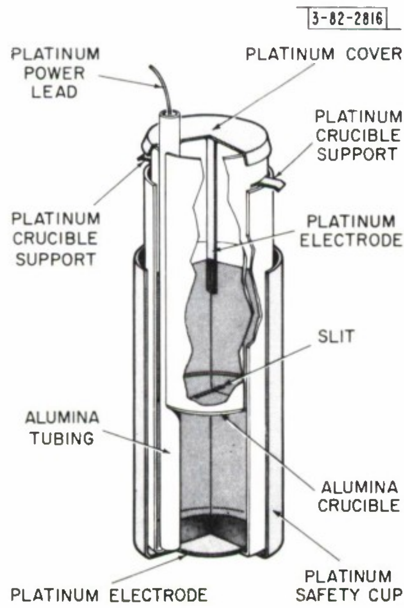

Fig. V-2. Cutaway view of assembled cell.

equilibrium is shifted rapidly toward the right as described by Eq. (1). Consequently, as the temperature increases, more acid is produced to dissolve the spinel; the process reverses as the temperature decreases. The melting points of sodium pyrotungstate-tungstate melts are quite low (500° to 800°C), permitting the use of comparatively low operating temperatures for single-crystal synthesis.

Figure V-1 shows the phases that appear in the $CoCr_2O_4$-$Na_2W_2O_7$ system as determined by the x-ray analysis of fused samples. The exact position of the indicated phase boundary has not yet been determined, and that which is represented is a proposed boundary.

To date, it has been found that $CoCr_2O_4$, $CoFe_2O_4$, CoV_2O_4, $ZnCr_2O_4$, $MnCr_2O_4$ all crystallize from this flux system. The system also appears to be adaptable to electrolytic growth of material that possesses reduced valences. This possibility is presently under investigation.

W. Kunnmann   A. Ferretti
R. Arnott   D. B. Rogers

2. A Ceramic Double Cell for Crystal Growth by Fused Salt Electrolysis

Under conditions of low current density, it is often possible to maintain stepwise valence changes leading to an insoluble product that is slowly precipitated at the electrode. This situation is well adapted to the growth of many types of single crystals that contain cations with multiple possible valences. For example, good yields of MoO_2 single crystals have been obtained by electrolytic reduction from a flux of $Na_2Mo_2O_7$ at temperatures greater than 600°C. An inherent difficulty of crystal growth by the electrolytic technique occurs where multivalence changes of partially soluble products are involved. Under the required conditions of a low current density, electrical reaction between the redox products and the electrodes can occur in an opposite direction to that desired. This cyclic process leads to low yields and poor crystal formation. We have found that this difficulty is easily precluded by the use of a ceramic double cell. The essential advantage of such an arrangement lies in the fact that good physical separation of the redox product and of any intermediate phase from the vicinity of the opposite electrode is maintained.

The essential features of the double cell are shown in Fig. V-2. The cell consists primarily of two close-fitting, concentric crucibles of "recrystallized" alumina. The inner crucible has a 0.010- by 0.5-inch slit cut through the bottom. The side and bottom edges of this crucible have also been cut to accommodate, with minimum clearance, a 5/15-inch o.d. heavy-wall alumina tube. This tube, extending from the bottom of the outer crucible to the top edge of the inner crucible, serves as an insulator for a platinum lead wire that is attached to the cell cathode at the bottom of the outer crucible. The cell anode is in the form of a platinum strip that extends from a platinum cover into the inner crucible. A platinum wire connects the cell cover to an appropriate power supply.

Efficiency of the double cell is high and satisfactory operation can be maintained when 1.68×10^{-4} (or more) equivalents per hour are generated in the reaction chambers. Crystal growth is often initiated under these conditions. We have obtained single crystals of several transition-metal reduced oxides and "mixed" oxides by utilizing this technique. A typical example is the

growth of Na-Mo bronzes ($Na_xMo_6O_{18-x}$). This process depends on the stepwise reduction at the cathode of Mo^{+6} to a lower valence state with the corresponding formation of the insoluble bronze. Each half of the double cell is filled with this material and the cell is placed in the constant-temperature portion of a suitable furnace. The furnace temperature is raised slowly to 550°C and electrolysis of the fused flux is begun.

In general, carrying out the electrolysis over a one-week period at a current density of 20 ma cm^{-1} per number of electrons transferred is a reasonable compromise for the rate of production consistent with good crystal growth and stoichiometry.[7]

W. Kunnmann
A. Ferretti

3. Compounds with B31 $\rightleftarrows$ $B8_1$ Transitions

In order to test the hypothesis that the spin correlations among narrow-band electrons can be extrapolated from superexchange theory for the spin correlations among localized electrons, studies of a number of compounds with B31 structure have been undertaken. The orthorhombic B31 structure is a distortion of the hexagonal $B8_1$ structure of NiAs. The distortion is caused by a displacement toward one another in the basal plane of the two body-centered-orthorhombic cation subarrays of the NiAs structure. It has been suggested[8] that this distortion reflects metal-metal bonding between near neighbors in the basal plane of the B31 structure, and that B31 $\rightleftarrows$ $B8_1$ crystallographic transitions should occur below the melting point in some systems.

The compound MnAs is peculiar in that it exhibits two transitions: $B8_1$ $\rightleftarrows$ B31 $\rightleftarrows$ $B8_1$ at about 313° and 400°K, respectively. The low-temperature transition coincides with a Curie temperature, which suggests that magnetic energy is responsible for restabilizing the $B8_1$ phase at the lower temperatures. The first-order phase change at the Curie temperature has been interpreted by Bean and Rodbell[9] to reflect a temperature-dependent exchange interaction in a material with large thermal-expansion coefficient. An alternate explanation, however, is that the first-order phase change at the Curie temperature reflects a partial quenching of the spin. Partial spin quenching is possible if a narrow d-electron band of β-spin overlaps the upper, occupied d-electron levels of α-spin. In MnAs, the c-axis-directed d-orbitals should form a band of collective-electron states.

In order to distinguish between these two interpretations of MnAs, a study of the systems MnP-MnAs and MnAs-MnSb has been initiated. If partial spin quenching is responsible for the properties of MnAs, substitutions of phosphorus for arsenic, which decrease the cell size and therefore increase the ligand-field splittings, will enhance the spin quenching, whereas substitutions of antimony for arsenic will reduce and ultimately eliminate spin quenching.

Preliminary experiments indicate: (a) The first-order phase change at the Curie temperature of MnAs occurs at 313°K if there is a slight excess of manganese, but is reduced to between 290° and 305°K in a slight (<1 percent) excess of arsenic; the temperature range for the transition apparently reflects small chemical inhomogeneities in the powdered sample. This suggests that the $B8_1$ $\rightleftarrows$ B31 transition is unusually sensitive to small variations in manganese (perhaps small variations in interstitial manganese). (b) Upon replacing 5 atomic percent of the arsenic by phosphorus, there is only one transition, which appears to be B31 $\rightleftarrows$ $B8_1$; the low-temperature

phase appears at about 275°K and is definitely established below 255°K. By 10 atomic percent phosphor, the low-temperature phase is established below 390°K. (c) Preliminary magnetic measurements on a powder sample of $MnAs_{0.9}P_{0.1}$ showed that saturation was not achieved in fields as high as 17,000 oe, which is indicative of extremely high anisotropy. The Curie temperature is $T_c \approx 230°$ to 240°K, which is well below the crystallographic transition. Although it is dangerous to make conclusions about the magnitude of the atomic moment from unsaturated magnetization measurements, the results are compatible with considerable spin quenching in $MnAs_{0.9}P_{0.1}$.

J. B. Goodenough
D. H. Ridgley
W. A. Newman

B. MEASUREMENTS

1. Antiferromagnetic Resonance in $YCrO_3$

Zero-field AFMR measurements as a function of temperature were made on powdered $YCrO_3$ samples.* Measured zero-field resonance frequency vs temperature, together with a Brillouin function curve for S = 3/2, is shown in Fig. V-3. The spectrometer operated from 8- to 1.6-mm wavelength, using third-harmonic power generated by a crystal frequency multiplier for the shorter wavelengths. Extrapolation of the data to zero temperature gave a critical resonant frequency of 198 kMcps for the sample. A Néel temperature of 129°K, determined by extrapolating the resonant frequency to zero, was in good agreement with the temperature observed for the disappearance of the paramagnetic resonance with decreasing temperature.

J. J. Stickler

2. Superconductivity

a. Apparatus

An article entitled "Variable Temperature Cryogenic Chamber" has been prepared for submission to the Review of Scientific Instruments. The chamber described has been used in this laboratory in experiments in which the resistive transition of superconducting niobium was measured, as described in earlier Solid State Research reports. The abstract of the article follows.

A sample chamber is described which provides continuously variable temperatures from the liquid helium range to room temperature and can be used with superconducting solenoids or with conventional magnets. It should be most useful where low temperatures must be maintained despite substantial heat dissipation in the sample. Relatively rapid variations of temperature are possible. The present system is designed for precision of about ±0.1°K, but greater precision should be possible if required.

E. S. Rosenblum
S. H. Autler
K. H. Gooen (National Magnet Laboratory, M.I.T.)

* The samples were prepared by A. Wold.

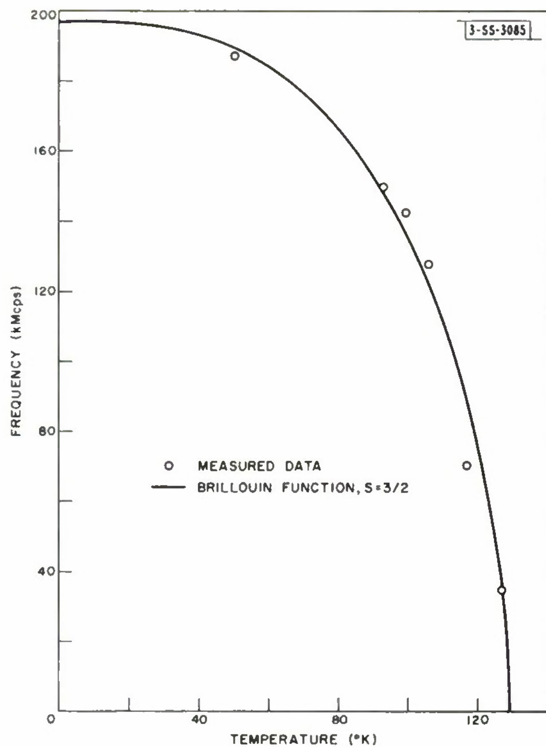

Fig. V-3. Zero-field antiferromagnetic resonant frequency vs temperature for $YCrO_3$.

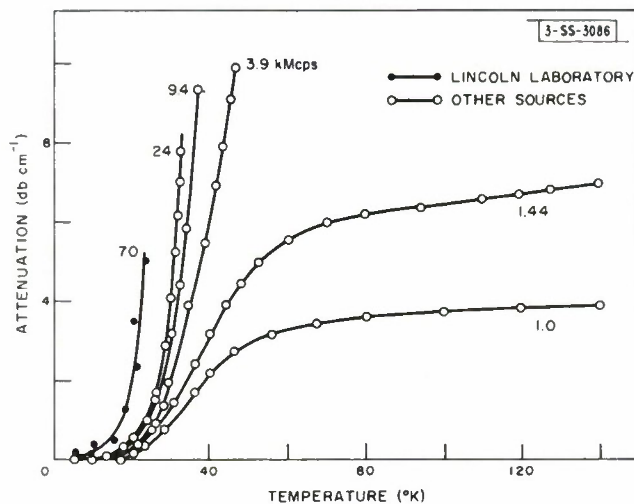

Fig. V-4. Temperature dependence of attenuation of longitudinal phonon echoes in x-cut quartz at 70 kMcps obtained from measurement of first echo only. The other curves, shown for comparison, are taken from the literature (Ref. 10). All curves normalized to 0-db-cm^{-1} attenuation at 4.2°K.

b. Upper Critical Fields of Niobium

Measurements of the upper critical field of pure and impure niobium have been extended down to 0.4°K by adapting the equipment for use in the He^3 refrigerator which has been described in earlier Solid State Research reports. The results are not entirely conclusive because of the uncertainty in thermometer calibration.

E. S. Rosenblum
S. H. Autler
W. C. Kernan
K. H. Gooen (National Magnet Laboratory, M.I.T.)

3. Phonon Attenuation in Quartz at 70 kMcps

The temperature dependence of the attenuation of 70-kMcps longitudinal phonons in x-cut quartz has been measured from 4.2° to 25°K. Preliminary results are shown in Fig. V-4, along with data at other frequencies taken from the literature.[10] The qualitative behavior of the attenuation is as expected: the steep rise occurs at a slightly lower temperature than at lower frequencies. A signal-to-noise ratio for the first echo of 20 db (Fig. V-5) has been obtained by altering the cavity geometry and selecting the best of the present quartz samples. The large decrement between successive echoes is attributed primarily to surface roughness and interference of components of the acoustic waves. The absolute attenuation of the phonons in the quartz is small because, in some samples, the size of successive echoes decreases only slightly; however, in these cases the first echo is always very small. Efforts to increase the number of observed echoes are now directed toward obtaining better quartz samples and investigating the feasibility of a pulse-integrating detector.

A scale drawing of the microwave cavity and sample initially used to observe the phonon echoes is shown in Fig. V-6.

J. B. Thaxter
P. E. Tannenwald

C. THEORY

1. Elastic Magnetic Scattering of Neutrons

In their neutron-diffraction study of manganese chromite, Hastings and Corliss noted not only that the sharp magnetic "satellite" peaks near the (111) nuclear position degenerated into a broad, liquid peak at about 20°K, well below the Curie point of 41°K, but also that this liquid peak persisted up to at least 300°K.[11] Prince has observed similar persistence of a liquid short-range-order peak near the (111) position in nickel chromite.[12] However, we did not notice any distinct liquid peak in cobalt chromite at room temperature, even though its Curie point is 96°K.[13]

In order to gain some understanding of the above behavior, we began a theoretical investigation of the elastic magnetic scattering to be expected at high temperature. This diffuse scattering is given for a powder by

$$I_d(2\Theta) = \frac{2}{3} BF_d(\kappa)$$

where B is a constant of the experiment and

$$F_d(\kappa) = \Sigma_\nu \Sigma_{m\mu} g_\nu f_\nu(\kappa)\, g_\mu f_\mu(\kappa)\, \overline{\underset{\sim}{S}_{1\nu} \cdot \underset{\sim}{S}_{m\mu}}\, j_o(\kappa \tau_{1\nu}^{m\mu})$$

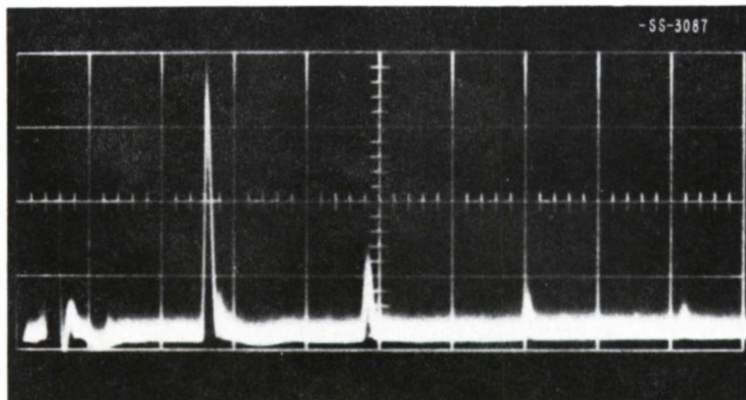

Fig. V-5. Longitudinal phonon echoes excited in 1/4-inch-long x-cut quartz rod placed in microwave cavity. Horizontal scale is 1 μsec div^{-1}.

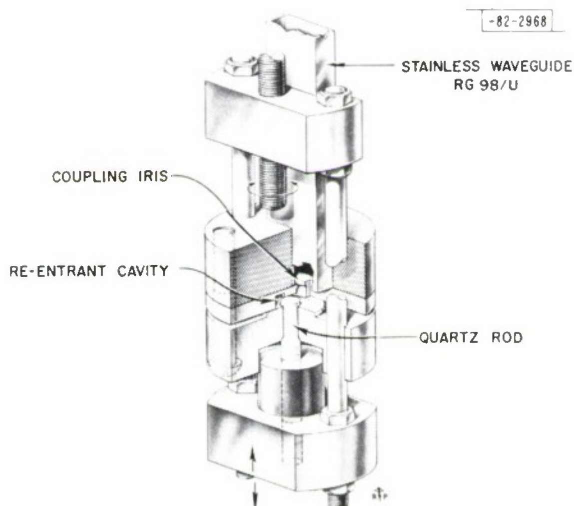

Fig. V-6. Microwave re-entrant cavity and quartz rod initially used for observation of echoes. Over-all height is 1 inch.

Here, κ is the magnitude of the neutron scattering vector, ν and μ run over all the sublattices (six for the spinel) and m runs over all the unit cells in a crystallite, g_ν and $f_\nu(\kappa)$ are, respectively, the g-factor and the form factor appropriate to the νth site, $\tau_{1\nu}^{m\mu}$ is the distance between the two indicated sites, and j_o is the spherical Bessel function. The $\underset{\sim}{S}_{n\nu}$ are the spin operators, and the bar represents the quantum-mechanical average value at the temperature in question.

When $(m\mu) = (1\nu)$, the contribution is simply

$$F_d^{(o)}(\kappa) = \Sigma_\nu g_\nu^2 f_\nu^2(\kappa)\, S_\nu(S_\nu + 1)$$

where S_ν is the spin quantum number for the νth ionic specie. The remaining terms, $(m\mu) \neq (1\nu)$, can be expanded as power series in $\beta = 1/kT$, where the coefficient of β^{p+q} involves such quantities as $\langle S_{1\nu} \cdot S_{m\mu} H^p \rangle \langle H^q \rangle$. Here, H is the Heisenberg Hamiltonian and $\langle\ \rangle$ denotes the average value at infinite temperature. We have evaluated the first three terms in this expansion for manganese chromite.

We find that, at room temperature, the expansion for $\overline{\underset{\sim}{S}_{1\nu} \cdot \underset{\sim}{S}_{m\mu}}$ appears to converge very rapidly, so that only the first-order term in β contributes appreciably to the neutron diffraction. This term produces a broad peak in the vicinity of the (111) nuclear position. When this contribution is added to the effect of $F_d^{(o)}(\kappa)$, excellent quantitative agreement is obtained with the experimental diffraction pattern.[14] Furthermore, our calculations show that the liquid peak would still be observable at 600°K. It is essentially the same as the familiar high-temperature "antiferromagnetic peak" observed in antiferromagnets, and arises directly from the antiferromagnetic nature of the exchange interaction. Consequently, it should be present in all ferrimagnetic spinels.

When the first three terms are re-evaluated for cobalt chromite at room temperature, the broad peak is indeed found to be present. However, its predicted magnitude is so much smaller than for manganese chromite that it would not have appeared as a peak under our particular experimental conditions. Thus, our cobalt chromite results do not contradict the theoretical prediction.

We have also tried to compute the diffuse diffraction pattern to be expected for manganese chromite at 77°K. Here, we find that the expansion is converging very slowly, so that not even semiquantitative comparison with experiment can be obtained from just the first three terms. However, the general qualitative behavior is suggestive, so that an extension of the calculation to higher-order terms would appear worthwhile, particularly since the diffuse peaks are much sharper than at higher temperatures and consequently contain more information.

K. Dwight
N. Menyuk
T. A. Kaplan

2. Aspherical Spin-Density in S-State Cations

We consider a cation that has a $^6S(d^5)$ ground term in an octahedral crystal field and take an unperturbed state in which the spin component S_z, for some direction z, has its maximum value. In this state, the magnitude of the spin density $\vec{s}_o$ is spherically symmetric. Restricting

ourselves to the configuration d^5, it is found that in first order, spin-orbit coupling gives an additional contribution $\vec{s}_1(\vec{r})$ to the spin density. The quantity $\vec{s}_1(\vec{r})$ is perpendicular to $\vec{s}_o$, integrates to zero, and is highly aspherical, since it is a linear combination of the spherical harmonics Y_{4m}. In the high-temperature phase of α-Fe_2O_3, $\vec{s}_1(\vec{r})$ contributes to the neutron diffraction intensity at the same peaks as does the weak ferromagnetic moment (the Dzialoshinsky canting of $\vec{s}_o$). This contribution is estimated to be of the same order as that of the Dzialoshinsky moment at several of the peaks. Hence it is probably important to an understanding of the surprising, highly aspherical distribution recently observed by Pickart, Nathans, and Halperin. Furthermore, $\vec{s}_1(\vec{r}) \neq 0$ should occur under much more general conditions than needed for the Dzialoshinsky canting; for example, at low temperatures in α-Fe_2O_3 the latter does not occur, whereas $\vec{s}_1(\vec{r})$ is roughly of the same size as that calculated for the high-temperature ordering. Higher-order perturbation effects are being investigated.

T. A. Kaplan

3. Proposed Spin Configuration for MnP

In the last Solid State Research report (1963:3), it was pointed out that the susceptibilities along the three principal axes of single-crystal MnP cannot be interpreted on the basis of a flat, cycloidal spiral propagating along the orthorhombic c-axis and distorted by anisotropy forces alone within the b-c plane. Since the exchange parameter J'_{AA} for interactions between next-near neighbors in the a-c plane, which are along the c-axis, was assumed temperature dependent via thermal expansion of the c-axis, it is necessary to include the dependence of J'_{AA} on the c-axis parameter in the entire calculation. Therefore, it is necessary to multiply J'_{AA} by the factor $(1 - \alpha_s \epsilon_n)$ in the expression for the exchange energy E_{ex} entering the Hamiltonian. Here

$$\epsilon_n = [(\underset{\sim}{R}_{n+2} - \underset{\sim}{R}_n) - (\underset{\sim}{R}_{o,n+2} - \underset{\sim}{R}_{o,n})]\, 2/\eta$$

is the strain induced by exchange striction and α_s is a nondimensional parameter. Minimization of the total energy with respect to ϵ_n gives

$$\epsilon_n = \epsilon_o \cos(\varphi_{n+2} - \varphi_n), \qquad \text{where} \qquad \epsilon_o = \alpha_s J'_{AA} M_s^2/2Y$$

where Y is Young's modulus and φ_n is the angle the moment of the nth (001) plane makes with the direction of an applied field H. If H = K = 0, the magnetic spiral remains simple and the exchange striction is uniform. In this case,

$$\varphi_n(H = K = 0) = \varphi_n^o = n\Theta$$

and minimization of E_{ex} with respect to Θ yields

$$\cos\Theta\,[1 - 2\alpha_s \epsilon_o \cos 2\Theta] = (J_{AB} - 4J_{AA})/4J'_{AA}$$

Thus, if $\Theta_o > \pi/4$, exchange striction increases the turn angle ($\Theta > \Theta_o$ where $\Theta = \Theta_o$ for $\epsilon_o = 0$), and if $\Theta < \pi/4$, it decreases the turn angle ($\Theta < \Theta_o$).

If $H \neq 0$ and $K \neq 0$,

$$\varphi_n = n\Theta - \epsilon h_A \sin(2n\Theta) - h \sin(n\Theta)$$

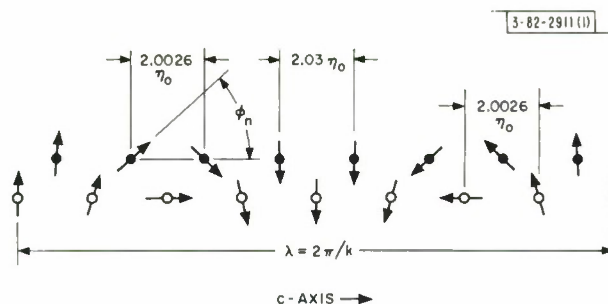

Fig. V-7. Proposed spin configuration [distorted spiral (11)] for the antiferromagnetic phase of MnP, given that $\theta = \pi/8$, and $\epsilon_o = 0.15$. The turn angle is $\phi_n = n\theta - h_A \sin(2n\theta)$, where $h_A = -2(\chi_c - \chi_b)/(\chi_c + \chi_b) = -0.5$. This gives $\phi_n = 0$, $\pm 42.5°$, $\pm 73.6°$, $\pm 106.4°$, $\pm 137.5°$, and $\pm 180°$. Both θ and ϵ_o are temperature dependent.

where

$$h_A \equiv (2K/M_s^2)/\{64J'_{AA}\Theta^4 [1 - \tfrac{1}{2}(\alpha_s\epsilon_o/\Theta^2) - \tfrac{4}{3}\alpha_s\epsilon_o]\}$$

$$h \equiv (H/M_s)/\{5J'_{AA}\Theta^4 [1 - \tfrac{4}{5}(\alpha_s\epsilon_o/\Theta^2) - \tfrac{26}{15}\alpha_s\epsilon_o]\} \quad .$$

Thus small distortions of the spiral due to the presence of anisotropy in the b-c plane are amplified by the magnetostrictive effects. The observed susceptibilities can be accounted for by $\Theta = \pi/a = 20°$, provided $\alpha_s \sim 15$ and $\epsilon_o \sim 0.015$ if $\alpha_s\epsilon_o \sim \alpha_s^2 10^{-2}$. These numbers are reasonable and lead to the distorted spiral of Fig. V-7. Thus this analysis suggests that there should be a measurable modulation of the c-axis spacing that has half the wavelength of the spiral. From a combination of x-ray and neutron-diffraction experiments as a function of temperature in the antiferromagnetic region, it should be possible to obtain independent numbers for all the parameters of the theory.

J. B. Goodenough

4. Higher-Order Corrections to the Molecular Field Theory of the Magnetic State

A hierarchy of approximations is set forth in which the expectation value of the spin at the ith site in the nth approximation is given by

$$\langle S_i^z \rangle = \sum_{j=0,n} \langle S_i^z \rangle_j \, \epsilon^j \quad .$$

The coefficients $\langle S_i^z \rangle_j$ are computed by equating terms in ϵ^j in the expression

$$\Sigma \langle S_i^z \rangle_j \, \epsilon^j = \mathrm{tr}\,\{\exp[-\beta(\mathcal{H}_o + \epsilon\mathcal{H}')]\, S_i^z\}/\mathrm{tr}\,\exp(-\beta\mathcal{H})$$

in which $\epsilon\mathcal{H}' = +2\Sigma J_{ij} \langle S_i^z \rangle S_j^z + \mathcal{H}$, $\mathcal{H} = \mathcal{H}_o + \epsilon\mathcal{H}'$, and $\mathcal{H}$ is the Heisenberg Hamiltonian. The zeroth and first approximations correspond to the Weiss molecular field result. The nth approximation gives the susceptibility

$$\chi^{(n)} = \frac{Ng^2\mu^2 S(S+1)}{3kT} \frac{\sum_{i=0,n} a_i (J/kT)^i}{1 - a_1 a_n (J/kT)^{n+1}}$$

in which the a_i are the usual coefficients of the high-temperature susceptibility expansion.[15] The nth approximation to the Curie temperature is given by $(kT_c/J)^{n+1} = (a_1 a_n)$. The temperature dependence of the magnetization near T_c is also obtained.

G. Dresselhaus

REFERENCES

1. W. Kunnmann, D. B. Rogers, and A. Wold, "Use of CO/CO_2 Atmospheres for the Synthesis and Free Energy Determination of Several Mixed Oxide Systems," J. Phys. Chem. Solids (to be published).
2. J.K. Galt, B.T. Matthias, and J.P. Remeika, Phys. Rev. 79, 391 (1950).
3. J.P. Remeika, J. Am. Chem. Soc. 78, 4259 (1956); J. W. Nielson, J. Appl. Phys. 29, 390 (1958).
4. R. Summergrad and E. Banks, J. Phys. Chem. Solids 2, 312 (1957); A. Mones and E. Banks, J. Phys. Chem. Solids 4, 217 (1958); R.J. Gambino and F.S. Leonhard, J. Am. Ceram. Soc. 44, 221 (1961).
5. W. Kunnmann, A. Wold, and E. Banks, J. Appl. Phys. 33, 1364 (1962).
6. A. Ferretti, R.J. Arnott, E.J. Delaney, and A. Wold, J. Appl. Phys. 32, 905 (1961).
7. A. Wold, W. Kunnmann, R.J. Arnott, and A. Ferretti, "Preparation and Properties of Molybdenum Bronzes," Inorganic Chemistry (to be published).
8. J.B. Goodenough, J. Appl. Phys. Suppl. (to be published, 1964).
9. C.P. Bean and D.S. Rodbell, Phys. Rev. 126, 104 (1962).
10. E.H. Jacobsen, Quantum Electronics (Columbia University Press, New York, 1960), p. 468.
11. J.M. Hastings and L.M. Corliss, Phys. Rev. 126, 556 (1962).
12. E. Prince, J. Appl. Phys. 32S, 68 (1961).
13. N. Menyuk, K. Dwight, and A. Wold, J. Phys. Radium (to be published).
14. We are indebted to L.M. Corliss and J.M. Hastings for sending us their complete data.
15. G.S. Rushbrooke and P.J. Wood, Molecular Phys. 1, 257 (1958).